UNIVERSITÀ DEGLI STUDI DI CATANIA
Dottorato di Ricerca in Fisica - XXIII ciclo

ROSALBA MIRACOLI

CHARACTERIZATION OF MICROWAVE DISCHARGE ION SOURCE FOR HIGH PROTON BEAM PRODUCTION IN CW AND PULSED MODE

PhD Thesis

Tutors:
Prof. Salvatore Cavallaro
Prof. Santo Gammino
Supervisors:
Dr. David Mascali
Dr. Luigi Celona

PhD coordinator:
Prof. Francesco Riggi

XXIII CICLO 2007-2010

This study has been made in collaboration with

Laboratori Nazionali del Sud
Istituto Nazionale di Fisica Nucleare
64, Via S.Sofia I-95123
Catania, Italy

Contents

Introduction

The production of high current beams is a key point for different applications and this role is deemed to increase in the coming years, either for industrial applications and for the research projects. High current and high brightness H^+ beams can be provided by 2.45 GHz MDIS - Microwave Discharge Ion Sources, which present many advantages in terms of compactness, high reliability, ability to operate in CW mode or in pulsed mode, reproducibility, and low maintenance.

MDIS operations are based on the generation of a slightly overdense plasma ($n_e \simeq 10^{17}\ cm^{-3}$) produced by the interaction of microwaves with H_2 gas introduced at low pressures ($10^{-5}\ mbar$) inside a copper made chamber with a volume of one liter approximately, in presence of a 0.1 T magnetic field that is slightly higher than the Electron Cyclotron Resonance value (for this reason the MDIS are also called off-resonance discharges). In this way, electrons having temperatures of the order of 20 eV can be generated, which are able to disgregate the H_2 molecules and to further ionize the atomic hydrogen, thus finally obtaining protons. Typical extracted proton currents are of the order of $30 - 100$ mA, with extraction energies of the order of $50 - 80$ keVs. The extraction system is typically composed by two or more electrodes, and a high voltage platform is usually employed to insulate the plasma chamber with respect to the beam line and the other equipments (microwaves generators, waveguides, etc.). The magnetic field can be either produced by room temperature solenoids or by permanent magnets (this improves the compactness of the source). No magnetic traps are needed, since the collisions needed to obtain protons from the molecular hydrogen are only few and require short times.

Important industrial applications for which sources are purchased fell into three categories [1].

In the first category is the surface cleaning by means of inert or reactive ion beams. The process is known as **etching**. The second category concerns the deposition of coatings, by using the flux sputtered off from a target by the ion beam. This is known as **ion beam sputter deposition**. The Third category involves the concurrent use an ion beam to improve the properties of a coating that is being deposited using different technique (direction deposition). This is **ion-assisted deposition**.

The ion sources can be employed to characterize the structure of the atoms or the molecular structure of the materials. It is possible, for example, to use as probes X-rays and neutrons. Neutron beams can be produced through fission in the nuclear reactors, or by spallation processes induced by accelerated proton beams. Moreover, a CW proton beam of a few tens of MW produce a neutron flux that is able to sustain subcritical nuclear reactors. The same principle can be used for the incineration of nuclear wastes (actinides and long lived fission fragments) produced by conventional over-critical reactors, leaving no substantial amounts of radiotoxic waste at the end of the cycle. In 1998 the Research Ministers of France, Italy and Spain, recognizing the potentialities of Accelerator Driven System (ADS) for the transmutation of long-lived nuclear wastes [2], decided to define a common R&D European platform on ADS, promoted by Carlo Rubbia through the idea of the Energy Amplifier (in Italy the project was named TRASCO - TRAsmutazione SCOrie).

Several forthcoming projects are foreseen for the next future, all of them covering the large parte of the above mentioned applications. The INFN-LNS group focused on the *R&D* for ion sources, for example, has been involved in the TRASCO project since 2000: the TRIPS (TRASCO Intense Proton Source), that is now in operation at INFN-LNL, was here designed constructed and tested, fulfilling all the requirements of the TRASCO ADS [3]. Other crucial projects in the framework of european collaborations are, in particular: the ESS - European Spallation Source [4], to be built in Lund, Sweden, and the MYRRHA project to be installed Mol (Belgium) [5]. A third project (DEDALUS) will make use of MDIS for a new high power cyclotron to be installed in China [6].

For each source the most important parameters are the maximum beam current and the intensity of the single ion species. So the total beam current and the proton beam was studied as a function of different experimental set-up. In order to make a meaningful analysis, further measurements are required, regarding the quality of the ion beam. The quality of the ion beam extracted from an ion source is characterized by the beam emittance; for high quality ion beams the emittance should be as small as possible. The beam formation is therefore an essential process for the optimum operation of the following accelerator as it *shapes* the beam either in the transversal phase space and in time. A stringent request in terms of (*rms* normalized) beam emittance at the entrance of the radio frequency quadrupole (RFQ) may be of the order of 0.20 to 0.30 π mm mrad, which makes essential to design and test the ion source and low energy beam transport (LEBT) as a whole.

In order to understand the plasma processes in the Microwave Discharge Ion Source (MDIS) and improve the performance of the ion sources, a number of experiments have been carried out. A theoretical discussion dealing with plasma physics relevant for the production of intense proton beam in MDIS are considered in chapter 1. An historical overview on the production of high current beams by the 2.45 GHz microwave ion sources is introduced in chapter 2. The ion sources and the diagnostics used in the experiments are discussed in chapter 3. In chapter 4 the measurements on the VIS source at LNS and on the SILHI source at CEA-Saclay are presented. Different methods to improve the electron density are discusses in chapter 5. Finally, in chapter 6, the conclusion are drawn.

We were able to characterize the sources either by the point of view of the extracted current and of the emittance, in CW and pulsed mode. The obtained values fall within the requirements of the aforementioned projects. New solutions to further improve the performances have been indicated throughout the thesis. A particular attention was paid, in fact, to some innovative tools able to increase the electron density for a more efficient ionization, this getting more intense currents. The main limitation of MDIS, in fact, consists of the so called electromagnetic cutoff, which naturally fixes the upper boundary of the plasma density which can be reached at a given frequency. Passive and active techniques can be used on the purpose to overcome this limit. A series of measurements were carried out with VIS source by inserting a thick Al_2O_3 tube inside the plasma chamber (passive technique), which provided a increment of the current of 20%. A preliminary test has been carried out with CAESAR (that is a source for multicharged ions) making use of Carbon nanotubes as electron guns (active technique) [7]. Improvements on the extracted beams were of the order of $30 - 70\%$. Finally, another active mechanism was tested on a device very similar to the VIS source: we tried to employ an innovative mechanisms of plasma ignition based on electrostatic waves (ESW) [8]; the possible conversion of electromagnetic waves into electrostatic modes into the plasma were carefully investigated, as the electrostatic wave do not suffer any density cutoff in their propagation throughout the plasma.

Chapter 1

Plasma Physics applied to ECR ion source

Ion sources have been used for a wide variety of application. They are used for different types of accelerator for nuclear research; they have application in the field of fusion research; and they are used for different industrial processes like ion milling and implantation, etc.

It is important to underline the relationship between ion source performances and plasma parameters. The ion beam current is first of all determined by the plasma density, the magnetic field configuration, the electron plasma temperature, and the plasma size. The improvement of these parameters improve the beam brightness and more generally, high-performance ion beams are extracted from high-performance plasmas.

1.1 Collisions in plasma

Plasma collisionality plays a crucial role in several processes. It regulates the confinement times in magnetically confined plasmas, it thermalizes the electrons in low temperature discharges and it determines the ionization rates in a plasma used as source of ions.

Collisions between the charged particles in plasma are quite different from collision between the neutral particles in an ordinary gas. Energy and momentum are exchanged by means of a large number of distant interactions by single or multiple interactions.

The collision probability is usually expressed by means of the concept of cross-section. But in the plasma the most useful concepts related to the cross-section are the mean free path and the collision frequency. If the collision cross-section is σ, the *mean free path*, before the particle suffers a collision, can be obtained as:

$$\lambda_{mfp} = \frac{1}{n\sigma} \tag{1.1.1}$$

where n is the appropriate particle density. The collision time τ is related to the λ_{mfp} and σ by:

$$\tau = \frac{\lambda}{v} = \frac{1}{n\sigma v} \tag{1.1.2}$$

where v is the appropriate mean particle velocity. The collision frequency ν is the reciprocal of the collision time,

$$\nu = \frac{1}{\tau} = n\sigma v \tag{1.1.3}$$

Frequency and times of collisions change with electron density n_e and electron temperature T_e and if the collisons concern like or unlike particle. For ion source plasmas τ usually lies in the range from nanoseconds to milliseconds.

This collision frequency ν is the most convenient parameter to take in ions sources, because its value can be compared to the typical plasma frequencies such as the cyclotron frequency ω_c (see section 1.3), the Spitzer frequencies (see section 1.1.1) ν_{ei}, μ_{ee} and ν_{ii} the plasma frequency ω_p, the bounce frequency ω_b in a mirror system and all kinds of wave frequency ω introduced or self-generated in the medium.

In the next sections the collisions will be divided into two different groups: **multiple collisions** and **binary collision**.

1.1.1 Spitzer collisions

The **Spitzer collisions** represent the multiple interactions of a single particle with many other particles, and the net effect is to give a large-angle scattering. These cumulative small-angle scatterings resulting finally in a 90° deflection are then supposed to be the most probable scattering mechanism inside the plasma.

In principle, these collisions can extend over the whole distance over which the Coulomb forces are effective; however in order to make probable the calculation of the cross-section, it is necessary to choose a distance, given by the **Debye** shielding length Λ_D[1], for distance greater than Λ_D a Coulomb force can be neglected (as a consequence of the charged particles screening). Beyond this distance, the plasma may be regarded as being electrically neutral, so that the particle under consideration is not affected by Coulomb forces.

An effective cross-section for 90° deflection by means of multiple collisions can be defined as [9]:

$$\sigma = 8\pi \left(\frac{z_1 z_2 e^2}{M v^2} \right) \ln \left(\frac{\Lambda_D}{b_{min}} \right) \qquad \text{[CGS]}$$

where z_1 and z_2 are the charges of the two particles, e is the electron charge, M is the mass of the colliding particle (if one considers the other particles much more massive) and the term $\frac{\Lambda_D}{b_{min}} = \ln \Lambda$ is the so called Coulomb logarithm.

This equation is similar to the cross-section for single Coulomb scattering (Rutherford formula), but the multiple scattering probability exceeds single scattering by the factor $(8 \ln \Lambda)$, the 90° scattering due to a single collisions is much less probable than multiple deflections.

A more precise representation of the multiple collisions can be given in the center of mass system, and the collision frequencies can be calculated by taking into account collisions among the two different plasma species: electrons and ions. Omitting, for sake of brevity, the mathematical description, we can use the final formulas to understand what is the role that each type

---

[1] Debye Length: $\Lambda_D = \frac{\epsilon_0 k T_e}{n e^2}^{1/2}$; a particle feels the electromagnetic interaction due only to those particles located inside the Debye sphere. The Debye length helps to correct define a plasma: being L the plasma typical dimension, must be $\lambda_D \ll L$. This last condition is also called *plasma quasi-neutrality*

of collision plays in the plasma [9]:

$$\begin{aligned}
\nu^{ee}_{90^\circ} &= \frac{1}{\tau_{sp}} = 5\cdot 10^{-6} n_e \frac{\ln\left(\frac{\Lambda_D}{b}\right)}{T_e^{\frac{3}{2}}} \\
\nu^{ei}_{90^\circ} &= \frac{1}{\tau_{sp}} \sim 5\cdot 10^{-6} z n_e \frac{\ln\left(\frac{\Lambda_D}{b}\right)}{T_e^{\frac{3}{2}}} \\
\nu^{ii}_{90^\circ} &= \frac{1}{\tau_{sp}} \sim z^4 \left(\frac{m_e}{m_i}\right)^{\frac{1}{2}} \left(\frac{T_e}{T_i}\right)^{\frac{3}{2}} \nu^{ee}_{90^\circ}
\end{aligned} \tag{1.1.4}$$

n_e is in cm^{-3} and T_e in eV.

Each frequency is usually called characteristic Spitzer collision frequency. Once given the collision frequency we can easily determine the time between two successive events: $\nu^{ee}_{90^\circ} \sim \nu^{ei}_{90^\circ}$, and $\tau^{ee}_{90^\circ} \sim \tau^{ei}_{90^\circ}$; on the contrary, if we consider ions colliding against electrons (i-e collisions), we have:

$$\tau^{ie}_{90^\circ} \approx \left(\frac{m_i}{m_e}\right) \tau^{ei}_{90^\circ} \tag{1.1.5}$$

The amount of the energy transferred for particles of the same species (for example e-e or i-i) is about the half of the initial one, whereas it is equal to the $\frac{m_e}{m_i}$ fraction in case of e-i or i-e collisions.

The electrons in plasmas exchange energy and they can reach an equilibrium distribution on a rather short time-scale. Moreover ν_{ee} and ν_{ei}, Spitzer collision frequency, are much smaller than ω_{ce} and ω_{RF} (which are generally between 2.5 and 20 GHz). Hence the Spitzer collisions do not impede the electron gyromotion.

Therefore ECR plasma are termed collisionless plasma, and this remains true in most cases even when inelastic and elastic collisions are added to the Spitzer collisions.

The electron transfer energy to ions, or vice versa, on a time scale that is m_i/m_e times longer than the time required for electron thermalization. For example, in a MDIS plasma with density of 10^{11}cm^{-3} at $T_e = 10eV$, ν_{ee} lies between 10^5 and 10^6 s$^-1$. Thus electron thermal equilibrium is reached on a very short scale, a few microseconds (which is general shorter than the electron lifetime) whereas ions cannot be heated at all by electron-ion collisions, and they will remain cold.

The difference in thermalization times is more evident for more energetic electrons: when $T_e \sim 1keV$ one finds ν_{ee} between 10^2 and $10^3\,s^{-1}$. Only if the electron lifetime is comparable with these values it would be possible to obtain an electron thermalization through *ee* (electron-electron) collisions. For the ions, their lifetime is too short to be heated by the electrons. We now understand why in the most MDIS plasmas hot electrons are mixed with cold ions. Thanks to this cold-ion property the MDIS may provide ions beams with small emittances (see section 1.5).

1.1.2 Elastic electron-neutral collision

An elastic collision is defined as the one which does not alter the internal energy state of the colliding particles. The most important consequence of an elastic collisions is the possible deflection of the electron. This effect is described in term of a *differential* cross-section $I_0(\theta) = I_0 \sin\theta\, d\theta d\phi$ for elastic scattering into the solide angle $d\Omega$. $I_0(\theta)$ is proportional to the probability of an electron being scattered by an elastic collision into the given element of solid angle $d\Omega$.

The figure 1.1.1 gives the total electron-neutral collision frequency versus the electron energy for different gases. The general behavior demonstrated in this figure is that the total electron frequency increases with electron energy (< 10 eV)and then more or less saturate at electron energies above about 10 eV.

1.1.3 Binary inelastic electron collision

Binary collisions play a main role in the plasma ionization. If the electron energy is not enough (it must overcome the ionizing potential), the effect of the collision becomes the excitation of the atom. Hence there are two main inelastic collision process:

1. total ionization from the ground state;

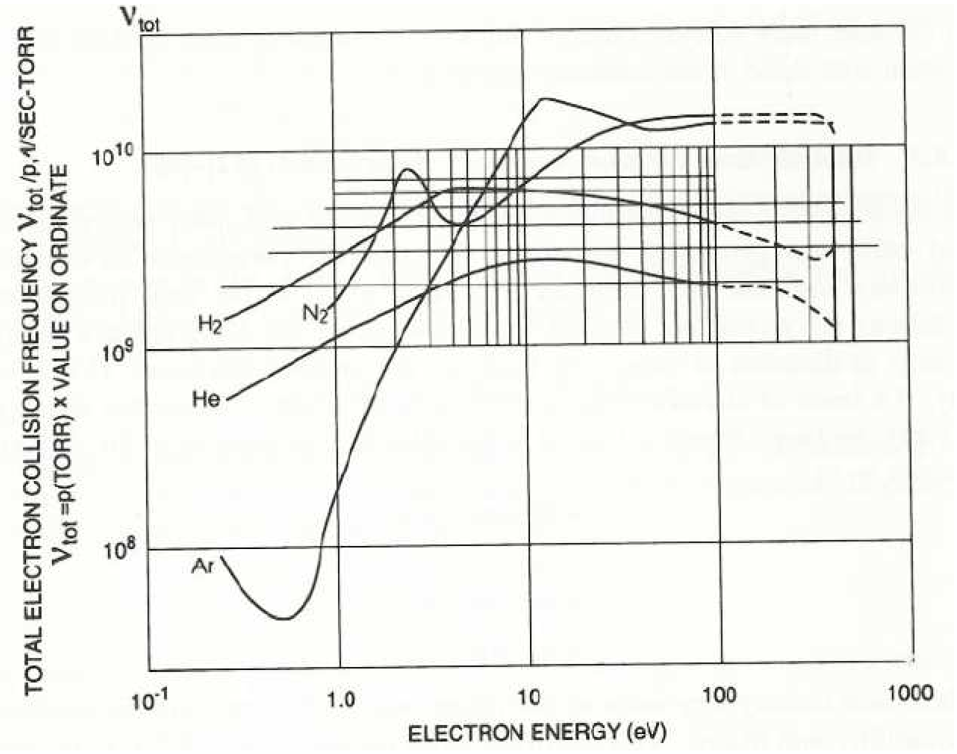

Figure 1.1.1: *The total electron-neutral collision frequency versus the electron energy for* H_2, *He* N_2 *and Ar [9].*

2. total excitation from the ground state.

The electron-neutral elastic and inelastic collisions play an important role in case of high pressure plasmas with a low degree of ionization and low electron temperature ($T_e \leq 15\,eV$).

At electron temperatures comparable or higher than the neutral ionizing potential, the ionizing collisions becomes the most important collision. The basic reaction equation is:

$$\mathrm{e}^- + A \rightarrow e^- + A^+ + e^- \tag{1.1.6}$$

As it can be seen from figure 1.1.2, the effective ionizing frequency increases rapidly once that the threshold energy has been passed. The maximum values of σ_i are the order of $10^{-16}\,cm^2$ and they correspond to electron

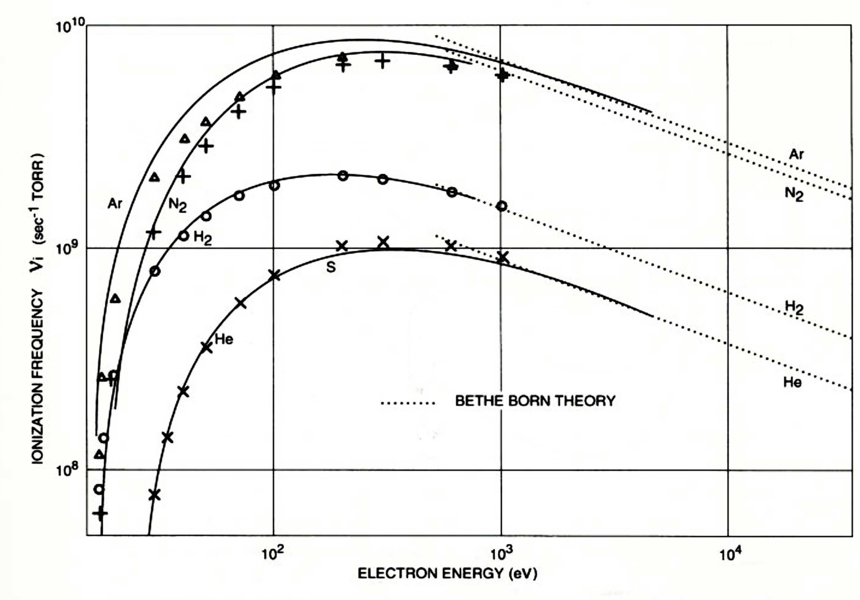

Figure 1.1.2: *Ionization frequencies versus the electron energy. For high electron energies the experimental data have been fitted with the Bethe-Born theoretical formula [9].*

energies of order of 100 eV. After the collision, one slow electron and one fast electron, which carries off the major part of the kinetic energy not used in the reaction, are generally present. The slow electron has an approximately uniform angular distribution, while the fast electron tends to maintain the direction of the initial electron.

1.1.4 Remarks about collisions

In these section we have introduced the most important interaction between the plasma particles. In the sources that I will be described in the chapter 3, the electron temperature change between 10 and 20 eV. The electron-neutral momentum transfer collision at low electron energies plays a similar role in the weakly ionized plasma as the 90° electron-ion Spitzer collisions in the strong ionized plasma. In low-electron-temperature plasma, working at relatively high pressure ($> 10^{-3}$ mbar) with the e-N collisions are responsabile for randomization processes. In figure 1.1.3, the e-i Spitzer collisions are compared at e-N momentum transfer collisions, at different hydrogen pressure for a relatively cold electron plasma, with density $10^{18} \leq n \leq 10^{14}$ cm^{-3}. We see that above $T_e \sim 1$ eV the Spitzer frequencies can became smaller than 10^{-5} mbar, emphasizing the important role played by e-N collisions in weakly ionized plasma. At higher energies inelastic frequencies became comparable to the total collision frequency, because the elastic collisions decrease.

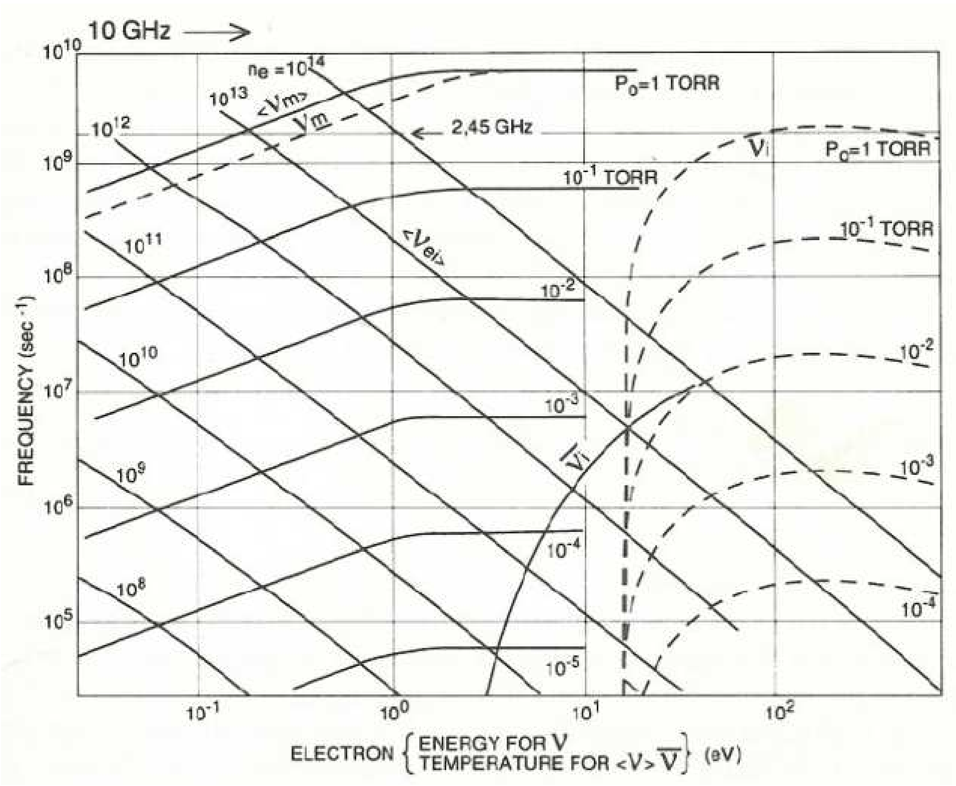

Figure 1.1.3: *Electron-ion momentum transfer* ν_{ei} *versus electron energy or temperature for singly charged ions with electron density as parameters.* ν_M, *electron-neutral momentum transfer, and* ν_{ion}, *ionization frequency, are given for comparison (gas* H_2*) [9].*

1.2 Plasma confinement

High temperature plasmas cannot be contained by a natural vessel, but only by magnetic fields. In order to confine the particles in a bounded volume, the magnetic fields must be curved and inhomogeneous. The Lorentz forces that act on the charged plasma particles and forced them into circular and helical orbit around the magnetic fields lines.

The source, object of this thesis, produces low-charged ion beams, so it does not need a magnetic trap which confines the electrons for times higher than 10^{-5} s. The presence of an external magnetic field is not aimed to the production of high-energy electrons and multi charged ions, but it has the function of making an anisotropic plasma where the electromagnetic wave can transfer their energy to electrons (see the next sections 1.3).

1.3 Waves in plasmas

The wave propagation in plasmas is a quite complex subject, as it involves many aspects of the plasma physics and the mathematical approach is not so easy. Waves can be studied by different points of view, especially using the kinetic or the fluidodynamical models. The most simple approach is the single particle one, which however gives information about the principal modes propagating in the plasma. Here we limit our analysis to the general issues, with the aim to determine the cutoffs and resonances of each mode propagating in a magnetized plasma. Plasma waves are always associated with a time and space varying electric field, and the propagation properties of such fields are determined by the dielectric properties of the medium, which in turn depend on eventually applied magneto-static or electrostatic fields. A plasma may be both inhomogeneous and anisotropic, and this affects its dielectric properties.

The anisotropy can be easily induced by a magneto-static field. MDIS plasma are then anisotropic media by the point of view of electromagnetic wave propagation.

Other than pure electromagnetic waves (EM), in plasma exist partially or totally longitudinal waves, the latter named *electrostatic* wave (ES). EM and ES waves can couple each other, and EM waves can converted in ES wave and vice versa. More details about ES waves will be given in the section 1.3.1. Propagation of wave in plasmas is strongly influenced by spontaneous, self generated plasma oscillations. They arise when any displacement of electrons occurs with respect to the positive, rigide *sea* of background massive ions. In order to preserve the quasi-neutrality, a restoring force arises which causes the oscillation of electrons at a frequency which depends only on the electron density, and due by plasma frequency. This mechanism generates oscillations which in a cold plasma approximation, i.e. $T_e = T_i \sim 0$, do not propagate into the plasma.

They can be found mathematically by perturbing the fluid equations $\dfrac{\partial \rho_m}{\partial t} + \vec{\nabla} \cdot \rho_m \vec{V} = 0$ (mass continuity equation) and $\vec{\nabla} \times \vec{B} = \dfrac{4\pi \vec{J}}{c}$ (Maxwell equation) with time varying harmonic electric and magnetic fields:

$$\vec{E}_1 = \hat{E}_1 e^{i\omega t} \tag{1.3.1}$$

$$\vec{B}_1 = \hat{B}_1 e^{i\omega t} \tag{1.3.2}$$

Assuming that the perturbing fields have small amplitudes, the fluid equations can be linearized and the Maxwell equation for B$_1$ gives:

$$\vec{\nabla} \times \hat{B}_1 = -\frac{\imath\omega}{c} \left[1 - \frac{\omega_p^2 \left(1 + m_e Z/m_i\right)}{\omega_2} \right] \hat{E}_1 \tag{1.3.3}$$

considering that $m_e \ll m_i$, we can write for the dielectric constant:

$$\epsilon\left(\omega\right) \sim 1 - \frac{\omega_p^2}{\omega^2} \tag{1.3.4}$$

$\omega_p^2 = \dfrac{n_e e^2}{\epsilon_0 m_e}$ in MKS units, is the so-called plasma frequency, and it can be demonstrated that oscillations exist inside the plasma at this frequency. Note that a corresponding frequency can be determined also for ions.

By looking again to the expression 1.3.4, some further considerations can be done. In particular it may be noted that electromagnetic waves with frequencies lower than ω_p cannot propagate into the plasma. In other words *in homogeneous and non magnetized plasmas the density cannot exceed the so called cutoff value given by*:

$$n_{cutoff} = 4\pi^2 \frac{m\epsilon_0}{e^2} f_p^2 \tag{1.3.5}$$

We can express the above formula in a more convenient form:

$$n_{cutoff} = 1.26 \cdot 10^{-8} f_p^2 \tag{1.3.6}$$

If we apply a magneto-static field to the plasma, then it will become an anisotropic medium for the electromagnetic waves propagation. Necessarily, the dielectric constant will transform in a tensor ($\bar{\epsilon}$), as the field propagation will depend on the direction of the wave injection into the plasma. $\bar{\epsilon}$ can be determined, in the cold plasma approximation and in the high frequency limit (neglecting the ions response to the electromagnetic field because of their high inertia), by means of the single particle approach. We start from the equation describing the motion of a single particle subject to the action of magneto-static field $\vec{B_0}$, under the effect of collisional function introduced in the term $m_e\vec{v}\omega_{eff}$, and in presence of an oscillating electric field $\vec{E}$ associated to the incoming wave:

$$m_e \frac{d\vec{v}}{dt} = q_e\vec{E} - m_e\vec{v}\omega_{eff} + q_e\vec{v} \times \vec{B_0} \tag{1.3.7}$$

By adding the term connected with the magneto-static field (oriented, for sake of simplicity, along the $\hat{z}$ axis), one can find the $\vec{k}$ vectors of waves propagating in magnetized plasmas [10]. It comes out that $\vec{k}$ depends on the angle formed by the incoming wave with the magnetic field direction. In addition, two different constants of propagation exist for the wave [10]:

$$k'_\theta = \frac{\omega}{c}\left[1 - \frac{X(1+iZ-X)}{(1+iZ)(1+iZ-X) - \frac{1}{2}Y_T^2 + \sqrt{\frac{1}{4}Y_T^4 + Y_L^2(1+iZ-X)^2}}\right]^{\frac{1}{2}} \tag{1.3.8}$$

$$k"_\theta = \frac{\omega}{c}\left[1 - \frac{X(1+iZ-X)}{(1+iZ)(1+iZ-X) - \frac{1}{2}Y_T^2 - \sqrt{\frac{1}{4}Y_T^4 + Y_L^2(1+iZ-X)^2}}\right]^{\frac{1}{2}} \tag{1.3.9}$$

similarly to the case of electromagnetic waves propagating in non isotropic crystals. Here $X = \left(\frac{\omega_p}{\omega}\right)^2$, $Y = \left(-\frac{\omega_c}{\omega}\right)$, and $Z = \left(\frac{\omega_{eff}}{\omega}\right)$, where ω is the wave frequency, ω_c is the cyclotron frequency and ω_{eff} is the collision frequency. The imaginary parts of $\vec{k}$ are connected with the wave collisional damping. Neglecting the collisions, for a wave incidence angle of 0° we obtain:

$$k'_0 = \frac{\omega}{c}\sqrt{1 - \frac{X}{1+Y}} = \frac{\omega}{c}\sqrt{1 - \frac{\omega_p^2}{\omega(\omega-\omega_c)}} \tag{1.3.10}$$

$$k''_0 = \frac{\omega}{c}\sqrt{1 - \frac{X}{1-Y}} = \frac{\omega}{c}\sqrt{1 - \frac{\omega_p^2}{\omega(\omega+\omega_c)}} \tag{1.3.11}$$

if the wave incidence angle is 90° we obtain:

$$k'_{\frac{\pi}{2}} = \frac{\omega}{c}\sqrt{1-X} = \frac{\omega}{c}\sqrt{1 - \frac{\omega_p^2}{\omega^2}} \tag{1.3.12}$$

$$k"_{\frac{\pi}{2}} = \frac{\omega}{c}\sqrt{1 - \frac{\frac{\omega_p^2}{\omega^2}}{1 - \frac{\omega_c^2}{\left(\omega^2-\omega_p^2\right)}}} \tag{1.3.13}$$

Hence for a given arbitrary direction, defined by θ, we have two waves characterized by k'_θ and k''_θ. As a function of X, k'_θ is more similar to a wave propagating in an isotropic plasma, then the associated wave will be called **ordinary wave**; the wave with k''_θ is named **extraordinary wave**. Considering the two extreme conditions (0° and 90°) we actually have four different waves: in plasma physics another classification prevails, according to the scheme shown in table 1.1. Usually, the waves propagating along the magnetic field direction are named R and L waves, according to their

Table 1.1: *Cutoffs and resonances of the waves propagating inside the plasmas [11].*

vectors orientation	refraction index	wave type
$\vec{B}_0 = 0$	$\omega^2 = \omega_p^2 + k^2c^2$	light wave
$\vec{k} \perp \vec{B}_0$, $\vec{E} \parallel \vec{B}_0$	$\frac{c^2k^2}{\omega^2} = 1 - \frac{\omega_p^2}{\omega^2}$	O wave
$\vec{k} \perp \vec{B}_0$,$\vec{E} \perp \vec{B}_0$	$\frac{c^2k^2}{\omega^2} = 1 - \frac{\omega_p^2}{\omega^2}\frac{\omega^2 - \omega_p^2}{\omega^2 - \omega_h^2}$	X wave
$\vec{k} \parallel \vec{B}_0$	$\frac{c^2k^2}{\omega^2} = 1 - \frac{\omega_p^2/\omega^2}{1-(\omega_c/\omega)}$	R wave
$\vec{k} \parallel \vec{B}_0$	$\frac{c^2k^2}{\omega^2} = 1 - \frac{\omega_p^2/\omega^2}{1+(\omega_c/\omega)}$	L wave

polarization (circularly right for R and left for L). The waves propagating along the perpendicular direction to $\vec{B}_0$ are named O and X, according to the orientation of the electric field with respect to the magnetostatic field direction.

The O-mode is characterized by $\vec{k} \perp \vec{B}_0$ and $\vec{E} \parallel \vec{B}_0$. If $\vec{k} \perp \vec{B}_0$ and $\vec{E} \perp \vec{B}_0$ the wave will be called X mode.

Let us consider the cutoffs and resonances of the R, L, O and X waves. For the R waves, the refraction index $\frac{c^2k^2}{\omega^2}$ becomes infinite at $\omega = \omega_c$. In this case the microwave frequency is equal to the Larmor frequency, hence **the wave is in resonance with the cyclotron motion of the electrons**. This resonance is of primary importance for MDIS and takes the name of **Electron Cyclotron Resonance**. More generally the cutoffs and the resonances of the various propagation modes can be summarized by reporting the different $\frac{c^2k^2}{\omega^2}$ formulas obtained from the 1.3.8 and 1.3.9. A schematic summary of the main electron waves is given in table 1.1. There $\omega_h = \sqrt{\omega_c^2 + \omega_p^2}$ is the so called *upper hybrid frequency.*The X mode has a resonance at the upper hybrid frequency , i.e when:

$$\omega^2 = \omega_p^2 + \omega_c^2 = \omega_h^2 \tag{1.3.14}$$

The L wave does not suffer any resonance, as well as the O mode. Instead they suffer a cutoff that can be determined by the equations reported in table 1.1, when the refraction index $\frac{c^2k^2}{\omega^2}$ goes to zero.

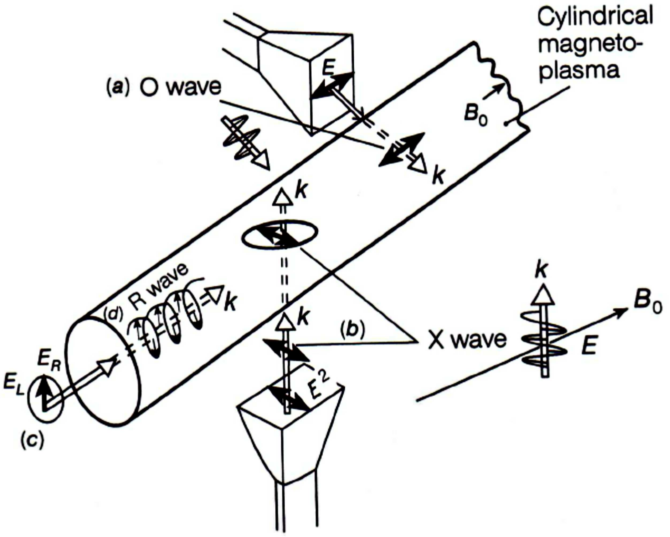

Figure 1.3.1: *Schematic representation of the possible ways to inject electromagnetic waves into a column of a magnetized plasma. The different modes can be excited, according to the location of the waveguide providing the electromagnetic field, and also according to the wave polarization inside the waveguide [9].*

The figure 1.3.1 shows schematically the direction of propagation of the four modes in a cylindrically shaped plasma column. A powerful method to visualize the cutoffs and the resonances of the various modes is to plot them on the so called CMA diagram[2] [11]. This diagram is reported in figure 1.3.2.

When the propagation occurs at a given angle with respect to the magnetic field, the phase velocities change with the angle. Some of the modes listed above with $\vec{k} \parallel \vec{B}$ or $\vec{k} \perp \vec{B}$ change continuously into each other. Such

---

[2] The CMA diagram takes the name from Clemmow, Mullay and Allis who proposed the graphical representation of the many cutoffs and resonances of electromagnetic waves propagating in a cold plasma.

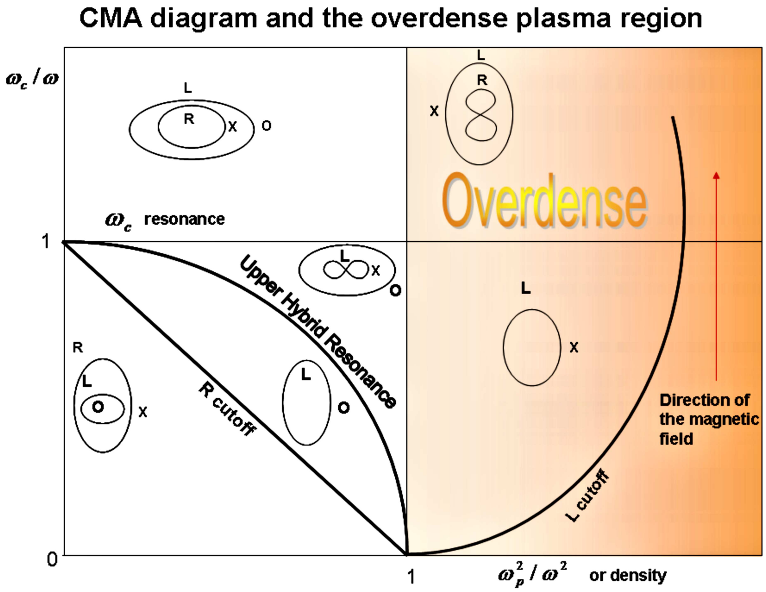

Figure 1.3.2: *A detailed view of the Clemmow-Mullaly-Allis diagram showing the region of the so-called overdense plasma, i.e. that region where the plasma density exceeds the cutoff of the ordinary (O) mode.*

a complicated picture is greatly simplified by the CMA diagram, which however works only in case of cold plasma approximation ($T_e = T_i = 0$). Any finite temperature modification implies a so great number of complications that the diagram cannot be further reliable.

The diagram can be viewed as a plot of the ω_c/ω versus ω_p^2/ω^2 , or equivalently a plot of the magnetic field versus the plasma density. For a given frequency ω, any experimental situation characterized by ω_c (i.e. the magnetic field) and by ω_p (i.e. the plasma density) is denoted by a point on the graph. The total plane is divided into several zones, and the boundaries of each zone are the cutoffs and the resonances mentioned above. For example, considering an X wave propagating from a region of high magnetic field, inside a plasma with a fixed value of density, the value of the magnetic field where the UHR occurs can be easily determined on the graph. The vertical line at $\omega_p^2/\omega^2 = 1$ is the so called O cutoff, and it corresponds to the cutoff density in an unmagnetized plasma. Above this value the plasma will be called **overdense**. The small diagrams in each region delimitated by the cutoffs and the resonances (i.e. the eight-shaped or ellipsoidal small diagrams) indicate not only which wave propagates, but also the qualitative variation of the phase velocity with the angle (considering that the magnetic field is directed along the vertical direction).

1.3.1 Bernstein waves

Electron Bernstein waves (EBW or BW) are electrostatic waves propagating across the magnetic field in a hot plasma. Then the cold plasma approximation cannot be used, and the fluid and single particle approach fail. They are so named after Ira B. Bernstein, who described these modes in 1958 [12]. The Bernstein waves are sustained by electron cyclotron motion and they can be thought as the fronts of electron rarefaction and compression perpendicular to the magnetic field with wavelength λ of the order of electron Larmor radius ρ. Clearly, a finite Larmor radius should be considered. In a Maxwellian plasma this also implies that the temperature be finite. In fact in a cold magnetized plasma the electrons are tight to the field lines and the charge separation (and space-charge waves) is possible only along the field. At high enough temperatures, the electron gyroradius $\rho = mv_{th}/\left(eB\right)$ (where v_{th} is the electron thermal velocity and the other notations are standard) becomes comparable with the wavelength λ. The EBW occurs when the electron gyrophase is organized in such a way that the space charge distribution has maxima and minima, which are periodically distributed perpendicularly to external magnetic field lines [13]. If additionally the wave frequency ω is of the order of the cyclotron frequency ω_c, the electrons can move in phase with the local wave field and "participate" in wave motion, in the following sense: by moving in response to the wave field, the electrons alter the local concentration of electric charge, giving their own contribution to the electric field of the wave . This means that the electrons gyromotions cannot be random as in the absence of the wave, otherwise the wave cannot propagate. We need some regular bunching of the electron charge in order to facilitate the wave propagation.

One of the most important properties of EBW is that they

can propagate in overdense plasmas without any cutoff. As long as $\omega \geq \omega_c$, the BW propagate in overdense plasmas as $\omega_c > \omega_p$, then the electrons are still able to transfer information for the wave propagation outside any Debye sphere. Because of their electrostatic nature, **the Bernstein waves cannot propagate outside the plasma, and their boundary is constituted by the UHR layer** [13].

By determining O and X modes from a kinetic approach, it can be demonstrated that the *O* mode is a pure electromagnetic wave, whereas *X* has a small electrostatic component. Near the UHR layer the *X* mode also adopts an electrostatic character. Its refractive index becomes large and the longitudinal electric field dominates. Then near the UHR the *X* and EBW-modes coincide; the *X*-wave is coupled into an EBW and vice versa. In a full wave view the *X*-wave expresses a longitudinal polarization which becomes dominant when the *X*-wave reaches the UHR [13]. In the vicinity of the UHR the phase velocity is strongly reduced until it approximates the thermal velocity. Here the wavelength reduces down the order of the electron gyro radius and an EBW is excited.

1.3.2 Eigenmodes

Wave in MDIS ion source may be also described macroscopically, i.e., by considering the plasma chamber as a multimode cavity where many electromagnetic modes exists and can be selected depending on the rf coupling system. Eigenmodes of a cylindrical cavity (ECR plasma chamber) are $TE_{m,n,p}$ or $TM_{m,n,p}$ where the indices stand, respectively, for the Ψ azimuthal, r radial, and z axial or parallel coordinates. They are actually standing waves formed by oblique waves with respect to the parallel direction, as their dispersion relation in vacuum can always be written in the form [14],

$$k_0^2 = k_\perp^2 \left(m, n\right) + k_\parallel^2 \left(p\right) \ , \tag{1.3.15}$$

where k_0 is the vacuum wave number.

In an ideal situation, rf coupling in ECRIS is performed by injecting a wave that is coupled only to the right wave (parallel propagation), and it is almost completely absorbed when crossing the resonance surface.

In a real situation, a linearly polarized wave is injected in parallel direction (along the main axis of the source), and it may reasonably be coupled to the whistler wave[3]. However, only some power of the R wave may be reflected on the walls of the plasma chamber. So there is a possible coupling to the cavity modes of the plasma chamber.

In order to to launch the microwave into the plasma coaxial and rectangular waveguides are used. With the last types of waveguides, the TE_{10} mode is used and it is more efficient than coaxial one.

1.4 Ion beam extraction

The ion produced in plasma chamber are extracted with the aid of high voltages. The extraction potential, which tends to penetrate through the plasma electrode aperture, is repelled by the plasma sheath potential; so an equipotential surface is formed which defines a curved boundary: **the plasma meniscus**. The relative strength of the plasma (the plasma potential) and extraction potentials defines the radius of curvature of the meniscus. Particles that cross the meniscus see that the extraction field form the beam. The initial focusing of the beam depends on the curvature of the meniscus and hence on the current density inside the plasma. Meniscus' position and shape depend upon all the parameters of the discharge, the extraction voltage, and the shape of the metal electrodes in the extraction zone.

The meniscus may assume a variety of shapes which are illustrated in figure 1.4.1 (for fixed extraction voltage). For overdense plasma (a) the meniscus is convex and a significant number of ions are lost as they hit the extraction electrodes. In the case of intermediate plasma density (b) the beam is better matched to the extraction, which makes this shape of plasma meniscus the most attractive regarding the extraction design. Finally, for underdense plasma (c) the meniscus is concave and although the beam is not lost at the extraction area, the space charge will create significant problems (i.e. beam blow up) further, down to the beam line. However, the magnitude

---

[3] The whistler wave is a very low frequency electromagnetic wave: the phase velocities much less than the speed of the light in free space.

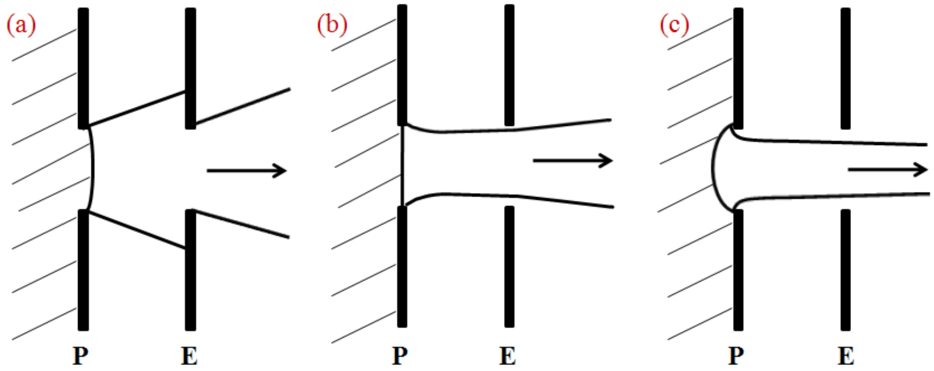

Figure 1.4.1: *Illustration of possible plasma boundary curvatures during ion extraction which may affected by changes in plasma density: (a) convex meniscus; (b) glad meniscus; (c) concave meniscus. The notation P refer to plasma electrode and E to extraction electrode.*

of this effect depends on the beam current. Plasma distortions, in addition, due to complex plasma boundary shapes, will lead to beam aberrations and may seriously deteriorate the quality of the beam.

The final angular divergence is affected by the space charge. In MDIS the space charge of intense beams has to be compensated. In many cases it is done by addition of gas in the low energy beam transfer line. The neutral are ionized by impinging beam ions and this process can generate a sufficient number of compensation electrons; but the electrons must be kept from being accelerated back into the source by the extraction field. This shielding can be achieved by means of the so-called *accel/decel* system, where a screening, or suppressor electrode is introduced into the extraction gap and biased to a sufficiently low potential to create a negative-potential well and form an electron trap (for high-q ion beams the compensating electrons are especially desirable).

1.5 The Emittance and Brightness of ion source

The quality of the ion beam extracted from an ion source is characterized by the beam emittance and brightness. These quantities are frequently used to determine the compatibility with given beam transport and optical systems. For high quality ion beams the emittance should be as small as possible and the brightness as high as possible.

These quantities are related to each other and their significance is a direct consequence of **Liouville**'s theorem. This fundamental theorem states that *the motion of a group of particles, under the action of conservative force fields*[4]*, is such that the local number density in the six-dimensional phase space volume* ($xyzP_xP_yP_z$) *everywhere remains constant.* An ion beam can be represented by a group of points, all of which stay within the six-dimensional hypervolume. The effective phase space volume of an ion beam may increase due to interactions with residual gas particles, beam transport and acceleration system aberrational effects, and space charge effects, but it cannot be never less than its value of the source extraction. Thus, the magnitude of the phase space volume or a quantity proportional to the phase space volume (emittance) measured at the extraction is a unique characteristic of the particular ion source.

1.5.1 Emittance

Often called "emittance", the volume emittance ν_6 is by definition the six dimensional hyper-volume of a certain fraction of the particles in a bunch [15]:

$$\nu_6 = \int\int\int\int\int\int dx \cdot dy \cdot dz \cdot dp_x \cdot dp_y \cdot dp_z \tag{1.5.1}$$

If the transverse components of the motion of a group of particles are mutually independent in configuration space (i.e., neglecting space charge and spin-dependent interactions)[5], the motion of the particles in the orthogonal planes (x, P_x), (y, P_y), and (z, P_z) will be uncoupled and therefore they can be treated separately.

For uncoupled motion in which a beam is moving along the z direction under the action of conservative forces, the four-dimensional hyperarea

---

[4] Conservative forces include the static electro-magnetic fields that are normally used to reshape and transport charged particle bunches to the desired location.

[5] This means that the particles are only subjected to hamiltonian interactions, i.e conservative forces.

(xP_xyP_y) or transverse phase space area is a conserved quantity, according to Liouville's theorem.

$$\nu_6 = \int\int\int\int dx \cdot dy \cdot dp_x \cdot dp_y \cdot \int\int dz \cdot dp_z = \nu_4^T \cdot A^L \tag{1.5.2}$$

where A^L is 2-dimensional longitudinal emittance area and ν_4^T is 4-dimensional transverse emittance volume. If the coordinates are not coupled, the 4-dimensional emittance volume can again be separated into 2-dimensional emittance areas:

$$\nu_4^T = \vec{p}^2 \cdot A^x \cdot A^y \tag{1.5.3}$$

if the particle energy remains constant along the beam axis, normally one can factorize out the momentum p. All these terms are normally called *Emittance*. Because of the predominately elliptical shape of emittance figures, most authors, proceed to define the *emittance* as the half-axis product of an ellipse with an area equal to the emittance area occupied by a certain fraction of the particle distribution:

$$E^x = \frac{A^x}{\pi}, \qquad E^y = \frac{A^y}{\pi} \tag{1.5.4}$$

The units of emittance are often given in terms of $\pi\, mm\, mrad$[6]

When the charged particles are accelerated, the axial velocity component increases dramatically, while any transverse field components at the entrance and the exit of the acceleration field can be factored out as the conservative force field of an emittance-conserving lens. As shown in figure 1.5.1, the increase of the axial velocity components decreases the trajectory angles, and hence the x' is reduced. By normalizing the emittance, this energy dependence is eliminated. The normalized rms-emittance E_{norm} is defined as it follows:

$$E_{norm} = \beta \cdot \gamma \cdot E \tag{1.5.5}$$

with $\beta = v/c$ is the ratio between the particles' velocity v and the speed of light c, and $\gamma = \sqrt{1-\beta^2}$ is the relativistic correction factor.

---

[6] The π is supposed *to assure the reader that the has the π has been factored out of the phase space area* (Sanders, 1990). However, if the π was factored out, it was factored out in the definition

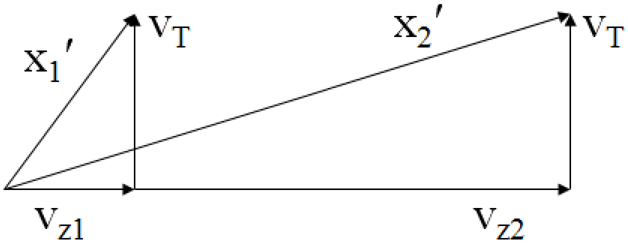

Figure 1.5.1: *Trajectory angles shrink as the axial velocity increases. The shrinkage of the trajectory angles can be factored out by multiplying the emittance with the relativistic velocity of the charged particles.*

The normalized emittance remains roughly the same throughout the entire accelerator. It can decrease through the collimation, but more typically it increases gradually throughout the accelerator; the increases are caused mostly by slightly mismatched, coupled systems and by non-conservative force fields, such as stripper foils. The emittance of 100% of a Gaussian distribution is infinite because the distribution extends to infinity. The 100% emittance of a real beam is dominated by particles that are often very far from the central trajectory and encounter highly non-linear fields, and therefore are easily lost. For this reason the emittance is normally given for a fraction of the beam, and frequently the 90% is taken. The emittance changes rapidly with the fraction of the enclosed beam and therefore it is important to characterize the emittances with the % level of the included beam fraction.

This limitation was eliminated through the introduction of the rms emittance by Chasman and refined by Lapostolle. For the (x,x') it is defined as:

$$\epsilon = \sqrt{\langle x'^2\rangle\langle x^2\rangle - \langle xx'\rangle^2} \quad , \tag{1.5.6}$$

with:

$$\langle x^2\rangle = \frac{\sum\limits_{all} (x-\bar{x})^2 \cdot c\left(x,x'\right)}{\sum\limits_{all} c\left(x,x'\right)} \quad , \tag{1.5.7}$$

$$\langle x'^2 \rangle = \frac{\sum\limits_{all} \left(x' - \bar{x}'\right)^2 \cdot c\left(x, x'\right)}{\sum\limits_{all} c\left(x, x'\right)} \quad , \tag{1.5.8}$$

and

$$\langle x \cdot x' \rangle = \frac{\sum\limits_{all} \left(x - \bar{x}\right) \cdot \left(x' - \bar{x}'\right) \cdot c\left(x, x'\right)}{\sum\limits_{all} c\left(x, x'\right)} \tag{1.5.9}$$

where x is the transverse location, x' is the approximated angular particle momentum and c(x, x') corresponds to the amount of particles passing the location x with an angular momentum x'. The terms $\langle x \rangle$ and $\langle x' \rangle$ in the above equations represent the mean value for the corresponding number to which the rms-emittance is normalized. The equations below show how these numbers are obtained:

$$\bar{x} = \frac{\sum\limits_{all} x \cdot c\left(x, x'\right)}{\sum\limits_{all} c\left(x, x'\right)} \quad , \tag{1.5.10}$$

$$\bar{x}' = \frac{\sum\limits_{all} x' \cdot c\left(x, x'\right)}{\sum\limits_{all} c\left(x, x'\right)} \tag{1.5.11}$$

The equation 1.5.6 is the semi-axis-product of an ellipse. For a Gaussian distribution, the ellipse contains 39% of the beam. The rms emittance is finite for the entire beam, as long as the total beam current is finite $\int\int c\left(x, x'\right)$.

A 4-rms or 6-rms emittance is frequently used which means 98% and 99.8%, respectively of the beam for a Gaussian distribution.

1.5.2 The emittance ellipse and its transformation

Liouville's theorem provides a powerful tool to describe a beam in the phase space. The knowledge of the area occupied by particles in phase space at the beginning of a beam transport line will allow us to determine the

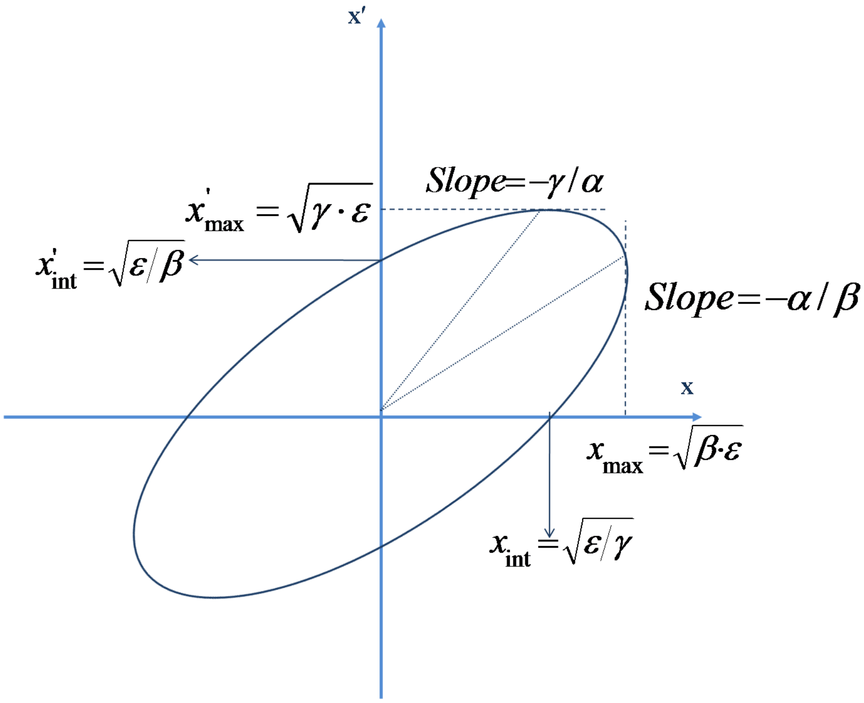

Figure 1.5.2: *Phase space ellipse.*

location and distribution of the beam at any other place along the transport line without calculating the trajectory of every individual particle. It has become customary to surround all particles of a beam in phase space by an ellipse called the phase ellipse (figure 1.5.2) described by:

$$\gamma x^2 + 1\alpha x x' + \beta {x'}^{2} = \epsilon \tag{1.5.12}$$

where α, β, γ, and ϵ are the ellipse parameters. The parameters α, β, and γ are called *betatrone functions* or Twiss parameters. When the beam is transmitted through different ion optical components the ellipse rotates in phase space and (figure 1.5.3) the Twiss parameters determine the shape and orientation of the ellipse.

The dimensionless α, for example, relates to the x,x' correlation, and it is negative for diverging beams, zero in beam waists or antinodes, and positive

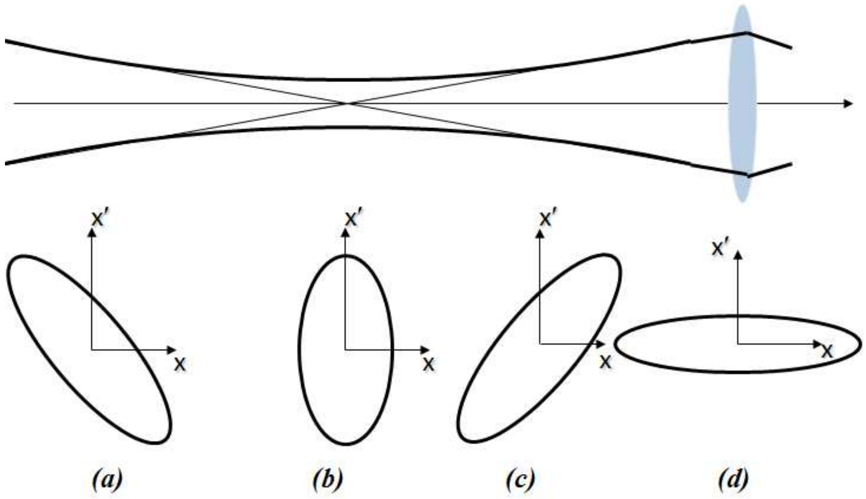

Figure 1.5.3: *The orientation for the emittance ellipse in the case of (a) converging, (b) focused, (c) diverging; and(d) parallel ion beam.*

for converging beams. The parameter β is by definition positive ($\beta > 0$) and it is measured as length per angle (such as m/rad). The parameter γ is also positive, measured in angle per length (e.g. rad/m) and dependent on α and β:

$$0 < \gamma = \frac{1+\alpha^2}{\beta} \tag{1.5.13}$$

When a beam drifts through a field-free region, the Twiss parameter γ remains constant because it is constant the related maximum divergence x'_{max}:

$$x'_{max} = \sqrt{\gamma \cdot \epsilon} \tag{1.5.14}$$

The Twiss parameter β, however, changes because the related maximum radius x_{max} changes throughout a drift region:

$$x_{max} = \sqrt{\beta \cdot \epsilon} \tag{1.5.15}$$

For beams extracted from ion sources, a useful estimation of the emittance is given as [16], [17]:

$$\epsilon^{xx'-rms-norm} = 0.016r\sqrt{\frac{kT_i}{M/Q}} + 0.032r^2B_0\frac{1}{M/Q} \tag{1.5.16}$$

where r is the radius of extraction aperture [mm], kT_i the ion temperature [eV], B the axial magnetic field at extraction [T] and M/Q is the ratio of ion mass in amu to charge state of the ion beam. The equation 1.5.16 shows that there are two main contributions to the ion beam emittance for an ECR ion source extraction system:

1. the ion beam transverse temperature[7],
2. the induced beam rotation (angular momentum) due to the decreasing axial magnetic field on the extraction region[8].

The sources described in the chapter 3 use microwave at 2.45 GHz to generate a plasma. This frequency acts only on the electrons, as we have reported in the section 1.3, so our plasmas have cold ions, with effective temperature below in the order of ~ 1 eV. In particular for the VIS source, shown in the section 3.1, there is a magnetic system that reduces significantly the stray field in the extraction area.

The emittance increases with the beam current, which is evidently to be related to space charge effects during the beam transport.

1.5.3 Brightness

For a comparison of different source, it is often to used to the **normalized brightness**. Because the emittance depends on source area, it is possible to reduce the emittance to an arbitrarily low value. However, this is done at the expense of beam current, and hence, it is not always a practical option. The brightness of the beam gives a measure of how much current can be concentrated in a small spot, and is defined as:

$$B_n = \frac{I}{\epsilon^{xx'} \epsilon^{yy'}} \tag{1.5.17}$$

Like the emittance, the brightness is an invariant along the beam path, and a higher brightness is associated with a higher performance beam.

---

[7] In the equation 1.5.16 the emittance due to ion temperature have been calculated assuming a Maxwellian temperature distribution inside the plasma [16].

[8] In the equation 1.5.16 the emittance due to decreasing of magnetic field is described by the Busch's theorem [16].

Chapter 2

Microwave Discharge ion sources

The production of high current beams is a key point for different applications and this role is deemed to increase in the coming years, either for industrial applications and for the research projects [18]. Some of the accelerator projects aiming to the production of high power beams for research purpose will use H^- sources with currents in the range of many tens of milliampere. Table 2.1 shows a list of some of these projects. High current and high brightness H^+ beams can be provided by 2.45 GHz microwave discharge sources, which present many advantages in terms of compactness, high reliability, ability to operate in CW mode or in pulsed mode, reproducibility, and low maintenance. Table 2.1 lists also the projects that will use high current proton beams (up to 100 mA) with low transversal emittance. The beam formation is an essential process for the optimum operation of the following accelerator as it *shapes* the beam either in the transversal phase space and in time. A stringent request in terms of (*rms* normalized) beam emittance at the entrance of the radio frequency quadrupole (RFQ) may be of the order of 0.20 to 0.30 π mm mrad, which makes essential to design and test the ion source and low energy beam transport (LEBT) as a whole. This is really a new trend that is faced by high power accelerator, whilst in the case of low current accelerators, the proton/ion source could

Table 2.1: *High power accelerator requirement.*

	p/H^-	mA	ms	Hz	Duty factor	π *mm mrad*
LEDA	p	100	CW	CW	100%	0.25
IPHI	p	100	CW	CW	100%	0.25
TRASCO	p	30	CW	CW	100%	0.2
ESS	p	60/90	1.2	50	4%	0.3
SPL	H^-	50	1.5	50	7.5%	0.2
SNS	H^-	50	1	60	6%	0.25
JKJ	H^-	30	0.5	50	2.5%	0.25

be considered as a black box which behavior has almost no consequences on the beam acceleration, except for beam trips or energy spread changes.

Nowadays it is well known that the beam formation mechanism in a high current source (HCS) plays a role in the acceleration process, particulary when the beam halo or the beam ripple may affect the performances of accelerators with large beam load. The major challenge of the accelerator front-end is essentially the preparation of a high quality beam, with a pulse well defined in time and a small transversal emittance (a minimized halo limits the beam losses throughout the high energy part of the linac and the overall reliability can be maximized). Therefore the simulations of the beam injector should ideally start from the plasma chamber and it should include the first acceleration stage. It is worthwhile to review the different experiences reported in the last decades as for the production of high current beams, with a special attention to the production of proton beams that are largely used in many applications.

Important applications for which industrial source are purchased fell into three categories [1].

In the first category is the cleaning of surface by means of inert or reactive ion beams. The process is known as **etching**. The second category concern the deposition of coatings, by using the flux sputtered off a target by the ion beam. This is known as **ion beam sputter deposition**. The Third category involves the concurrent use an ion beam to improve the properties of a coating that is being deposited using different technique (direction deposition). This is **ion-assisted deposition**.

The ion sources can be employed to characterize the structure of the atoms or the molecular structure of the materials. It is possible, for example, to use as scientific probe X-rays and neutrons[1]. Neutron beams can be produced through fission in the nuclear reactor or by means particles accelerators. In an accelerator, the neutrons are generated in process of spallation.

The possibility of generating a high neutron flux with a broad energy spectrum by means of a high current proton beam (1 GeV)impinging on a spallation target opens new perspectives in the use of high energy, high current proton accelerators. A CW proton beam power in excess of a few tens of MW could produce the neutron flux to a subcritical nuclear reactor, moreover the high neutrons flux also allows the incineration of nuclear waste (actinides and long lived fission fragments) produced by conventional critical reactors, leaving no substantial amount of radiotoxic waste at the end of the cycle. In 1998 the Research Ministers of France, Italy and Spain, recognizing the potentialities of Accelerator Driven System (ADS) for the transmutation of long-lived nuclear waste, decide to define a common R&D European platform on ADS, promoted by Carlo Rubbia through the idea of the Energy Amplifier.

2.1 Plasma heating for source operating at 2.45 GHz

Different theoretical analysis described the plasma ignition in HCS [9]. More generally, two different groups of plasma sources operating at 2.45 GHz (the

---

[1] X-rays interact with the orbital electrons so that this method don't allow to do a simple diagnosis of light atoms (the light atoms have few electrons). Neutrons interact with atoms by means of nuclear force to short range so they yield information about the positions of nuclei, that it is complementary comparing that of X-ray.

most used frequency) are defined, depending on the shape and value of the maximum magnetic field with respect to B_{ECR}. In some cases the sources operate at magnetic field below the ECR everywhere ($B < B_{ECR}$): the incoming wave is no longer a pure electromagnetic mode, but the interactions with the dense plasma triggers nonlinear phenomena and electrostatic oscillations. The incident electromagnetic wave absorption can be described by means of a collective approach: the electrons gyromotion is disturbed by fluctuating fields and by the plasma *effervescence* [9] with high frequencies (comparable with the microwave frequency). Then Bernstein waves (BWs) can be excited. The BW penetrate in the warm plasma core without any cut-off,and they can be absorbed at cyclotron harmonics fields $B_{ECR}/2$ or $B_{ECR}/3$. An experiment demonstrating the density optimization by varying B is reported in ref. [19] where clear evidences of energy absorption at cyclotron harmonics are shown. Because of the electrostatic nature of plasma heating, the density rises well above the cut-off. This option is useful but a plasma created in such a way is turbulent and nonuniform (some parts of the plasma chamber remain empty, as observed in ref. [20] because of the peripherical BW absorption).

The other case is the off-resonance wave-plasma interaction with $B > B_{ECR}$. Resonances between the electromagnetic waves and the plasma electrons can occur even for high plasma densities [21] [22], provided that a first ignition due to the single particle ECR heating occurs. Qualitatively the presence of ECR regions can be pictured as an ECR *gas-lighter* which gives a spark, that afterwards is maintained by the *fuel* created by an off-resonance discharge, covering the whole chamber. A more suitable theory generalizes the classical ECR heating theory, based on the electron collisionless motion during the wave-particle interaction, to the collisional case. In dense and turbulent plasmas a strong effervescence is triggered by density gradients, leading to a collective scattering of the single electron whose frequency is ν_{ω_p}. It strongly depends on the plasma frequency ω_p: when $\nu_{\omega_p} < \omega_p$ the electron gyromotion is strongly perturbed by the collective collisions and during the ECR acceleration the electron may go out of phase with respect to the wave. This means that the effective gyroperiod is longer than in the collisionless case.

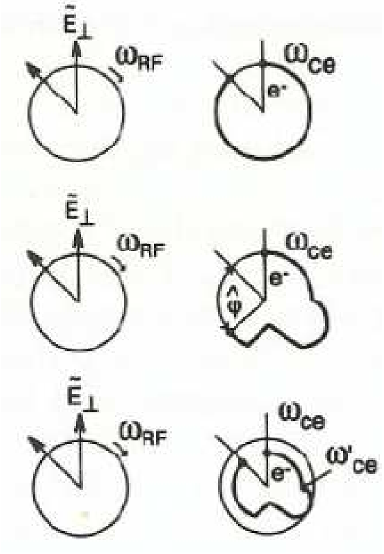

Figure 2.1.1: *R wave electric field vector rotations and electron gyrations in ECR (bottom), off-ECR (middle), and with* $B > B_{ECR}$ *[9].*

In order to recover the synchronization with the rotating wave electric field, a magnetic field higher than B_{ECR} is needed, and the acceleration restart. The key point of this approach is whether or not electromagnetic waves propagating parallel to the magnetic field (R-right hand polarized waves) exist in overdense plasmas. According with the CMA diagram, the R waves propagate only in the off-resonance region (i.e., above B_{ECR}). In fact, Sakudo [23] demonstrated that the higher plasma density is obtainable when $B_{ECR} < B < 1.3B_{ECR}$. The results obtained during the TRIPS magnetic profile optimization confirmed that the best performances can be obtained when $B > B_{ECR}$ everywhere. This allows an easy propagation of the R wave, without suffering any cut-off before the collisional, quasiresonant absorption at off-resonance B values.

In microwave discharge ion sources, the magnetic field role is not crucial as for higly charged ion beams production (ECRIS) [9], but nevertheless it is effective on the ionization process because it forces the electrons to spiralize around the field lines, thus increasing the electron lifetime and, because of the plasma quasineutrality, the ion lifetime τ_i. This finally increases the ionization probability. Anyway the magnetic field does not need a confining structure because in HCS single or double charged ions are to be created. More important is the plasma density, which is the crucial parameter for high currents, scaling with the density over ion lifetime ratio [9].

2.2 Low frequency ECRIS: historical notes

The 2.45 GHz microwave ion sources are used in many areas of fundamental and applied research and for a growing number of industrial applications. At the end of the 1970s, a slit-shaped 2.45 GHz microwave ion source adapted for a high-current ion implanter was developed by Sakudo [24] [9]. In this ion source, a solenoid and ferromagnetic materials are effectively placed to form a magnetic field of more than 875 G over the entire discharge chamber.

Some cases the applications require compact, microwave-plasma sources that are compatible with ultrahigh-vacuum technology. An eccellent small-size high-intensity microwave ion source, using a permanent magnet, has been developed by Ishikawa [25]. In this ion source the magnetic field required for ECR produced by the Co-Sm permanent magnet, so that a low input power small size microwave ion source is obtained. The size is 50 mm in diameter and 65 mm in height. In addition, since a plasma density of the order of 10^{12} cm^{-3} is generated, the source was able to produce a total extracted ion currents of more than 1 mA for Ar, N_2, O_2 and CO_2 gases and Cs and Rb metals. The ion source is suitable for megaelectronvolt implanters but it also convenient as an ion beam deposition source.

An outstanding ECRIS for proton injection into a RFQ accelerator was proposed by Taylor at Chalk River National Laboratory [26], [27]. This source can be considered as the basis of all different designs proposed in the last 15 years.

The plasma generator is simply a hydrogen filled chamber, with a superimposed magnetic field. The 1 kW CW magnetron is coupled to the plasma generator via a circulator, a directional coupler and a three-stub

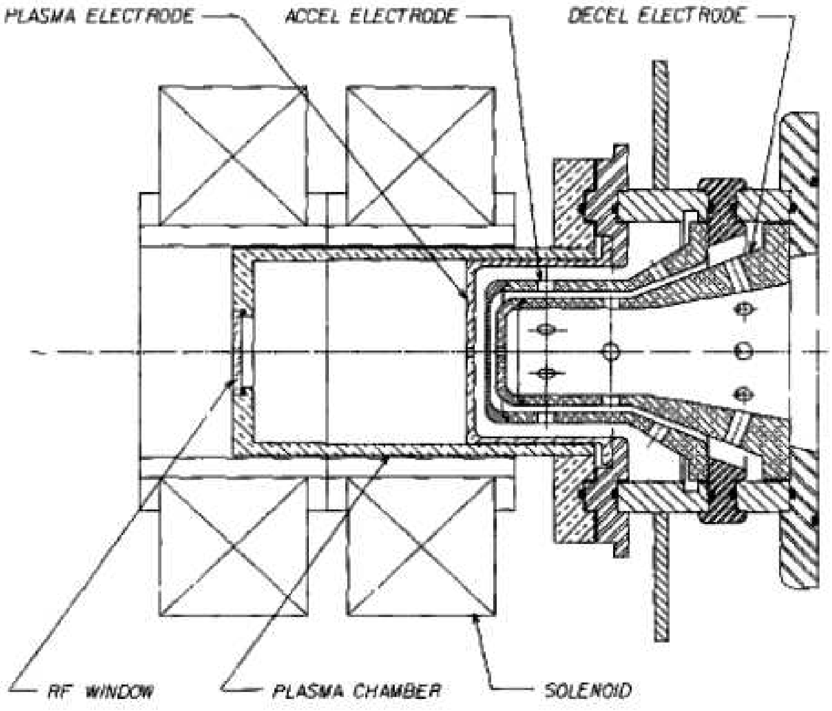

Figure 2.2.1: *Schematic of high current low-emittance dc ECR proton source [26].*

tuner and a 50 kV dc waveguide break has been introduced so that all of the active elements are at ground potential. The break consists of a 3 mm thick sheet of Teflon clamped between a choke flange and a standard flange by two acrylic plates . Stubs located a quarter of a wavelength on either side of the break are adjusted to tune out any impedance mismatch introduced by the break. A rectangular-to-ridged waveguide transition has been inserted immediately ahead of the microwave window to enhance microwave efficiency . The use of two solenoids independently positioned and energized permitted to change the magnetic field configuration,the maximum beam current is obtained when the magnetic induction at the microwave window is B_{ECR} whatever is the axial distribution of the magnetic field. The extraction system is a 50 kV multi-aperture triode. The source generates beam current densities more to 475 mA/cm^2 of hydrogen ions with a proton fraction greater than 85% at microwave power of 500 W. This source can be considered as the basis of all the different designs proposed in the last 15 years.

The main innovation of the CRNL design consists if the microwave line to adapt the waveguide to plasma impedance. The extraction system was not sophisticated but adequate for high current beam formation, using three electrodes in the accel-decel operation mode. This source was further improved by Sherman and co-workers at LANL [28], who improved the extraction system and the LEBT in order to optimize the beam coupling to the RFQ of the LEDA project. The pulsed operation mode was also tested, featuring a rise/fall time in the order of tens of microseconds. The requirements of the LEDA project (table 2.1) set the need to decrease the beam emittance, while getting at the same time a high reliability. Following the same track, at CEA Saclay, the SILHI source obtained larger brightness and high reliability in the second half of 1990s. The source presents a robust engineering of any part, which also includes beam line elements and diagnostics adapted to beam power exceeding 10 kW (typically 95 kV - 140 mA). A proton/deuteron fraction above 80% and an emittance below 0.2 π mm mrad could be obtained, while the reliability increased during years, reaching even 99.9% in a one week test [29]. The SILHI source will be described in the section 3.3. At the end of 1990s TRIPS (TRASTO Intense proton source) was built at INFN-LNS. The goal of the TRASCO/ADS project was less demanding in term of current than it is for the other projects in table 2.1 (maximum proton current of 30 mA in the RFQ, rms normalized emittance below 0.2π mm mrad, operating voltage 80 kV), but un spite of that a significant effort was applied that permitted an original and robust design with about the same reliability as the one obtained for SILHI(this source will described in the next section 2.2.1).

In 1998 two compact 2.45 GHz ECR ion source were built one at IMP for a machine of medical treatment with neutron at Lanzhou University and other at Sichuan University for thin film formation and ion source study [30].

At Toyama Prefectural University an ECR multi-charged ion source using a low frequency 2.45 GHz has been also realized not much different. Basic process are considered to be similar to the devices working at high frequency microwaves ($\geq$ 10 GHz). Due to good accessibility for measurement instruments, the plasma parameters (electron density n_e, electron temperature T_e, plasma potential) have been obtained by means of electric probe. The plasma potential profile has been measured and the potential well around ECR zone has been observed. With this device the plasma parameters and the production of high charge state ion beams have been measured and compared for the microwave power switched respectively in continuous and pulsed mode [31].

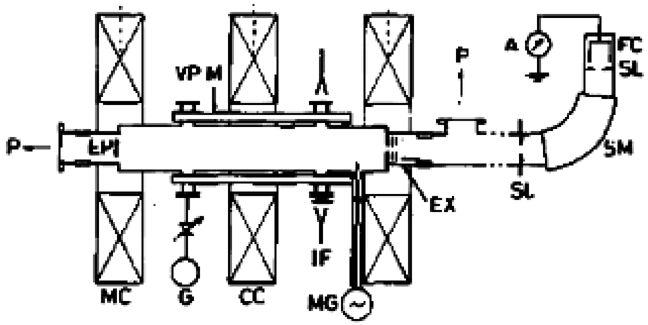

Figure 2.2.2: *ECR Multicharged Ion sources. MC: mirror coils; CC:center coil; M: octupole magnets; MG: magnetron; G: gas inlet; IF: interferometer; EX: extraction electrodes; SM: sector magnet; FC: Faraday cup; A: logarithmic current amplifier [32].*

The purpose of this source was the production of multi-charged ion using low frequency (2.45 GHz) with a consequence reduction of the price of the source. In this Japanese source the magnetic field has been designed to increase the ions and electrons time confinement, in particular the generation of high charge state was created in a B-minimum trap obtained by an octupole field formed by four permanent magnets [32].

In the last years new proton source at 50 keV, 50 mA has been commissioned for the low energy high intensity proton accelerator (LEHIPA) at Bhabha Atom Research Centre (BARC) [33], a new source for proton beam and H_2^+ beam production was developed at China Institute at Atomic Energy (CIAE) to support the innovative proposal for Boron Neutron Capture Therapy (BNCT) [34]. Moreover a compact microwave proton source for proton linac at Korea Atomic Energy Research Institute [35] for the Proton Engineering Frontier Project (PEFP) and a new versatile ion source at Catania INFN-LNS (that will be describe in the section 3.1)have been designed and successfully commissioned.

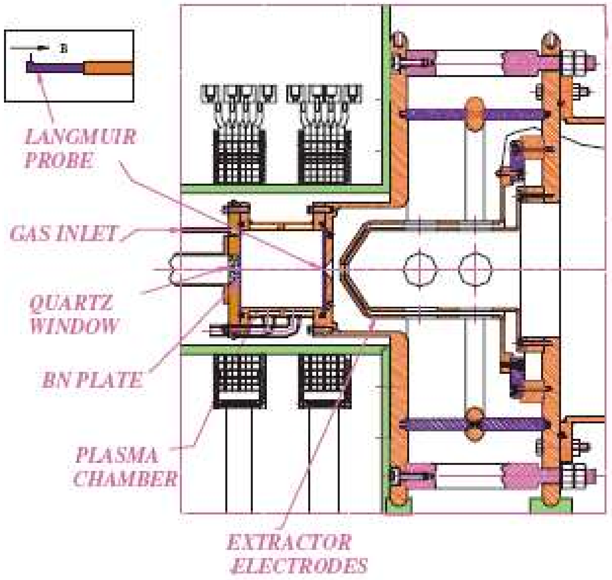

Figure 2.2.3: *The schematic diagram of the* 50 *keV ECR proton source [33].*

Future high intensity ion accelerators in table 2.1, including the Spallation Neutron Source (SNS) [36][37], the European Spallation Source (ESS), the Superconducting Proton Linac (SPL) etc, will require high current and high duty factor sources for protons and negative hydrogen ions.

The SNS is a second−generation pulsed neutron source dedicated to the study of the dynamics and structure of materials by neutron scattering and is currently under construction at Oak Ridge National Laboratory (ORNL). SNS is a collaboration of six U.S. National Laboratories that have developed an accelerator system capable of delivering nearly an order of magnitude higher neutron production beam power compared with that of existing facilities.

The SPL project is part of the luminosity upgrade of the Large Hadron Collider [38]. It consists of an extension of Linac4 up to 5 *GeV* and is foreseen to deliver protons to a future 50 *GeV* synchrotron (PS2). Its source will be a copy of the H^- source that has been successfully developed and operated as part of the injector for the HERA accelerator at DESY.

The present generation of H^- ion sources has evolved into very reliable accelerator subsystems providing continuous operation for many weeks. Unfortunately, when operated under nominal conditions, with known source lifetimes, none of these proven sources simultaneously meets each requirement of new accelerator facilities. (Achieving, simultaneously, high pulse and average current may be the most significant challenge of future source development [39].)

In this thesis only proton source using 2.45 GHz microwave have been studied, as SILHI and VIS, which are widely described in the next chapter. These sources can produce a current grater than 100 mA, stable beam with high availability and small emittance.

2.2.1 TRIPS

Since the middle of 1990 a series of *Microwave Discharge based* Ion Sources (MDIS) have been designed and built at LNS to fulfill the request of intense beams of single charged ions for several applications, from the exotic beam production to the nuclear waste transmutation. The MIDAS ion source [41],[42] was the first MDIS designed and built at LNS. It was a compact microwave discharge source which exploited the principle of the off-resonance discharge to generate an overdense low-temperature plasma, which is an effective tool to generate 1+ ion beams with high efficiency, short delay time and low energy spread. The prototype of the MIDAS source was tested in $1993-95$ but the results were not acceptable with respect to the efficiency request, mainly because of the low RF power coupled to the plasma. A new version (MIDAS2) was built in 1997 with excellent results [40]. After this achievement, a completely new MDIS was designed for high current applications, named TRIPS (TRASCO Intense Proton Source) [3].

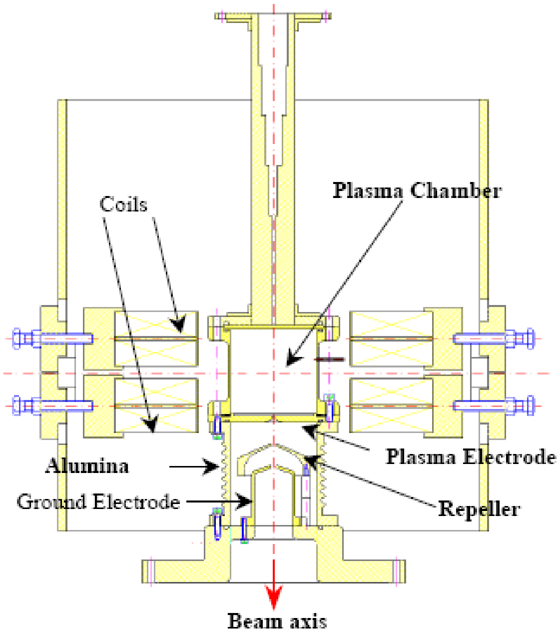

Figure 2.2.4: *The MIDAS2 source [40].*

The aim of TRASCO project (Trasmutazione Scorie) is to develop the technologies needed to design an accelerator driven system (ADS) for nuclear waste transmutation according to the Rubbia et al. proposal [2]. Their proposal was based on a high current continuous wave proton linear accelerator to drive a subcritical system able to transmutate nuclear wastes. The program was developed by INFN and ENEA and has been supported by Ministry of Research since the end of 1997. The system consists of two main parts: the accelerator and the subcritical system. INFN was in charge of the accelerator design, while ENEA handled the subcritical system, as well as some specific aspects related to the safety analysis of this type of nuclear installation on of the RED themes of the accelerator design was the test of a high current proton source with high reliability and low emittance figures. For TRIPS [3] all the three goals shall be fulfilled at the same time: proton current higher than $35mA$, root mean square (rms) normalized emittance below 0.2 π $mm\ mrad$, and reliability close to 100%.

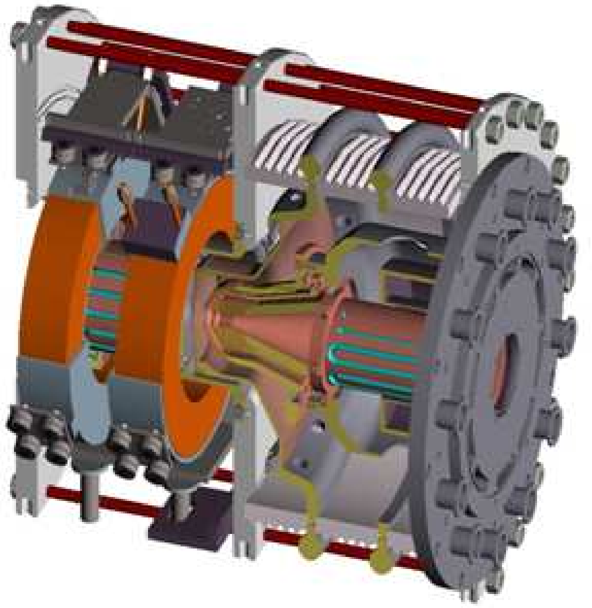

Figure 2.2.5: *Render view of the TRIPS source operating at LNS-INFN*

The source was installed on a 100 kV high voltage platform but it was routinely operated at 80 kV. The plasma chamber was cylindrical, 90 mm in diameter, and 100 mm in length. The microwave pressure window was placed behind a water-cooled bend in order to avoid any damage due to back-streaming electrons. The microwave power produced by a 2 kW 2.45 GHz magnetron was coupled with the plasma chamber through a circulator, a directional coupler, a four-stub automatic tuning unit, and a four section ridged waveguide transition. The five-electrode extraction system, shown in figure 2.2.6, consists of a plasma electrode made of stainless steel (at 80 kV), a puller electrode (at $40 - 42$ kV), two water-cooled grounded electrodes, and a negatively biased screening electrode inserted between the grounded electrodes in order to avoid secondary electrons due to residual gas ionization going up to the extraction area. Each electrode (except the plasma one) is divided into two parts: the first, close to the beam, is made of tantalum and the other is copper; this choice will increase the electrode power

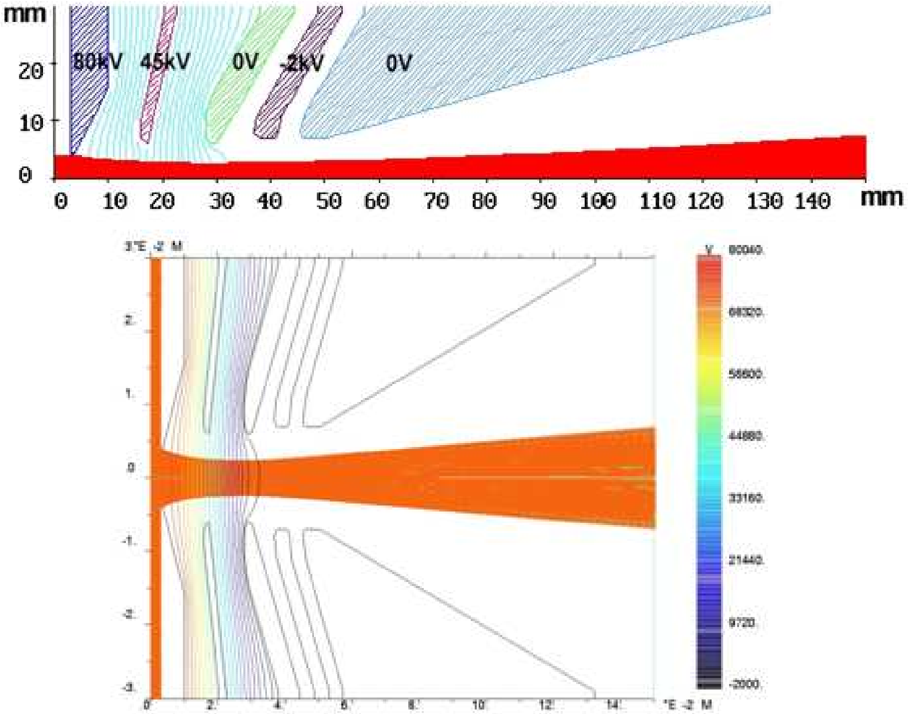

Figure 2.2.6: *Plot of the GUN trajectory of the TRIPS extraction system.*

dissipation and will permit the easy replacement of the first part without dismantling all the electrodes. The magnetic field is produced by two coils on line movable and independently energized. The position of the electron cyclotron resonance (ECR) zones determines the behavior of the source [29].

From these measurements the following conclusions can be drawn:

- the source is more sensible to variations in the extraction coil than to the injection one;
- the best performances are clearly obtained when the two ECR zones are located exactly on the BN disk at the two ends of the plasma chamber, as shown in figure 2.2.7. This magnetic profile has been used in different sources to optimize the their reliability and efficiency [44], [43], [29].

	Requirements	Results
Beam Energy	80 KeV	80 KeV
Total Current	35 mA	$\approx 60\ mA$ ($\phi_{extr} = 6\ mm$)
Proton Fraction	$> 70\%$	≈ 90 % (estimated)
Microwave power	$< 2\ kW$ at 2.45 GHz	0.3 - 1 kW at 2.45 GHz
Duty Factor	100% (dc)	100% (dc)
Emittance	$\leq 0.2\ \pi\ mm\ mrad$	$\sim 0.07\pi\ mm\ mrad$
Reliability	$\sim$ 100%	98% at 35mA (over 142 h)
Gas flow	$<$ 2 sccm	0.4 - 0.6 sccm

Table 2.2: *TRIPS requirements and Results [43].*

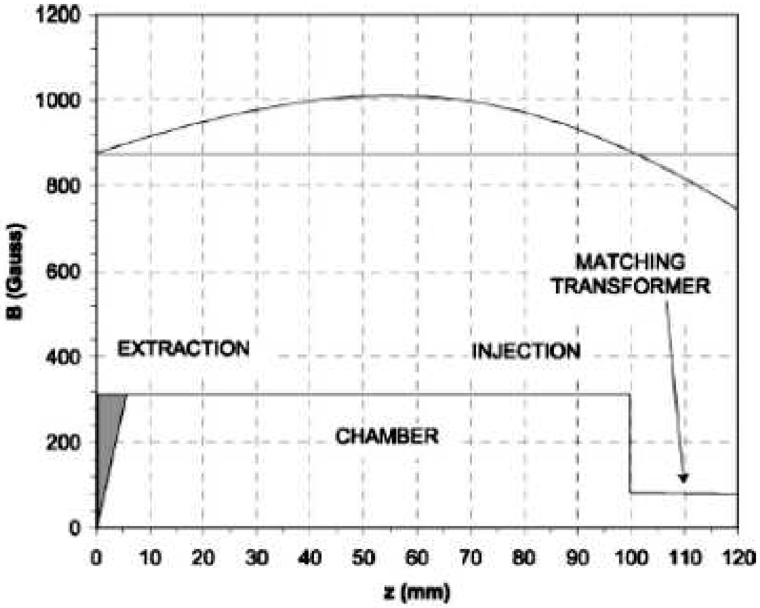

Figure 2.2.7: *The TRIPS optimum magnetic field [44].*

The emittance measurements confirmed that the typical source emittance at 40 mA is between 0.07 and 0.15 π mm $mrad$, in good agreement with the theoretical values predicted by the Krauss−Vogt formula [45]. Other measurements have been carried out at different current levels (between 30 and 50 mA) and the effects of rf power, puller voltage, solenoid currents and beam line pressure on the space charge compensation were explored. In such a type of plasma, only three species are present: H^+ (typically 90%), H_2^+ (8%) and H_3^+ (2% or less): the optimization of the proton fraction was made by tuning the injected gas amount and by increasing the rf power (table 2.2).

Chapter 3

Experimental equipments

The thesis is focused on the experimental study of the beam characteristic for two different sources. The Versatile Ion Source (VIS) operating at LNS-INFN in continuous mode and the SILHI (Source of Light Ions with High Intensities) ion source that operates at CEA Saclay in continuous and pulsed mode. A major goal of the optimization of the source performances was the increase of the produced beam brightness. A plasma reactor has been also used in order to improve the plasma parameters for different experimental setting; in particular the electromagnetic wave propagation and excitation mode in the plasma have been studied. The ion sources and the most important diagnostic devices used in the experiments will be described in the following sections.

3.1 Versatile ion source VIS

The TRIPS source overcomes all the requirements of the TRASCO project, but in order to simplify the source a proton source called PM-TRIPS was built in 2006 [44], once that the TRIPS source was installed at INFN-LNL, Legnaro and the test area was available. In particular in the PM-TRIPS source the movable coils have been replaced with permanent magnets, and the extraction geometry and extraction column has been simplified.

With these modifications we also avoid the high voltage platform and the

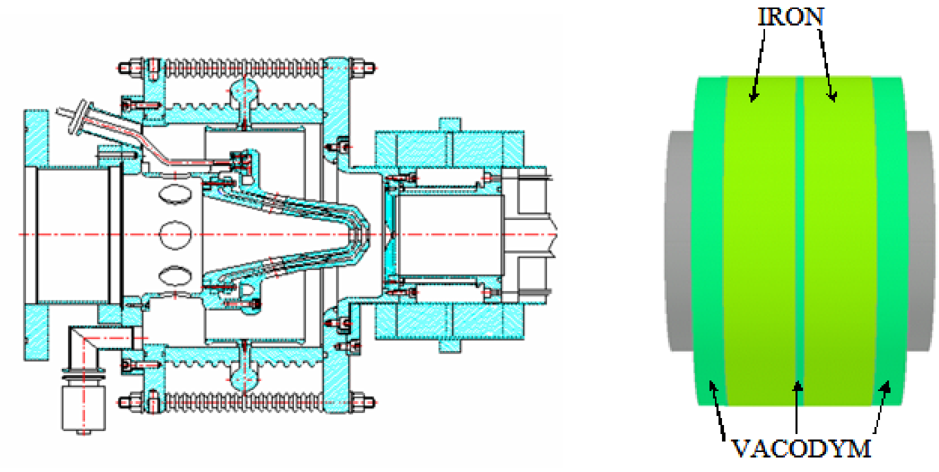

Figure 3.1.1: *PM-TRIPS Source and magnetic system*

insulating transformer, by insulating the gas pipe and the waveguide line. All these changes were expected to decrease the high voltage sparks and to increase the reliability. All the devices for the remote control were placed at ground potential, thus leaving only the plasma chamber and the permanent magnets at high voltage; the compact dimensions have also helped to get a better and easier maintenance.

The magnetic system, as it shown in figure 3.1.1, consist of a set of 3 Vacodym 745 HR permanent magnets; they are packaged together with two soft iron spacers and they are supported by a stainless steel tube.

During the first operations of this new source, some Penning discharges occurred, due to the stray magnetic field values in region near the extraction electrodes. In order to avoid this phenomenon the magnetic system has been completely redesigned by using the OPERA calculation suite and a new system magnetic has been used for the source VIS. The layout of the VIS source is reported in figure 3.1.2 [46].

Plasma chamber

The plasma chamber performs two roles: it couples microwave power to the plasma and it contains the plasma. The source body consists of a water-cooled copper plasma chamber (100 mm long and 90 mm diameter)

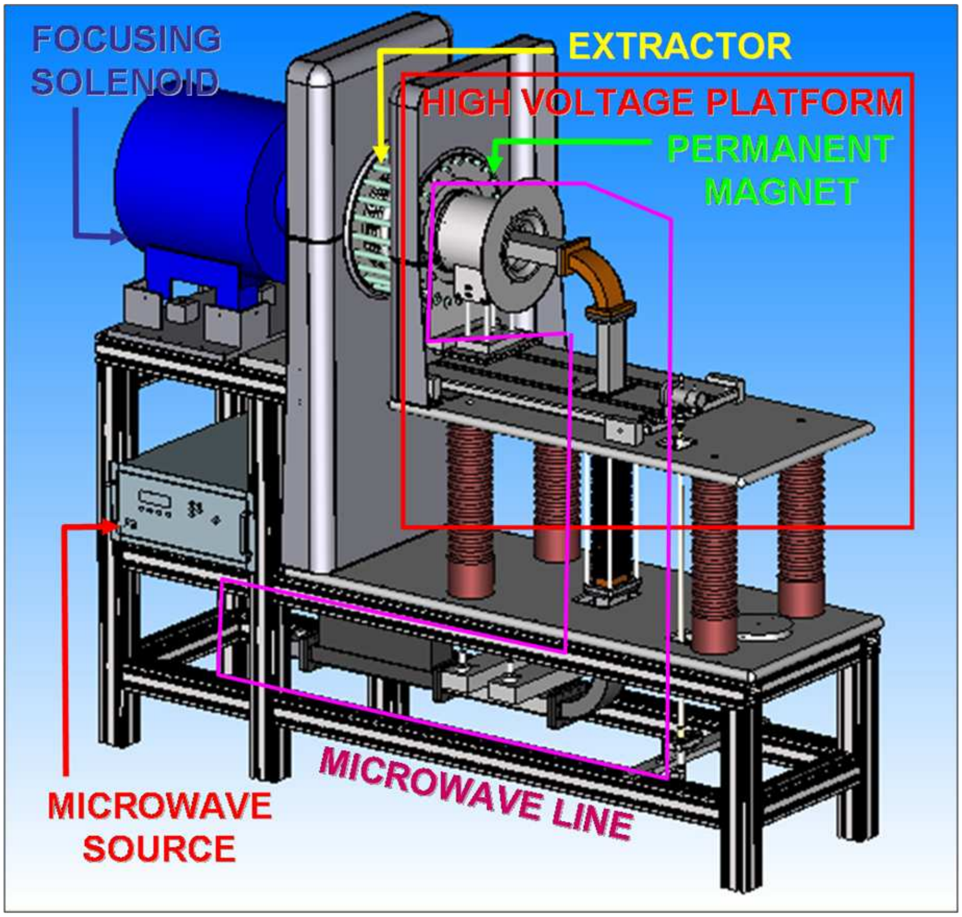

Figure 3.1.2: *A render view of the VIS source together with the focusing solenoid.*

surrounded by permanent magnets.

Formation of the plasma has been observed in this chamber for a microwave power greater than 400 W in presence of ECR field of 875 G and pressure of 10^{-4} mbar. The plasma consist ions, electron and neutrals. In case of hydrogen, the following reactions are dominant for the production of protons:

- $\mathrm{H}_2 + e \rightarrow 2H + e, \qquad H + e \rightarrow \mathrm{H}^+ + 2e.$
- $\mathrm{H}_2 + e \rightarrow \mathrm{H}_2^+ + e \qquad \mathrm{H}_2 + e \rightarrow \mathrm{H}^+ + H + e.$

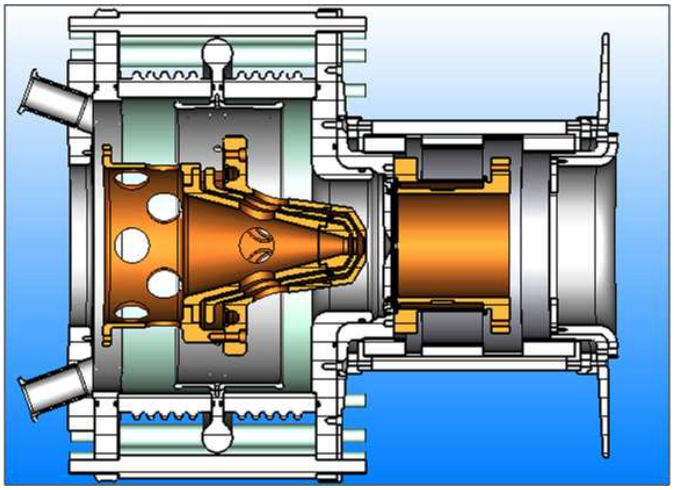

Figure 3.1.3:

- $H_2^+ + e \rightarrow 2H$, $\quad$ $H + e \rightarrow H^+ + 2e$
- $H_2^+ + H_2 \rightarrow H_3^+ + H$, $\quad$ $H_3^+ + e \rightarrow H^+ + H_2 + e$.

In order to enhance the proton fractions in these reactions, thick BN plate is located at the two extremities of the plasma chamber, one near the maximally flat matching transformer and the other near the extractor electrode. The nitride plate reduces the recombination processes for the formation of molecular ions. Moreover, due to high secondary electron emission coefficients of nitride plate, the electron densities in the ECR discharge is enhanced leading to increased dissociative ionization of the hydrogen.

The low operative pressure of $10^{-4} - 10^{-3}$ mbar in the plasma chamber, and of $10^{-5} - 10^{-6}$ mbar in extractor system is obtained by means of rotative and turbo-molecular pumps. The pressure difference in the plasma chamber and the extractor system was obtained because the plasma chamber was evacuated through the 8 mm hole in the plasma electrode.

Microwave System

The microwave line, in figure 3.1.4, is the result of an optimization study carried out with tools for high frequency structures simulation in order to reduce the microwave losses, simultaneously with an adequate matching

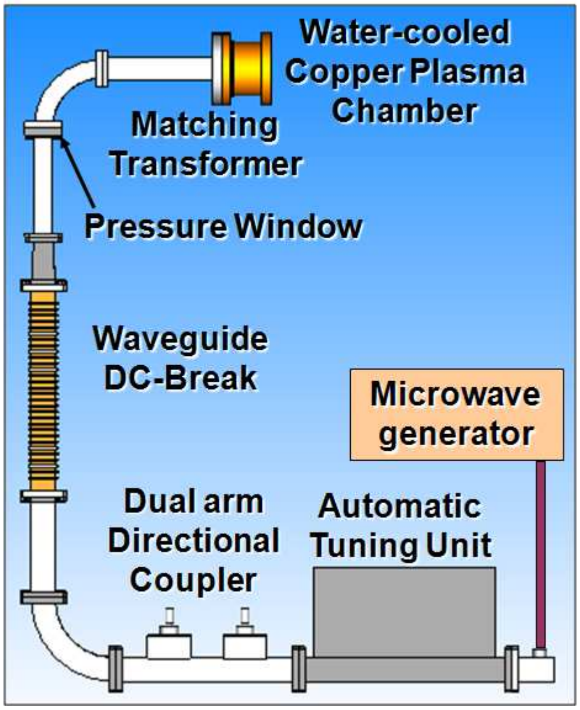

Figure 3.1.4: *VIS microwave line.*

of the waves to the plasma chamber. A plasma is generated by means of the microwaves provided by a 2.45 GHz Magnetron through a WR 340 (86.4 mm × 43.2 mm) waveguide excited in the TE_{10} dominant mode. An automatic tuning unit adjusts the modulus and phase of the incoming wave in order to match the plasma chamber impedance with and without the plasma, and a dual-arm directional coupler is used to measure the forward and the reflected power.

In TRIPS both the microwave line and the microwave generator are placed on the high voltage platform while in VIS the microwave generator is placed at ground potential. Then, in order to separate the high voltage region from the grounded one a waveguide DC-break has been designed and realized with the support of HFSS electromagnetic simulator [47], [48]. It is made of 31 aluminum disk of a WR 340 waveguide insulated one each other

(a) *A photo of* $WR340$ *DC-break.*

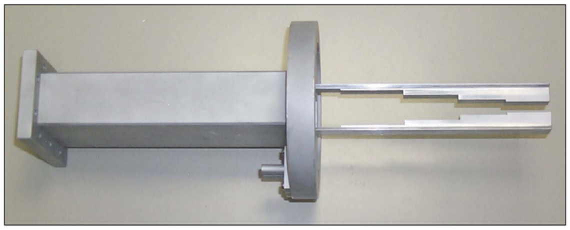

(b) *The matching transformer coupled to the plasma chamber.*

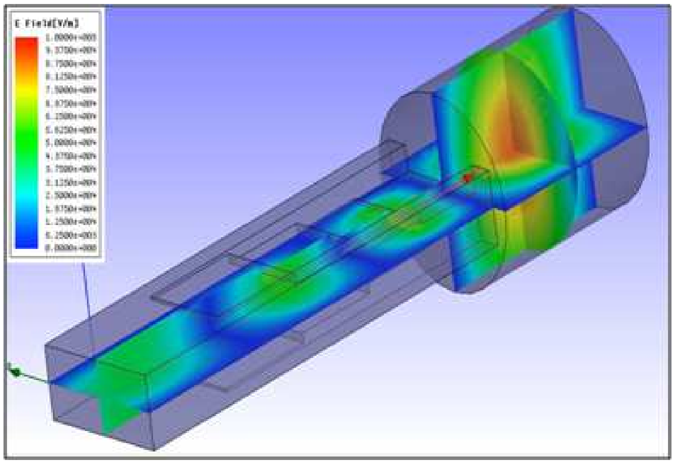

(c) *Electric field amplitude at* $2.45GHz$.

Figure 3.1.5: *Components of microwave line.*

by means of fiberglass disks 3.1.5 (a). The conductive parts will be fixed to voltages gradually decreasing from 80 kV to ground voltage, still keeping low the insertion loss.

The high pressure quartz window is placed before the WR 284 water-cooled copper bend in order to avoid any damage due to the back-streaming plasma electrons. Finally a maximally flat matching transformer has been inserted before the plasma chamber, shown in figure 3.1.5 (b) and (c), that is an optimized version of a similar device used in MIDAS and TRIPS ion source. It realizes an impedance matching with the plasma chamber and concentrates the electromagnetic field near the axis. The enhancement of the electromagnetic field in the plasma chamber cavity increases locally the plasma density and finally the ionization process [49].

Magnetic System

The magnetic system of the VIS source has been designed and realized with the aim to drastically reduce the stray field in this area and to avoid the Penning discharge, it is shown in figures 3.1.6. The magnets produce an almost flat field profile lower than 0.1 T, that exceeds the ECR resonance field (875 gauss), along the whole plasma chamber axis length. Due to the outer iron components the magnetic field quickly falls off in the extraction region. The stray field in the extraction area is significantly lower than for PM-TRIPS. Considering that the vacuum conductance is increased, the conditions for a Penning discharge are not reached. The resonant field for 2.45 GHz is present in two points along the plasma chamber axis. (As observed for similar ion sources these position, where two BN disks will be placed, are the optimum extremes of the chamber. This feature has been proven to be the best solution to increase the plasma electron density (figure 3.1.7).

Beam extraction electrode geometry

The ionic component of the plasma produced in plasma chamber is then extracted by means of four electrodes extraction system. The low energy beam transport line (LEBT) allows the beam analysis and it consists of a focusing solenoid, a four-sector diaphragm to measure the beam misalignments, a Direct-Current Current Transformer (DCCT), a 30° bending mag-

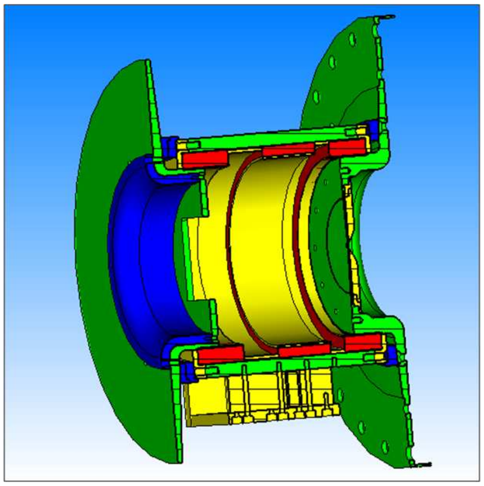

Figure 3.1.6: *View of the VIS magnetic system (in red the NdFeB magnets, in yellow the stainless steel components, in blue the aluminum ones and in green the ARMCO iron parts).*

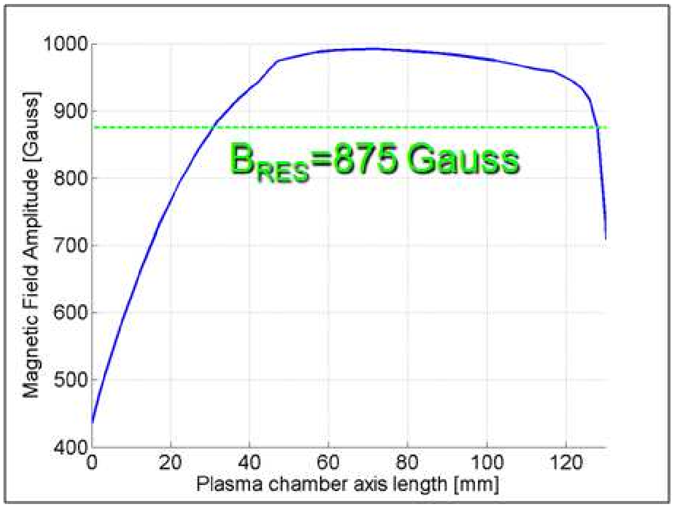

Figure 3.1.7: *Magnetic field values along the plasma chamber axis.*

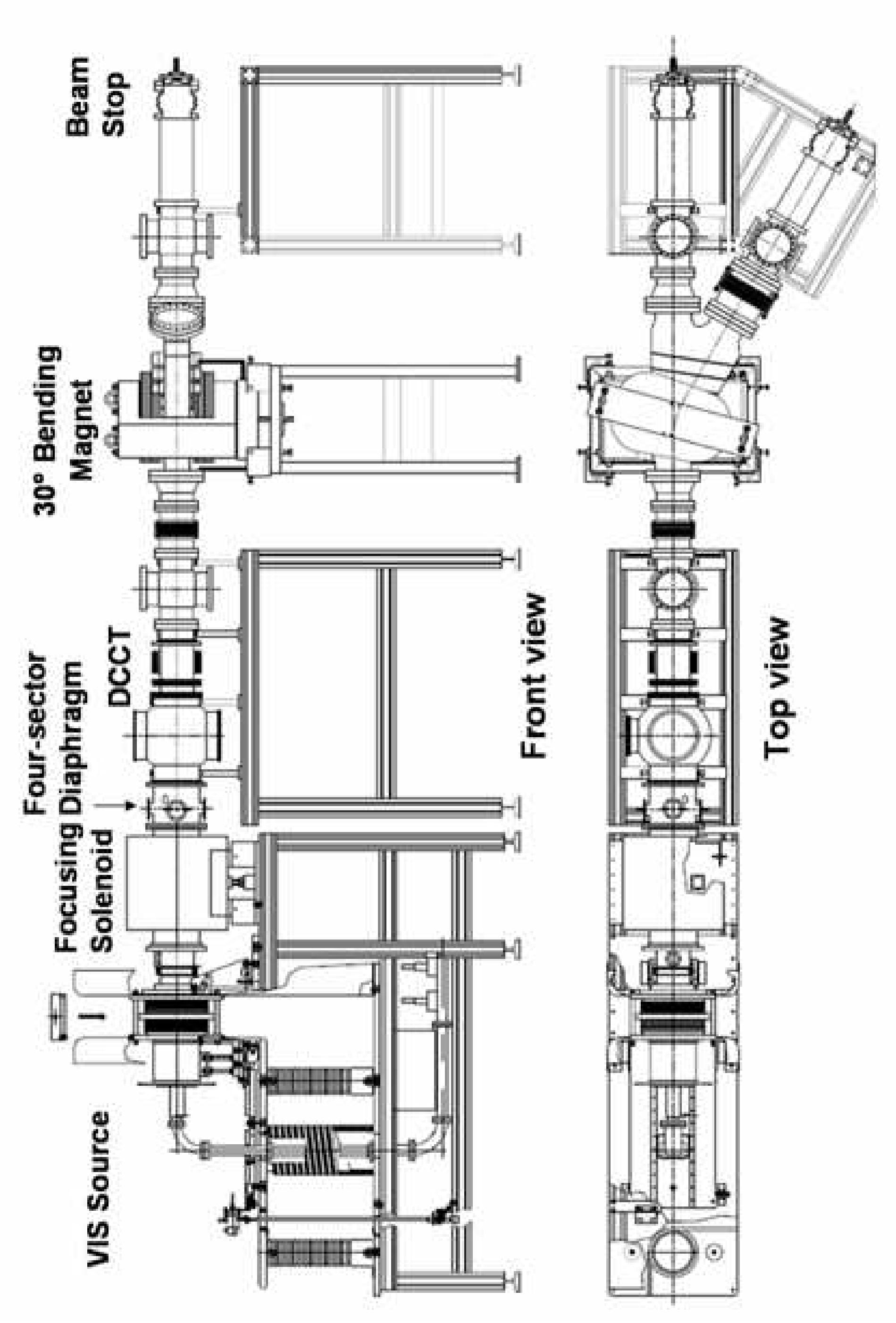

Figure 3.1.8: *A scheme of the VIS testbench.*

net and an insulated beam stop to measure the beam current, shown in figure 3.1.8.

The extraction system consists of a plasma electrode made of molybdenum at 65 kV voltage, two water cooled grounded electrodes and a 3.5 kV negatively biased screening electrode inserted between them, in order to avoid secondary electrons due to residual gas ionization, backstreaming to the extraction area. The VIS extraction has been optimized to work around 40 mA and a theoretical value of $0.1 - 0.2\,\pi\, mm\, mrad$ normalized emittance has been calculated, 11 cm far from the extraction electrode, i.e. fulfilling the requirement of high brightness.

The computer remote control permits to set the main source parameters and to monitor the source status and performance, ensuring the safe source operations. All the devices needed for the computer control will be at ground potential, this is the main advantage with respect to the TRIPS source, coming from the use of permanent magnets together with the insulation of the microwave line and of gas pipe. This choice permits to avoid any electronic device at high voltage making the high voltage platform and the insulation transformer not necessary and leaving only the source body at high voltage. The beam availability may be further increased and the damages to electronics because of high voltage sparks negligible.

3.1.1 The Technological Innovations of VIS

The VIS source presents many modifications respect to TRIPS source. The most important changes are about: the magnetic system, the extraction and the microwave system.

Magnetic system

> The magnetic field profile plays an important role not only for plasma heating, but also for the source reliability and for long term operations. On this purpose two independent resistive coils are preferable, but electronics at high voltage (power supplies and control) is needed. Anyway by using permanent magnets, like in case of the VIS source,

Table 3.1: *VIS performance.*

Parameters	
Extraction voltage	60 kV
Repeller voltage	~ -2 kV
Total current	> 35 mA
Proton current	> 30 mA
Proton fraction	$> 85\%$
Microwave power frequency	$0.5 - 1.5$ kW at 2.45 GHz
Axially magnetic field	$875 - 1000$ G
Duty cycle	100% dc
Beam emittance at RFQ entrance	$\leq 0.2\ \pi\ mm\ mrad$
Reliability	to be done

it is possible to produce ion beams with better stability and reliability in comparison with the solenoid coils system.

With these modifications it also has been wanted to avoid the high voltage platform and the insulating transformer, by insulating the gas pipe and the waveguide line. In this case all the devices for the remote control are at ground potential, thus leaving only the plasma chamber and the permanent magnets at high voltage; the compact dimensions help to get a better and easier maintenance.

Extraction system

For the topology of the beam extraction system at least a classical three electrode system is needed (accel-decel). The most performing sources have more sophisticated systems with 4 or 5 electrodes. The five electrodes topology allows the on-line optimization of the extracted beam, permitting to operate at different current ranges (10 to 100 mA) by optimizing the beam formation for each working condition.

The four electrode systems, in VIS, do not present such flexibility, but they are optimized in order to work around the operating value. Even in this case the use of a more flexible solution entails a major complexity in the controls.

Microwave system

In the VIS source there are two important technological innovations respect the TRIPS source [50], [51]: the DC-Break and the matching transformer.

Different topologies of DC-Break have been tested: the common single break structure which is worldwide the most used one and a more complex structure which call *multi-break* and that gives the possibility to operate safely at higher extraction voltages or at higher microwave power. In the first case a single gap must withstand the potential drop, while in the second case different metal sections separated by adequate insulators permit to divide the potential drop by a greater number of sections.

The DC-Break for the VIS source has been designed on the assumption that continuous operation at $\sim$ 60 kV is possible for the multi-break approach, with a potential drop for each section lower than 3 KV/mm to avoid discharge inside the waveguide. At first it has been thought to create structure composed by 30 disks of 2 mm thick Boron Nitride separated by 31 disks of 12 mm thick copper. Then the final DC-Break consists of 31 aluminum disks separated one from each other with fiberglass disks, with a 1.4 dB insertion loss at 2.45 GHz.

Both the TRIPS and VIS source have been used two different maximally flat matching transformer in order to optimize the coupling between the microwave generator and the plasma chamber and concentrating the electric field at chamber center. The characteristic port impedance Z_0 at the two input of the structure has been calculated in order to verify their matching properties. In particular at 2.45 GHz the TRIPS structure transform the 413.93 Ohm characteristic impedance into 145.4 Ohm, while the VIS transformer in 72.85 Ohm, thus improving the matching to the plasma.

3.2 Plasma Reactor

A plasma reactor was designed at INFN-LNS in order to dissociate complex molecules (in particular for environmental applications [52]). It practically works like a MDIS, with a plasma that is *weakly ionized* and strongly collisional because of low electron temperatures ($Te \sim 1 \div 15\ eV$) and high pressures ($0.1 \div 0.5\ mbar$). The plasma chamber (shown in figure 3.2.1) is a stainless steel cylinder 276 mm long, with a radius of 67.8 mm. A NdFeB permanent magnets system generates an off-resonance magnetic field along the plasma chamber axis (with a maximum of 0.1 T on axis). The magnetic system used for this device is the same that was used for PM-TRIPS and that was made available for other purposes since installation of VIS in the test area. The high electron-neutral collision frequency determines a high rate of molecules fragmentation, thus increasing the dissociation fractions. For safety reasons, the reactor efficiency has been tested by using non dangerous gas, in particular n-hexane (C_6H_{14}) and cyclehexane (C_6H_{12}) [53] but the final aim of the experiment, carried in $2006-7$, was the dissociation of dangerous complex molecules (e.g. *dioxin*).

The microwaves are generated by a Magnetron operating at 2.45 GHz with 300 W of maximum power; they are injected into the plasma chamber through a $WR284$ (72.136 mm width and 34.036 mm height) rectangular waveguide placed on the cavity axis that operates in the TE_{10} dominant mode like the other MDIS. A rotative pump is used for vacuum (working pressure was about 10^{-3} mbar are usually obtained). Several measurements have been carried out in order to determine the optimum operating conditions in terms of microwave power and gas pressure and n-hexane and cyclo-hexane have been successful dissociated [53]. The plasma reactor has been used as a testbench to investigate the standing wave formation inside the resonant cavity even in presence of plasma, which has been one of the most important achievement that have been recently obtained in the field.

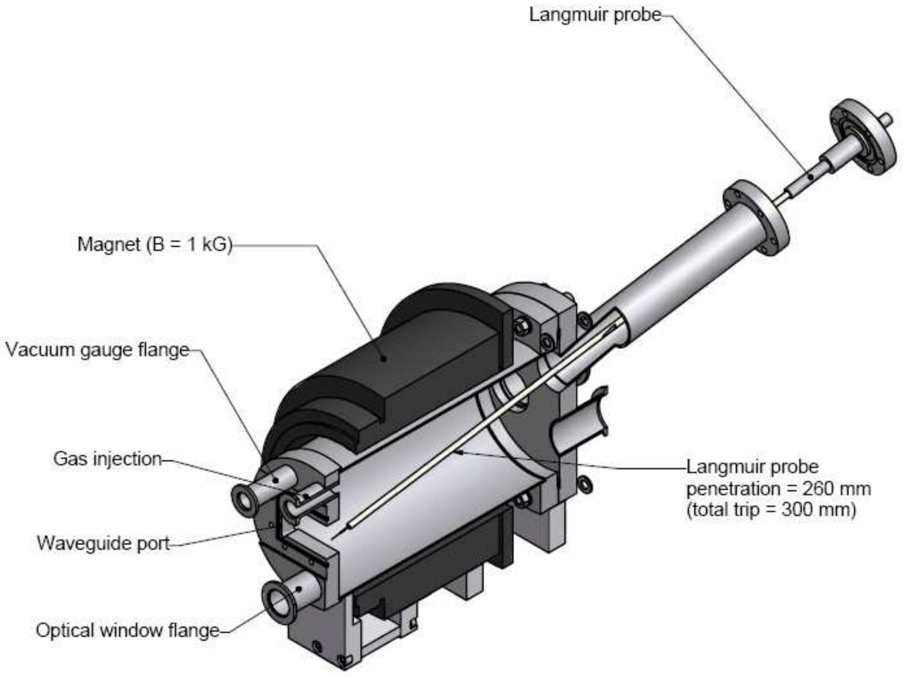

Figure 3.2.1: *Render view of the Plasma reactor source operating at LNS.*

Several measurements were performed by means of a vectorial network analyzer (NA) able to operate up to 50 GHz [54], in order to characterize the system including the plasma chamber (in vacuum) and the microwaves line in terms of S matrix with and without plasma.

The measurements of reflected and transmitted power have been performed by means of power meters connected to the waveguide directional coupler. The results of these measurements are reported in [55], [56] and they feature a complicated mechanism of wave plasma interaction which strongly depends on the back- ground pressure and on the RF power. A coaxial connector is also used; it permitted to determine the S_{11} parameter in presence of the plasma (a series of attenuator were used to reduce the output power) and to investigate the best condition of wave-plasma coupling thanks to a microwave probe that can be connected to it. For S_{11} parameter characterization the plasma was ignited through the waveguide and the NA was connected to the coaxial connector. By analyzing the S_{ij} parameters it may be possible to characterize the modes that exist inside the plasma chamber. In fact the frequencies for which the minimum values of the S_{11} occur, they represent the excited modes. Measurements of scattering parameters have been carried out in parallel with Langmuir Probe measurements of the plasma parameters, i.e. electron temperature and density, ion temperature and density. The whole set of data has permitted to improve the knowledge of MDIS plasma and it will be described in [56], [57] with more details.

3.3 High Intensity Light Ion Source - SILHI

The Saclay ion source, called SILHI (Source d'Ions Legers Haute Intens) [29] operates at 2.45 GHz and it uses two coil-generated axial magnetic field around B_{ECR} to generate and sustain the plasma (875 G). The source and its ancillaries are installed on a 100 kV high voltage platform and is routinely produces 95 keV beams. The 90 mm inner diameter plasma chamber is 100 mm long. Both ends are lined with 2 mm thick boron nitride (BN) disks. The molybdenum plasma electrode is designed with a single 8 mm diam aperture. The quartz rf window is located behind a water-cooled bend in order to be protected from backstreaming electrons. The rf power is produced by a 1.2 kW magnetron and is fed to the SILHI source via standard rectangular waveguides with a four stub automatic tuning system in between. A three section ridged waveguide transition is located between the plasma chamber and the bend to enhance the rf field. The magnetic field is now produced by only two coils over four available originally tuned and positioned independently. Coils and plasma chamber are located inside an iron magnetic shield (Figure 3.3.1). The five-electrode extraction system has been designed with the multiparticle code AXCEL6. An intermediate electrode located in the accelerating gap can be tuned to minimize the distortions in the phase-space distribution and to modify the beam focusing. An electrode at $\sim -2\ kV$ is inserted between two water-cooled grounded electrodes to avoid the acceleration of electrons produced by ionization of

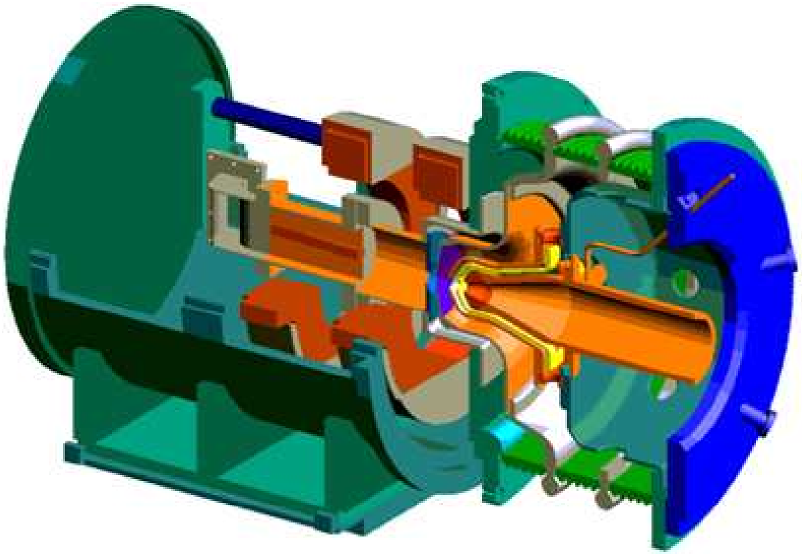

Figure 3.3.1: *Render view of the SILHI source operating at CEA-IRFU, Saclay.*

the residual gas in the LEBT. To avoid damages in the case of beam losses, the electrodes are made using an original assembly of copper and tantalum.

A single solenoid LEBT has been designed to characterize the extracted beam. The 0.22 T iron shielded solenoid (560 mm long, 250 mm inner diameter) is set at 1.05m after the plasma electrode to focus the beam in a diagnostic box. The ion source gas load is pumped by two 1000l/s turbomolecular pumps: the first one at the exit of the accelerator column and the second one on the emittance measurement unit (EMU) box. To allow an accurate matching to the RFQ a precise knowledge of the beam characteristics is required at the cavity entrance. Presently the beam position and size are obtained from charge coupled device (CCD) cameras. A Faraday cup, beam stopper, and toroids [Direct-Current Current Transformer (DCCT) and Alternating-Current Current Transformer (ACCT)] are used to measure the beam current and its high-frequency fluctuations. Insulated screens give information on beam losses and beam axis. The EMU uses the

---

[1] due to neutron production

Table 3.2: *SILHI H^+ and D^+ beam performance [58] .*

Parameters	Request	Status	Request	Status
Energy [keV]	95	95	95	100
IE voltage [kV]	55	56	...	50
I_{H^+},D_{H^+}[mA]	100	108	140	129
I_{tot} [mA]	110	130	155	135
H^+, D^+ fraction (%)	> 90	83	> 90	96
Plasma Φ [mm]	...	9	...	9
Density $[mA/cm^2]$	140	204	243	212
Duty Cycle (%)	100	100	100	0.2^1
$\epsilon_{rms.norm.}$ $[\tau\ mm\ mrad]$	0.2	0.15	0.2	...

classical *hole-profiler* techniques [59]. A 0.2 T-1 MV/m Wien filter is placed behind the 0.2 mm diam sampler to analyze the species ($\mathrm{H}_1^+/\mathrm{H}_2^+/\mathrm{H}_3^+$) and to measure the proton beam emittance.

The extracted beam parameters have been analyzed for many configurations of rf power, hydrogen mass flow and versus the tuning of the source magnetic field. By moving a single ECR zone from the rf input towards the plasma electrode (the second one being in the extraction zone), the extracted current decreases rapidly by a factor of 2 and the proton fraction goes down from 88% to 72%. The best performances are clearly obtained when the two ECR zones are located at the ends of the plasma chamber, on the BN disk at the rf input and close to the plasma electrode. The source efficiency increases to 0.145 mA/W in the double ECR mode instead of 0.105 mA/W in the single ECR mode [29].

Table 3.2 gives the requirements and the present performance of the source. More than 100 mA cw can be routinely accelerated at the nominal energy. For a 80 mA cw proton beam produced in the single ECR zone mode the losses are very low in the extraction system and in the LEBT

($\sim$ 20 μA on the intermediate electrode and $\sim$ 1 mA on the grounded electrodes with a limited temperature increase of 5 $°C$). The nominal r - r' rms normalized emittance is lower than $0.3\,\pi\,mm\,mrad$ and the proton fraction is better than 85%. The fraction for other species is below 12% for H_2^+ and 3% for H_3^+. A strong improvements of the emittance was obtained by injecting a buffer gas (H_2, N_2, Ar, or Kr) into the LEBT [43]. Emittance reduction as important as a factor of 3 have been observed while the proton fraction is unchanged and the beam losses induced by recombination are below 5% for the heaviest gases.The space-charge compensation factor has been measured at several points along the LEBT in order to understand the emittance reduction phenomena [60]. SILHI works also in pulsed mode since the tuning of a high intensity cw linac may be done with pulsed beams. SILHI current produced beam intensity higher than 120 mA in pulsed mode (as shown in Tab. 3.2) [61].

Indeed SILHI produced deuteron beam and to minimize neutron production the source has worked in pulsed mode ($2ms/s$) by modulating the 2.45 GHz magnetron power. A 135 mA total current beam has been easily extracted at 100 kV with the puller (intermediate electrode) biased at 50 kV. To obtain such a current 900 W were injected in the source. The D^+ fraction reached more than 95%, other extracted ions being D_2^+. Due to the non-adapted extraction system, a good transport line transmission was not expected; 100 mA were collected on the beam stopper located at 3.75 m downstream the plasma electrode, leading to a 75% LEBT transmission. More recently a similar source such a source has been developed to produce low current (5 mA) D^+ cw beam for the Spiral 2 project.In this case, the magnetic configuration is provided by permanent magnet rings and shielding has been installed to avoid Penning discharge in the extraction system, as in the VIS source. The extraction diameter aperture has been reduced to 3 mm and currents from several hundred of microamperes to 7 mA have been analyzed.

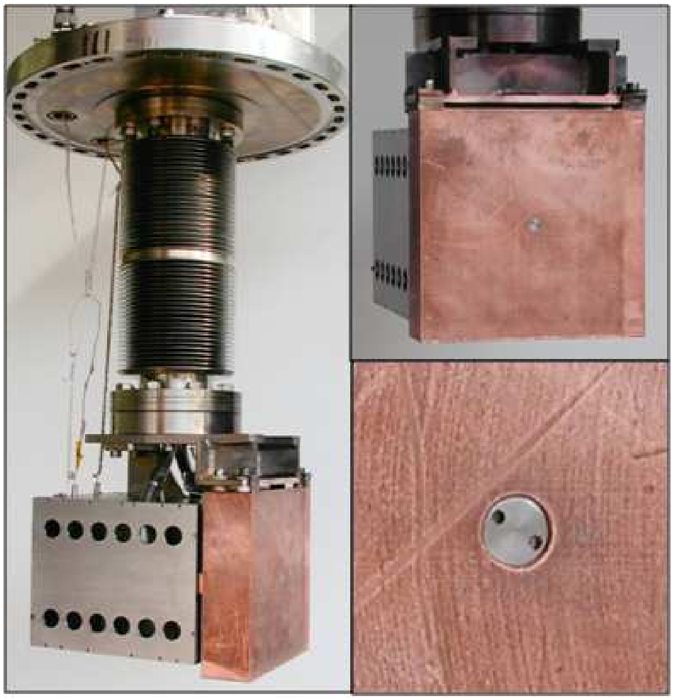

Figure 3.4.1: *Emittance Measurement Unit*

3.4 Beam and plasma diagnostics

3.4.1 Emittance Measurement Unit

The transverse emittance is a fundamental parameters for charged particle beams, because it allows the prediction of focus size and beam losses in a following accelerator. The measurement of these parameters help in optimizing the accelerators and improve the quality of the beams they produce. Positive ion sources normally output a mixture of ions with different masses and charge states. Because all ions have the same energy per charge, they follow the same trajectories in electric fields. However, different ion temperatures and stray magnetic fields often introduce slight variations in the emittance of the different species and charge states. Emittances measured at the output of the ion source or in electrical LEBTs are a linear combination of the emittance of the different species. What is interesting, however, it is only the emittance of the specie that will be selected in an analyzing magnet or be accelerated by the RFQ.

The emittance measurements for VIS and SILHI have been carried out by means of an emittance measurement unit (EMU) provided by the CEA-IRFU/Saclay SILHI group and shown in figure 3.4.1.

EMU is made of three part [62]:

1. the 0.2-*mm*-diameter tantalum sampler located in a water cooled copper block;
2. the permanent magnet Wien filter with adjustable electric field;
3. the wire for beamlet intensity measurements.

Our beam, as we have wrote in the section 3, consists of H^+, H_2^+ and eventually H_3^+, ions species with same charge state but different mass. The EMU allows the separate beam species analysis and the emittance measurements for the desired particle beam. The beamlet passing trough the front list experiences the electric and magnetic forces. The two forces are arranged in parallel or antiparallel direction upon positive or negative voltage on the deflection plates. Only a part of the beamlet, as the deflection electric field reaches a corresponding value, can pass through the beamlet slit and is collet by means a wire behind it [63]. So for example in figure 3.4.2 the distribution of the proton beam has been obtained: the three ions species, having a different masses, are subjected to different magnetic field strengths consequently they reached the beam slit for distinct electric field values.

Figure 3.4.2 represent the ratio of intensity of three ion species, obtained when the sample is on axis with respect to beam line. The device use a stepper motor, so the sample is moved long a beam diameter. Figure 3.4.3 is a graphical users interface of the EMU software (LabVIEW), it is divided in two sectors. We have used the first sector at the top to move vertically the sample. Instead with the second sector we have set, from time to time, the start and the stop of emittance measurements: it can choose the range of space interval and the step between each measurements as low as 1 mm. For each position by varying the electric field from 0 to 10 kV/cm, it is possible

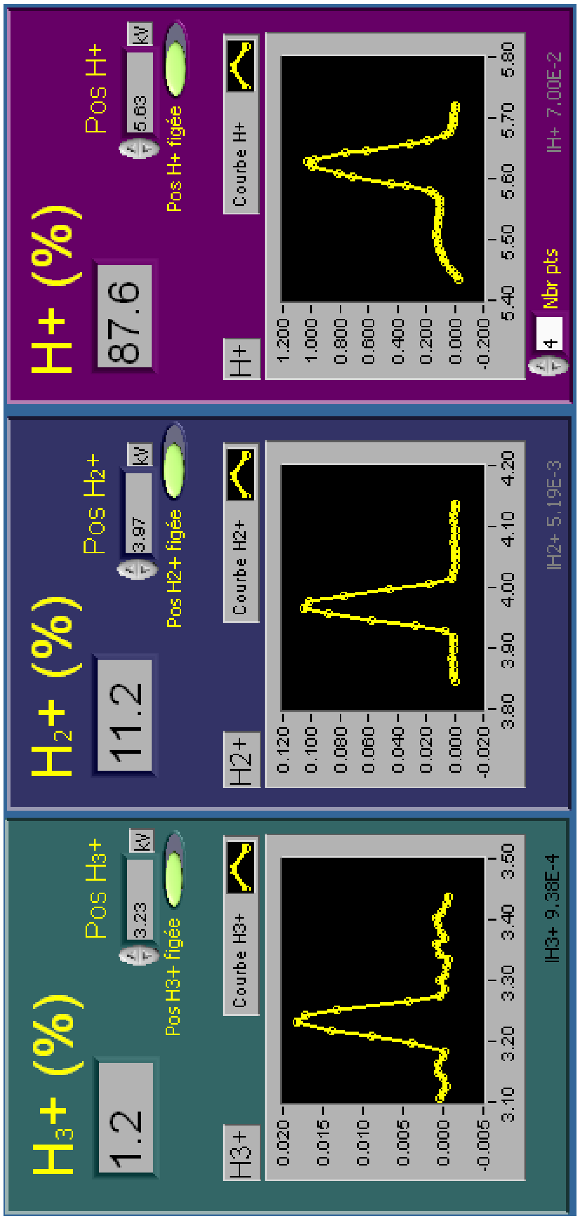

H+ (%) 87.6

Pos H+ 5.63 kV

Pos H+ figée

Nbr pts 4

IH+ 7.00E-2

H$_2$+ (%) 11.2

Pos H2+ 3.97 kV

Pos H2+ figée

IH2+ 5.19E-3

H$_3$+ (%) 1.2

Pos H3+ 3.23 kV

Pos H3+ figée

IH3+ 9.38E-4

Figure 3.4.2: *Distribution of the proton beam measured by means the EMU.*

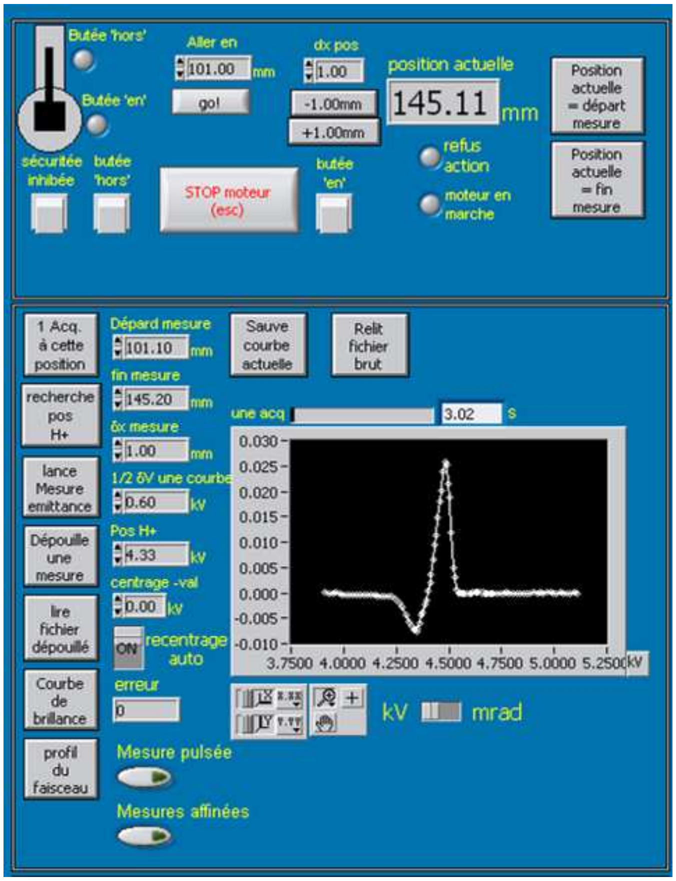

Aller en 101.00 mm

dx pos 1.00

position actuelle 145.11 mm

Dépard mesure 101.10 mm

fin mesure 145.20 mm

δx mesure 1.00 mm

1/2 δV une courbe 0.60 kV

Pos H+ 4.33 kV

centrage -val 0.00 kV

recentrage auto ON

une acq 3.02 s

erreur 0

Figure 3.4.3: *The graphical user interface of the EMU software, it permits to set and to monitor the measurement status.*

to determine the H^+ current peak, that we can see in graph of figure 3.4.3.

In order to make the emittance measurements, the beamlet divergence is deducted from the width of the current peak collected on the wire. The sampler position and the average potential value for the peak give the global divergence of the considered beamlet. Automatic procedures allow emittance measurements within a few minutes.

We remind that the LEBT of the VIS source has been designed in order to characterize the beam and the EMU was not originally considered, but with minor changes it was possible to adapt the EMU. The emittance mea-

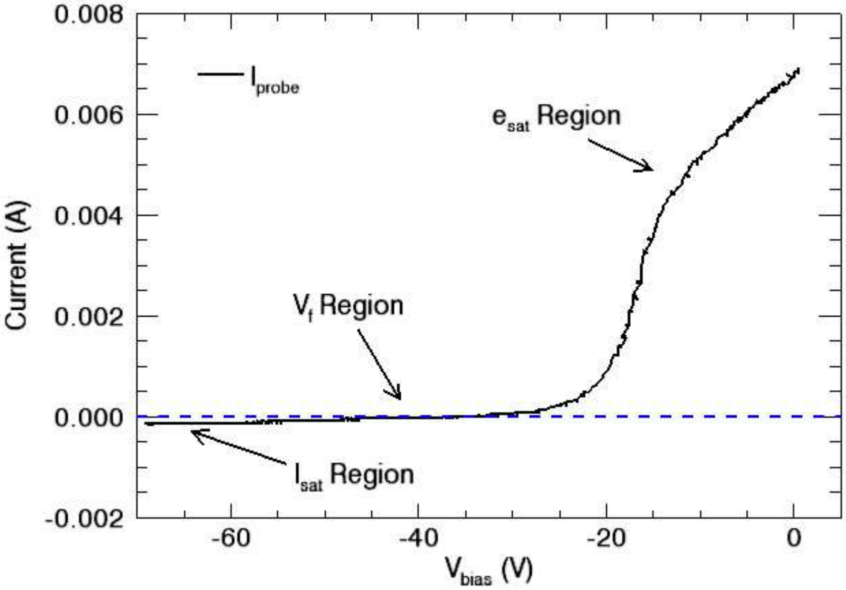

Figure 3.4.4: *Langmuir probe current-voltage characteristic show how the probe current varie with probe potential.*

surements have been carried out at different permanent magnets position; for fixed permanent position we have changed the puller voltage, microwave power and pressure. For different experimental set-ups the beam current varies from 30 to 45 mA with $\phi_{extr} = 8$mm.

3.4.2 Langmuir Probe

Plasma characterization has been obtained by means an electrical probe, which allows to measure local plasma parameters.

The working principle is, that a conducting wire of area A, whose potential V (measured respect to the plasma potential) can be controlled is immersed in a plasma [64]. When sweeping its potential and measuring the current I through the probe a characteristic current is obtained, which can be interpreted as follows:

Region 1: when the voltage is made very negative all electrons are repelled and the ion current is:

$$I_i = 0.6 n_i A e \sqrt{\frac{kT_e}{m_i}} \tag{3.4.1}$$

with m$_i$ the ion mass. If V made less negative a few higher energetic electrons are collected and this electron current is calling the *floating potential* V_f. On the probe electrode the positive ions are collected, so that around the probe a positive spatial charge is created. This charge screens the probe, which is on negative potential, from the other particles in the plasma. Just through this spatial charge layer, which surrounds the probe, the application of Langmuir probe for plasma diagnostic become possible because the disturbance created is small and localized.

Region 2: when the voltage keeps increasing the current varies according to

$$I = I_e exp\left(\frac{eV}{kT_e}\right) - I_i \tag{3.4.2}$$

where $V = V_s - Vp$, plasma potential minus probe potential. I$_e$ is the electron current in the retarding region:

$$I_e = neA\sqrt{\frac{kT_e}{2\pi m_e}} \tag{3.4.3}$$

As negative potential of the probe electrons decreases beside ions electrons also arrive at the probe. First very high energetic, laser also low energetic electrons penetrate the potential. Thus the probe does not measure the pure ion current, but the difference between the electron and ion current.

The electron temperature T$_e$ is determined from the slope of $\ln\left(I + I_i/I_e\right)$ versus V near the floating potential.

Region 3: As the probe potential is further increased the current drawn eventually saturates because all the electrons are collected.

When a magnetic field is present, we need to know how this magnetic field will affect the result. The principal effect of the field is to cause the electrons and ions to move no longer in straight lines but to orbit around the magnetic field lines in helical orbit with transverse radius [65]:

$$r = \frac{mv}{eB} \tag{3.4.4}$$

This radius is called the Larmor radius. The importance of the magnetic field effect is obviously determined by the ratio of r to the typical dimension r$_p$, probe radius. Clearly the electron Larmor radius is smaller than the ion radius by the factor $\sqrt{(m_e/m_i)}$. As a result, the electros are more strongly affected that the ions.

Depending on Larmor radius, the current collection phenomena of probe in plasma with magnetic field can be divided into three categories [66]:

1. r$_p \ll$ r: weak B-field;
2. r¡r$_p$: moderate B-field;
3. r$\ll$ r$_p$: strong B-field.

In the plasma reactor we are in the first case: both ion and electron currents are identical to the zero-magnetic field case [2].

The Langmuir probe used for our experiment consist of a 4 mm length of tungsten wire, with a diameter of 150 μm (the metallic wire protrudes from a cylindrical alumina sheath). A motor allows to move the probe inside the plasma chamber with an accuracy of 0.5 mm. The Langmuir probe is located so that it can penetrate inside the cavity for its entire length, forming an angle of 14° with respect to the chamber axis. An HIDEN commercial Langmuir probe has been used [67], and it was *user friendly* especially for the data analysis: the HIDEN software allows to easily determine the main plasma parameters by fitting the characteristic I-V curve.

---

[2] In plasma reactor we have estimated a Larmor radius of about $1.2 \cdot 10^{-6}$ m for 0.1 T magnetic field. This value is lower than probe radius $75 \cdot 10^{-6}$ m

Chapter 4

Experimental measurements

The experiments have been carried out mainly at the Laboratori Nazionali del Sud (LNS), exception for some measurements that were performed at CEA/Saclay (DSM/IRFU). Two ion sources have been used: the VIS source at LNS and the SILHI source at CEA/Saclay.

In the previous section we have described many proton sources: for each one the most important parameters are the maximum beam current and the intensity of the single ion species. So the total beam current and the proton beam was studied as a function of the microwave power, gas pressure, the extracted voltage and the permanent magnets position.

In order to make a meaningful analysis, further measurements are required, regarding the quality of the ion beam. In fact the emittance measurements have been made to characterize horizontal beam profile in the LEBT.

The measurements in pulsed microwave operations (pulse mode) were performed by means of the SILHI source (described in the section 3.3). By using the pulsed microwave operation we have generated a plasma with parameters that cannot be achieved in the cw mode. It was found that the total beam currents were increased in the pulse mode operations with respect the case of the cw mode.

We have characterized the beam current by changing the pulse duration and frequency with a duty cycle lower than 0.15. For each configuration we have determined the rms normalized emittance.

4.1 VIS characterization in continuous mode

In plasma sources the output current depends linearly on the electron density:

$$I \propto \frac{n_e}{\tau_i} \tag{4.1.1}$$

τ_i denotes the lifetime of the ion to be obtain. It corresponds to the confinement time a for source which makes use of plasma trapping.

As said in chapter 3 the MDIS ion sources produce ion beams with low charges state (1^+ and 2^+). So in our sources the increment of ion beams is connected mainly to the enhancement of electron density. High electron densities assure a more efficient ionization of the low-pressure plasma. Typical plasma parameters of proton sources operating in the off-resonance mode are: $\mathrm{T}_e = 20$ eV (above the hydrogen ionization threshold), $\mathrm{n}_e = 1{-}1.5 \cdot 10^{17}$ cm^{-3} that is above the $\mathrm{n}_{cutoff} = 7.5 \cdot 10^{16}$ cm^{-3}

4.1.1 Beam current measurements

In the experiment here reported, a background pressure of $10^{-6} \div 10^{-7}$ mbar was maintained for several hours, before the data acquisition. The working gas was then introduced in the plasma chamber by means of an unidirectional valve (UDV) in such a way that in the extractor region the pressure was kept in range of $1 - 2 \cdot 10^{-5}$ mbar.

The plasma discharge electrodes power supplies were energized by computer control; the figure 4.1.1 shows a graphical users interface of the VIS software (LabVIEW), used to switch on the FUG 100 kV and the FUG 3 kV and apply the voltage. Then the microwave generator was switched on and we created the plasma in the chamber. The reflected power was minimized using an automatic tuning unit (ATU in the panel show in figure 4.1.1). Once the plasma discharge was established, the current flowing in the solenoid coil was adjusted to obtain the desired magnetic field configuration which focus the proton beam.

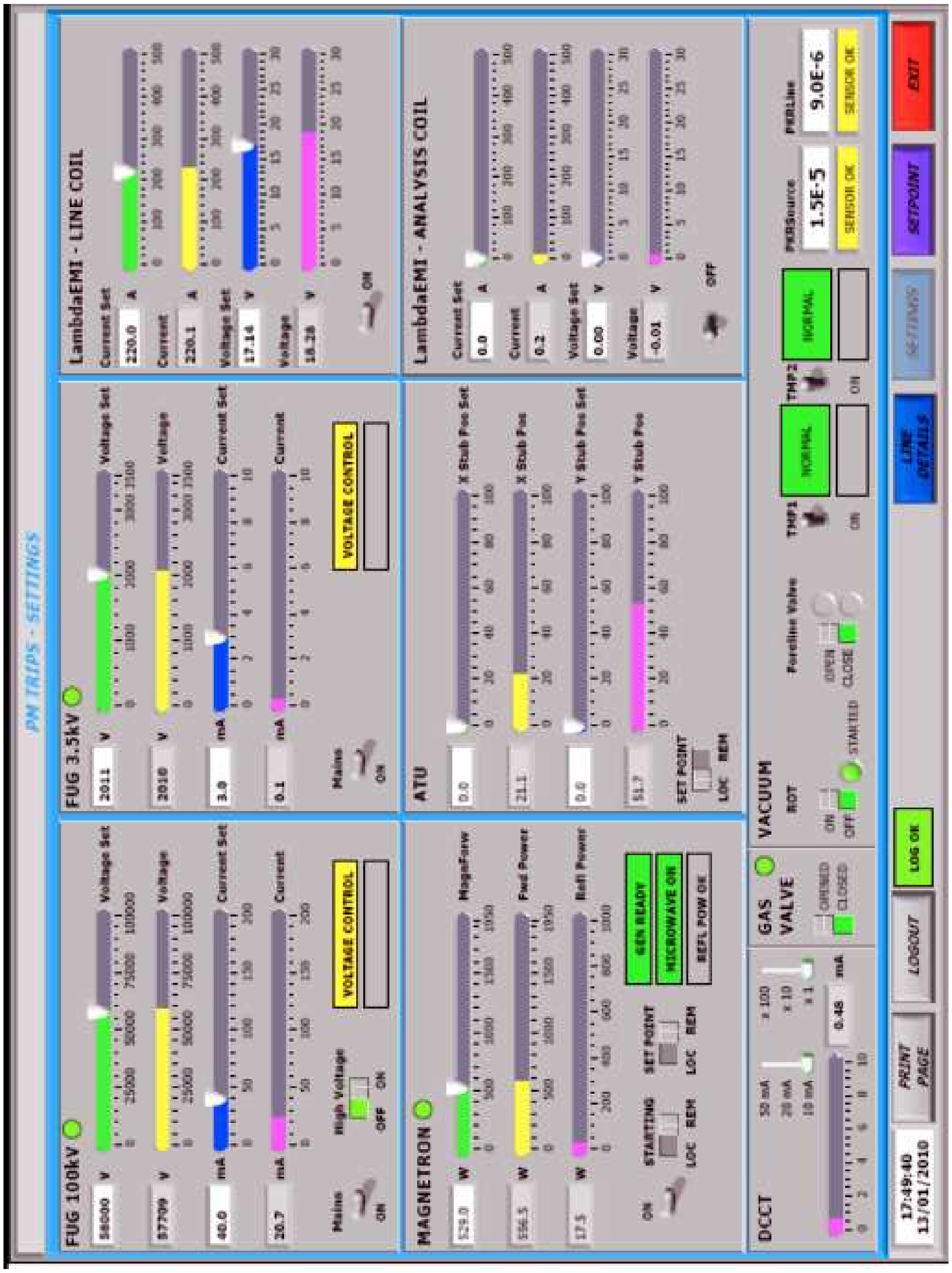
PM TRIPS - SETTINGS

FUG 100kV
Voltage Set 38000 V
Voltage 37709 V
Current Set 40.0 mA
Current 20.7 mA
Mains ON
High Voltage OFF ON

FUG 3.5kV
Voltage Set 2011 V
Voltage 2010 V
Current Set 3.0 mA
Current 0.1 mA
Mains ON

LambdaEMI - LINE COIL
Current Set 220.0 A
Current 220.1 A
Voltage Set 17.14 V
Voltage 18.28 V

MAGNETRON
MagnForw 529.0 W
Fwd Power 556.5 W
Refl Power 17.5 W

ATU
X Stub Pos Set 0.0
X Stub Pos 21.1
Y Stub Pos Set 0.0
Y Stub Pos 51.7

LambdaEMI - ANALYSIS COIL
Current Set 0.0 A
Current 0.2 A
Voltage Set 0.00 V
Voltage -0.01 V

DCCT
0.48 mA

VACUUM
TMP1 NORMAL
TMP2 NORMAL
PKRSource 1.5E-5 SENSOR OK
PKRLine 9.0E-6 SENSOR OK

17:49:40
13/01/2010

Figure 4.1.1: *The computer control permits to set the main source parameters and to monitor the source status.*

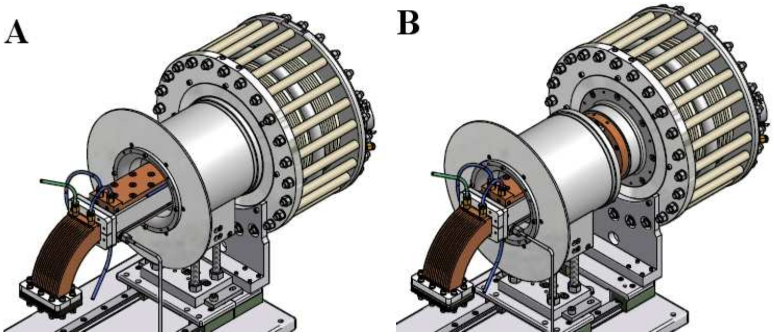

Figure 4.1.2: ***A)*** *Initial position of permanent magnets.* ***B)*** *Position of permanent magnets after they have been moved towards the copper bend (The displacement of the magnetic system is not on scale).*

The magnets system was moved with steps of 2 mm, from 0 to 12 mm, according to the sketch in figure 4.1.2: **A**) represent the permanent magnets position that we have called *at home*, and **B**) represent the shifted position towards the microwave line. For fixed permanent magnet positions we have changed the extracted voltage, microwave power and pressure. The operative pressure has been changed from $1.8 \cdot 10^{-5}$ to $2.5 \cdot 10^{-5}$ mbar, the extracted voltage from 50 to 65 kV.

The maximum current density that can be expected for any charged particle species accelerated by an electric field is obtained under space-charge limited conditions and follow the Child-Langmuir law (in this case the ions are assumed to have zero initial energy in the longitudinal direction) [16] :

$$I = \frac{4}{9}\epsilon_0 \left(\frac{2Q}{M}\right)^{1/2} \frac{\pi a^2}{d^2} V^{3/2} \tag{4.1.2}$$

where I is the total beam current that can be obtained from a cylindrical-symmetric extraction system, d is the extraction gap, Q is the charge, M is the mass of the ion, and a is the radius of the extraction aperture.

In figure 4.1.3 the total ion current and the current calculated by means the Child-Langmuir law is plotted versus the acceleration voltage. The Child-Langmuir law estimates the upper limit of ion current extractable through the ion charge space, so the extracted current is lower than those

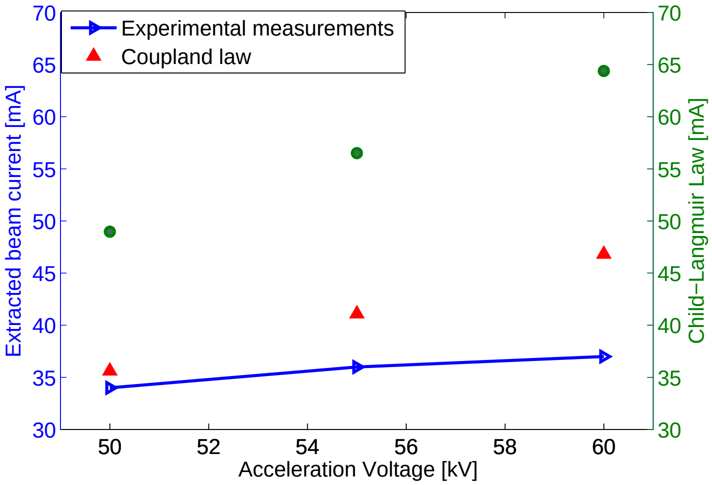

Figure 4.1.3: *Extracted current, Child-Langmuir current and Coupland current vs acceleration voltage for different pressure values, at* 700 *W and* 2 *mm shifted permanent magnets.*

estimated, and it increases with the increase of extracted voltage. In our case the ion current enhances more or less linearly with the increase of extracted voltage, the total increase is less than 10%, instead the Child-Langmuir law predicts an increment higher than 31%.

Here the data are better fitted by the equation 4.1.3 used by Coupland et al. [68, 69]: the idea is that the transported beam current emitted from an aperture into a finite acceptance angle does not infinitely rise with increasing area, but it rather saturates according to:

$$I = P^{*}V^{3/2}\frac{S^{2}}{1+tS^{2}} \tag{4.1.3}$$

where S is the aspect ratio $S = a/d$, P^{*} is the low-S perveance, t is the aberration parameter. In our measurement we have chosen the t value to obtain the best fit to the experimental data.

The increase of the ionic current with the extraction voltage can also be seen in Figure 4.1.4, where we have plotted the ion beam as a function of microwaves power when the magnetic system has been shifted of 4 mm.

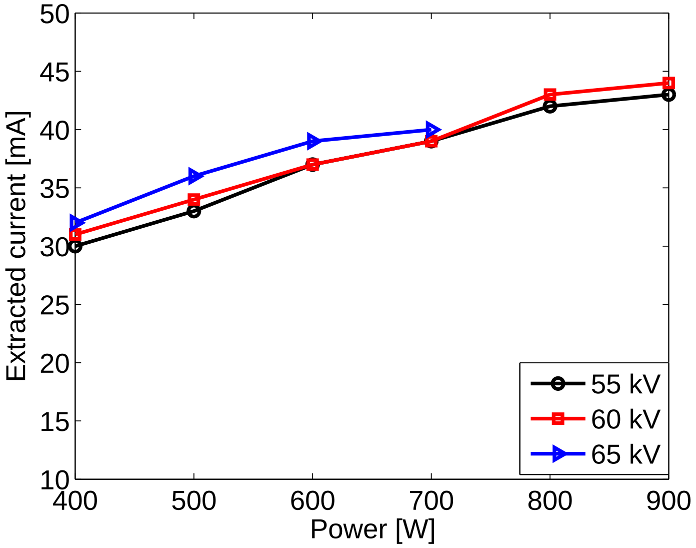

Figure 4.1.4: *Extracted current vs microwave power for different extracted voltage, at* $2.3 \cdot 10^{-5}$ *mbar and* 4 *mm shifted permanent magnets.*

For each microwave power values we have obtained more intense beams in correspondence to the maximum extracted potential value. But at 65 kV the source didn't allow to operate at powers higher than 700 W because discharges occurred (outgassing of the puller electrode was the probable reason).

The trend, reported in figure 4.1.4, shows an increase of the ionization rate (which in turn increase the plasma density) with the microwave power[1] [70]. In addition this phenomenon is related to the collisional mean free path. As the density increases, the mean free path decreases. Therefore the most of their electrons loose energy in high density plasmas because of collisions [33]. This makes worse the ionization rate, because many electrons become too cool. Additional quantities of RF power are then needed to restore a high plasma density regime. This is confirmed by measurements at different

---

[1] In some cases the total current tends to saturate at high microwave power values. This indicate that the further increase of the extracted beam should be obtained by increasing the extraction hole diameter than by enhancing the microwave power.

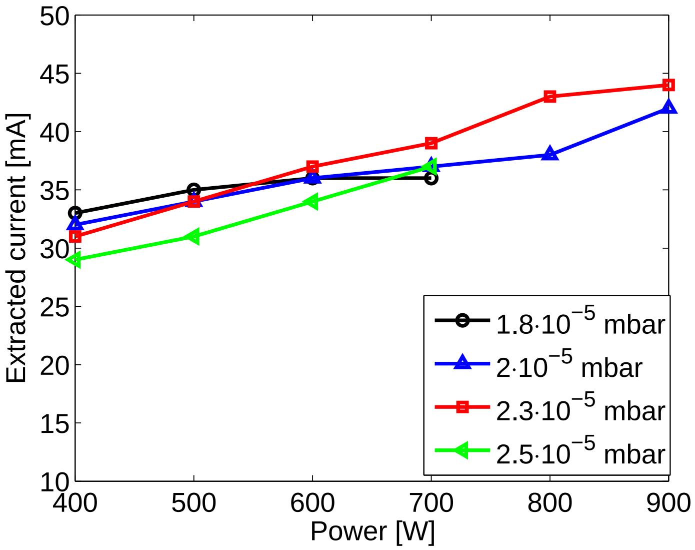

Figure 4.1.5: *Extracted current vs* 60 *kV, for different pressure and* 4 *mm shifted permanent magnets position.*

background pressures, as shown in figure 4.1.5.

The extracted ion current is plotted as a function of microwave power at various gas pressures. Going from $1.8 \cdot 10^{-5}$ to $2.5 \cdot 10^{-5}$ mbar, the beam current was found to increase linearly with gas pressure only for three pressure values. At $2.5 \cdot 10^{-5}$ mbar the total extracted current was much lower than the other measurements, because the energy of the electrons was not sufficient to ionize the gas molecules. At high pressure the improvement of the total beam current needs that the microwave power be increased.

The current intensity as a function of the permanent magnets position is shown in figures 4.1.6. The microwave power has been changed from 600 to 1200 W and the pressure was set at two values: $2 \cdot 10^{-5}$ mbar in figure 4.1.6 **A)** and $2.3 \cdot 10^{-5}$ mbar in figure 4.1.6 **B)**. In figure **A)** a maximum current of $\sim$ 49 mA has been obtained, operating at 1200 W, when the permanent magnets has been shifted of 2 mm. In **B)** currents values like 50 mA have been extracted for magnetic system shifted of 4 mm. Although for the two hydrogen flow rates there are the same magnetic configurations, it can be

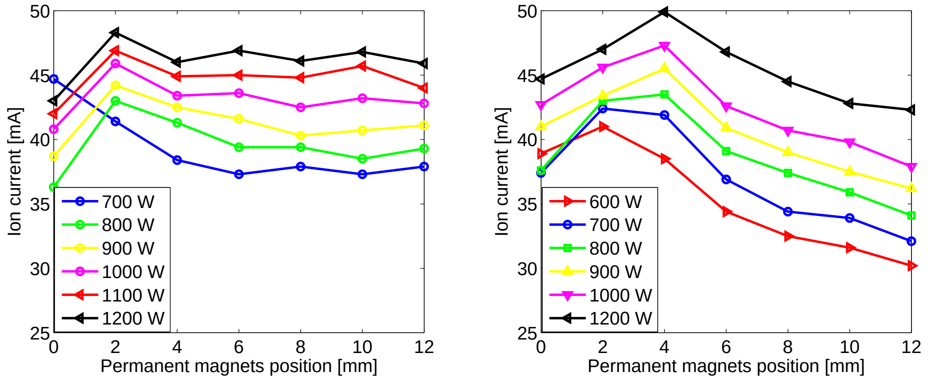

Figure 4.1.6: *Extracted current vs permanent magnet position for different microwave power: at A)* $2 \cdot 10^{-5}$ *mbar, B)* $2.3 \cdot 10^{-5}$ *mbar.*

observed that by operating at $2 \cdot 10^{-5}$ mbar the total beam current is only weakly affected by the different permanent magnets position, unless for the first position for which the lower intensity value was measured. By operating at $2.3 \cdot 10^{-5}$ mbar, in correspondence of the first permanent magnet position, low total current have been obtained, but these values are not the lowest. The beam current decreases when the magnet system is approaching at the microwave window, so the minimum total current values have been observed for permanent magnets position close to 12 mm.

4.1.2 Proton fraction measurements

A desirable property of such sources is that the proton fraction of the extracted beam be as high as possible. This allow to directly inject the proton beam into an accelerating structure (otherwise magnetic selection would be needed). The magnetic separation leads to an emittance growth and possible losses of beam brightness that is a situation undesirable for high current cw superconducting accelerators.

Previous works [71], [72] showed that by adding trace amounts of water[2] to the plasma chamber, the proton fraction increases from $\sim 75\%$ up to 95%. The addition of H_2O to the source appears to have additional bene-

---

[2] 1% of H_2O to the source

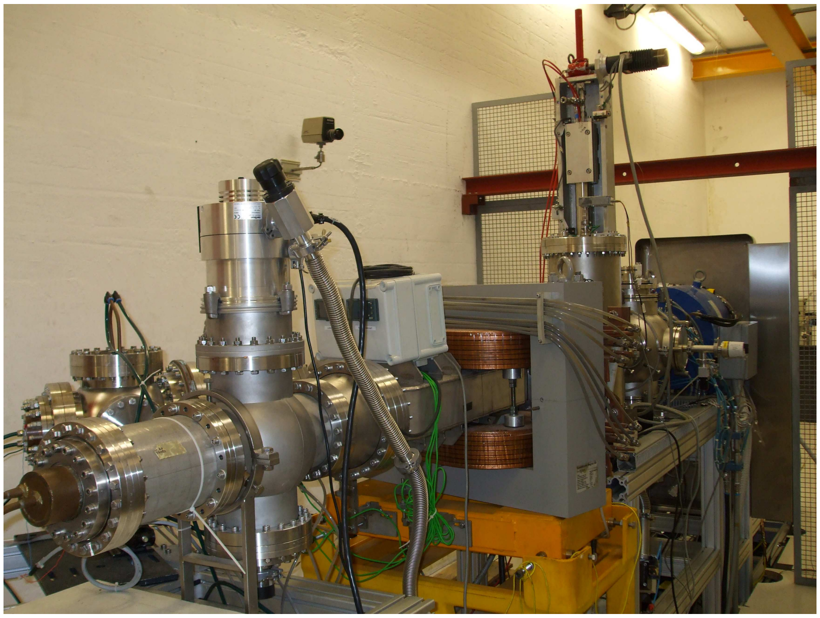

Figure 4.1.7: *A view of LEBT.*

fits, significantly stabilizing the plasma and producing a less noisy beam. In other works, Sherman and al. [28] have found that by operating the source with oxygen plasma for approximately $60 - 90$ min before the usual operations with hydrogen, a similar proton enhancement factor similar the water catalysis has been observed. The proton fraction enhancement may be related to the removal of injector contaminants and/or plasma chamber wall modification leading to a wall chemistry more favorable to a high atomic hydrogen concentration and hence a higher-proton fraction source.

In a previous work, Gammino et al. [73] have found that the proton fraction is increased when a thick Al_2O_3 tube is embedded in the plasma chamber. In our measurements only two BN disk have been used to increase the electron density.

The EMU, described in the section 3.4.1, can make proton fraction measurement as we have reported in figure 3.4.2.

This measurement has been obtained when the device was aligned with respect to the LEBT axis, and so it calculated only the fraction of the beamlet that pass through the slit. It is more interesting to measure the species fraction of the whole beam at the end of the beam line. On this purpose the analyzing magnet was used, the H^+ and H_2^+ species were swept into two Faraday cups sequentially, by adjusting the analyzing magnet. The analyzing magnet is the 30° Bending Magnets shown in figure 3.1.8: by setting its current we can choose which ionic species will reach the Faraday cup, located at 30° with respect to LEBT axis. For each species measurement, the electromagnetic solenoid current was adjusted to get the maximum beam current. In fact, the experiments showed that the focus strength of the three species is approximately proportional to the square root of the specie's mass, which means that the three species have almost the same path through the LEBT in that case.

Measurements reported here were made without the addition of H_2O, at 60 kV of extracted voltage, and the proton fraction has been calculated by means this equation:

$$H^+\% = \frac{H^+}{H^+ + H_2^+}, \qquad\qquad H_2^+\% = \frac{H_2^+}{H^+ + H_2^+} \tag{4.1.4}$$

We did not measured the fraction of H_3^+ molecular species because its amount was negligible, therefore our measurements are related only to the two ionic components H^+ and H_2^+.

Figure 4.1.8 shows the proton and H_2^+ fraction of a beam extracted from the source operating at 500 W microwave power and at different hydrogen mass flow. Under these conditions the proton fraction of the total beam is higher than 70% and increases with the pressure. Indeed the proton fraction should decrease with increasing the pressure, as it has been measured in other works [28, 26]: as the gas pressure increases, the electron temperature decreases and the recombination processes begin to play the main role. It did not occur in our source because we should further enhance the hydrogen mass flow so that the recombination processes could become the prevailing effects. In figure 4.1.8 the total current trend is also reported: the ion beam increases with increasing the hydrogen flow too, as the proton fraction. We did not work at higher pressures because high pressure values generated some sparks in the source.

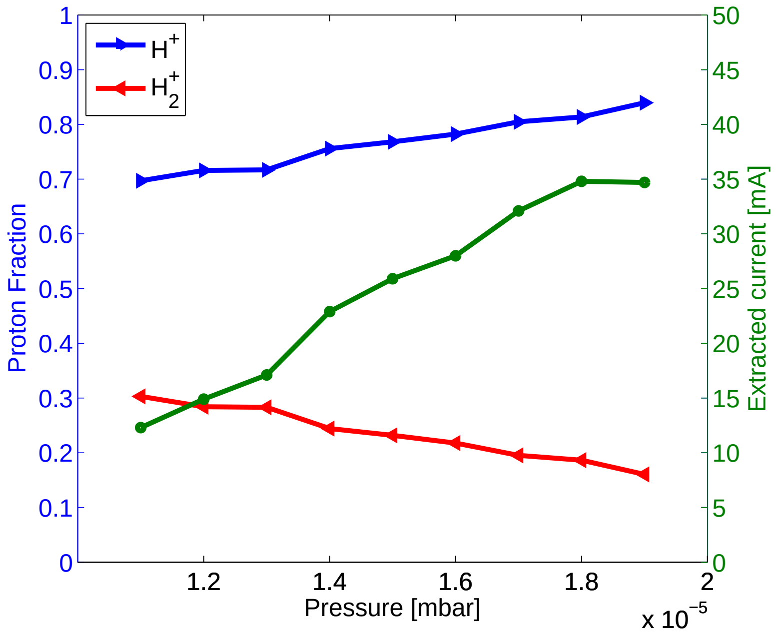

Figure 4.1.8: *Species fraction and extracted current vs hydrogen flow.*

The proton fraction, moreover, was measured under different microwave powers. In the figure 4.1.9 there are the species fraction and the total current as function of microwave powers at $1.9 \cdot 10^{-5}$ mbar. The beam current increases when enhancing the microwave powers, conversely the proton fraction saturates at medium high power levels.

This trends can be understood if we consider the important physical process occurring in a hydrogen plasma [74]:

The reactions that can occur in our source, listed in table 4.1, are:

1) H_2 Dissociative excitation: $H_2 + e \rightarrow H_2^* + e \rightarrow H + H + e$.

2) H_2 Ionization: $H_2 + e \rightarrow H_2^+ + 2e$.

3) H_2 Dissociative ionization $H_2 + e \rightarrow H_2^* + e \rightarrow H^+ + H + 2e$.

4) H_2 Dissociative ionization $H_2 + e \rightarrow H^+ + H + e$.

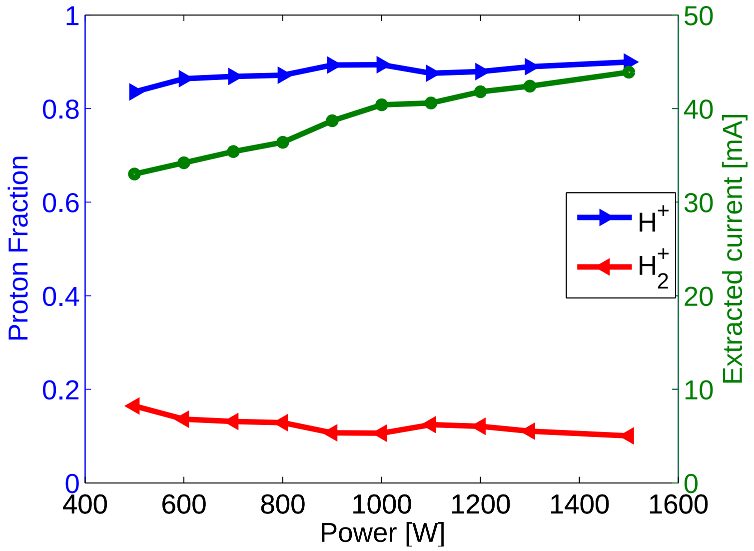

Figure 4.1.9: *Species fraction and extracted current vs microwave power.*

5) H_2^+ Dissociative excitation $H_2^+ + e \rightarrow H^+ + H^+ + 3e$.

6) H Ionization $H + e \rightarrow H^+ + 2e$.

7) H^* Ionization $H^* + e \rightarrow H^+ + 2e$.

where numbers designate the reaction, E_{th} is the threshold energy of the reaction, and E_{max} is the energy at the maximum cross section, σ_{max}. The dependence of the cross section on the electron energy for some important processes are listed in figure 4.1.10.

From figure 4.1.10 and the table 4.1: proton are mainly generated by the multiple collision processes **1)**, that we have introduced in the section 3.1 [3]. The single collision processes of **2)** and **4)** for hydrogen molecules mainly generate H_2^+ ions .

A high proton content is mainly generated by the two-step process **1)**, following by the reaction **6)**. This is because $T_e \sim 5 - 20$ eV in our source, the reaction rate coefficient **1)** for generating atomic hydrogen is larger than

---

[3] In the section 3.1 the process $H + e \rightarrow H^+ + 2e$ follows the reaction **1)**.

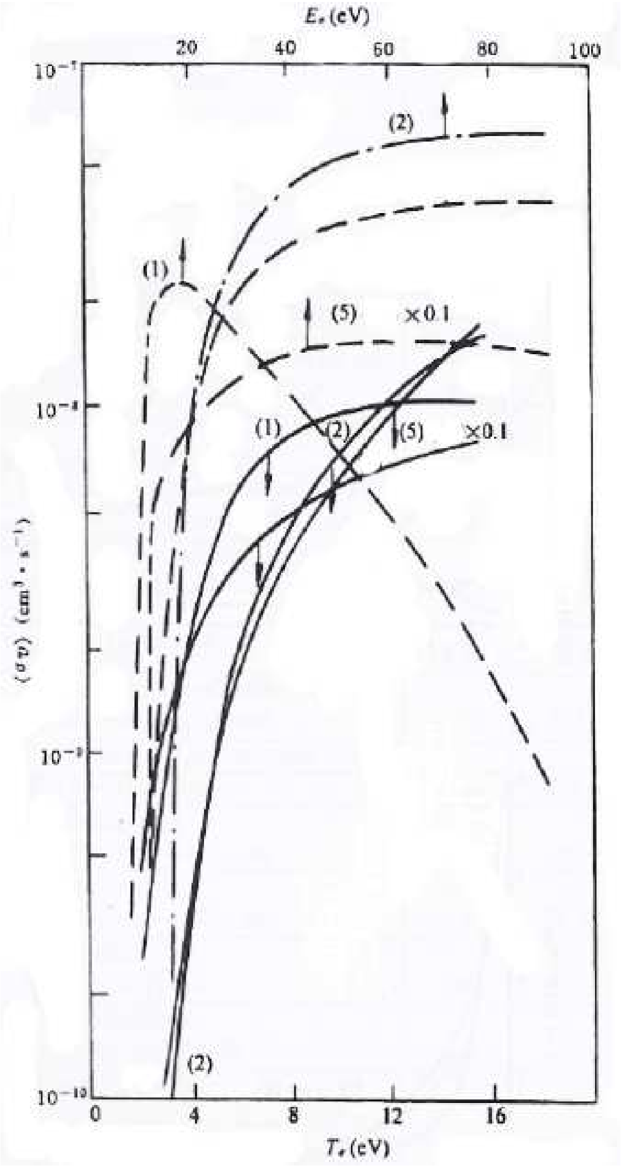

Figure 4.1.10: *Some important rate coefficient for ionization in a hydrogen discharge [74]. The solide line are* $< \sigma v >$ *average over a Maxwellian distribution for thermal electrons, and the dotted line are* σv *for monoenergetic electrons. The numbers in brackets are the corresponding reactions from the table 4.1.*

Table 4.1: *Various physical processes and their characteristic values for molecular hydrogen [74].*

	E_{th} (eV)	σ_{max} (10^{-16} cm^2)	E_{max} (eV)
1)	9.2	0.9	17
2)	15.6	0.98	70
3)	18	0.058	100
4)	46	0.005	120
5)	12.1	4.3	~ 24
6)	13.6	0.7	64
7)	3.3	9.4	13

2) for generating H_2^+ ions, as seen in figure 4.1.10, this results in a very high content of atomic hydrogen in the plasma chamber. When we applied higher microwave power values for a fixed hydrogen mass flow, the electrons gained larger amount of energy and consequently their temperature was increased. For higher electrons temperature, the cross section enhances slightly for the reaction **2)**, so we can observe in figures 4.1.9 that the proton fraction remains steady or decreases.

Figure 4.1.11 shows the trend of proton fraction as function of microwave power for two different permanent magnets configurations (the magnet system has been shifted of 4 and 6 mm respectively): in both configurations the proton fraction is higher than 80%. The change of magnetic field profile did not improve on proton fraction.

Finally we wanted to verify whether injecting of Argon in the LEBT, the species fraction would have improved. In fact for emittance measurements the neutralization of the space charge of positive ion beams, reached by electrons coming from ion-atom ionizing collisions in the background gas, can reduce the beam divergence. The proton fraction as a function of microwave power for different Argon mass flow is represented in figure 4.1.12. At a fixed chamber pressure ($1.3 \cdot 10^{-5}$ mbar) the Argon mass flow in the beam line has

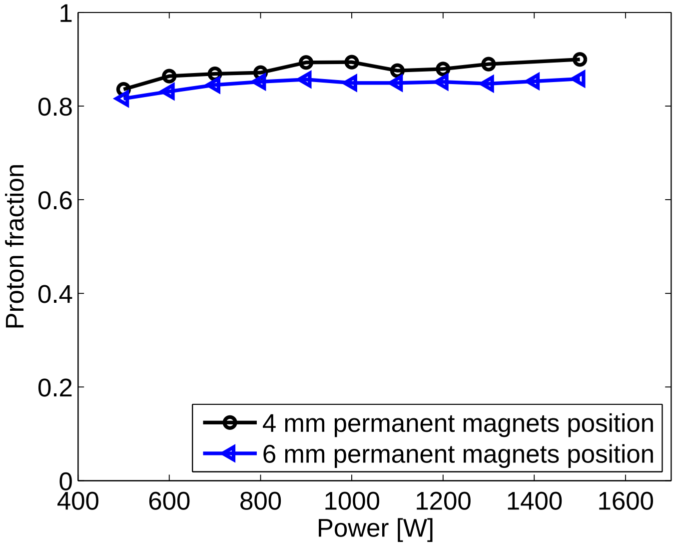

Figure 4.1.11: *Proton fraction vs microwave power for different permanent magnets position.*

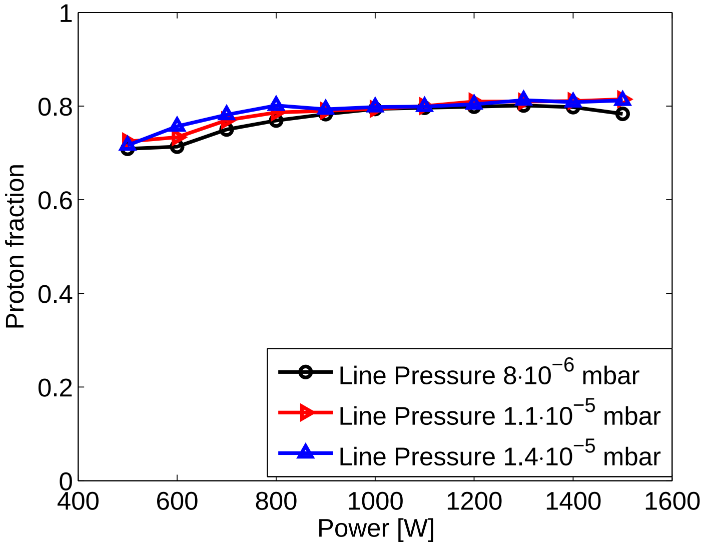

Figure 4.1.12: *Proton fraction vs microwave power for injection of Argon in the beam line.*

been changed twice ($1.1 \cdot 10^{-5}$ and $1.4 \cdot 10^{-5}$ mbar) and the species fraction measurements have been compared with those effected without Argon (Line pressure $8 \cdot 10^{-6}$ mbar). From figure 4.1.12 we can see that the proton fraction remains unchanged when Argon gas is injected in the LEBT: there was a slight fluctuation in correspondence of low microwave powers and for higher microwave powers the trend of proton fraction is similar for the three pressures.

In conclusion we have seen that the hydrogen mass flow and microwave powers influenced the different species by affecting the electron temperature: in fact the change of the electron temperature inside the plasma modifies Maxwellian distribution for thermal electrons that is correlated to rate coefficients for ionization processes. For example the single collision process will dominate at high T_e, resulting in a high H_2^+ content. Furthermore, the H^+ production can be increased if loss rate of the ions is reduced: the hydrogen atoms partially recombine at the wall chamber, so it very important to choose the material of the plasma chamber that reduces the hydrogen atom recombination coefficient of the wall material[4].

In our source we have measured high proton fraction values up than 80% for different hydrogen mass flow and microwave powers.

4.1.3 Emittance measurements

A complete characterization of the beam has been obtained by means of the emittance measurements unit, described in thesection 3.4.1, and shown in figure 4.1.13. The emittance measurements, as for total current and proton fraction, have been carried out at different permanent magnets positions. Fixing the permanent position, additional measurements were done by changing the puller voltage, the microwave power and the hydrogen mass flow. For different experimental set-ups the beam current varied from 30 to 45 mA for $\phi_{extr} = 8$ mm.

In addition for each configuration we have set every parameter like

---

[4] Quartz has a much smaller hydrogen atom recombination coefficient than copper. In the previous work [73] Al_2O_3 wall coatings have been used to increase the proton fraction.

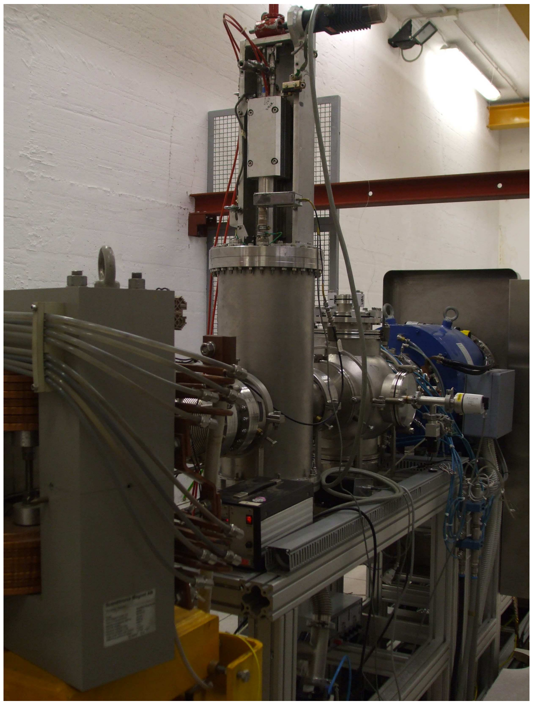

Figure 4.1.13: *A view of the LEBT and the emittance measurement unit (EMU) .*

Dépard mesure and fin mesure, shown in figure 3.4.3, to choose when the device began to make emittance measurements, with respect to the size of proton beam. The LabVIEW front panel was able to display and save the emittance picture, one of them is reported in figure 4.1.14. Below the emittance picture there are the values of ϵ_{rms}, ϵ_{nrms} and Twiss parameters (α, β and γ).

In the study of beam divergence it is needed to take in account the space charge forces in the beam, as these forces usually govern the beam's behavior. **Space charge** (SC) is the simplest and the most fundamental of the collective effects whose impact generally is proportional to the beam intensity. The charge and current of the beam creates self-generated fields and image fields which alter its dynamic behavior and influence the single-particle motion as well as coherent oscillations of the beam as a whole [75].

If we consider many charged particles travelling in an travelling beam

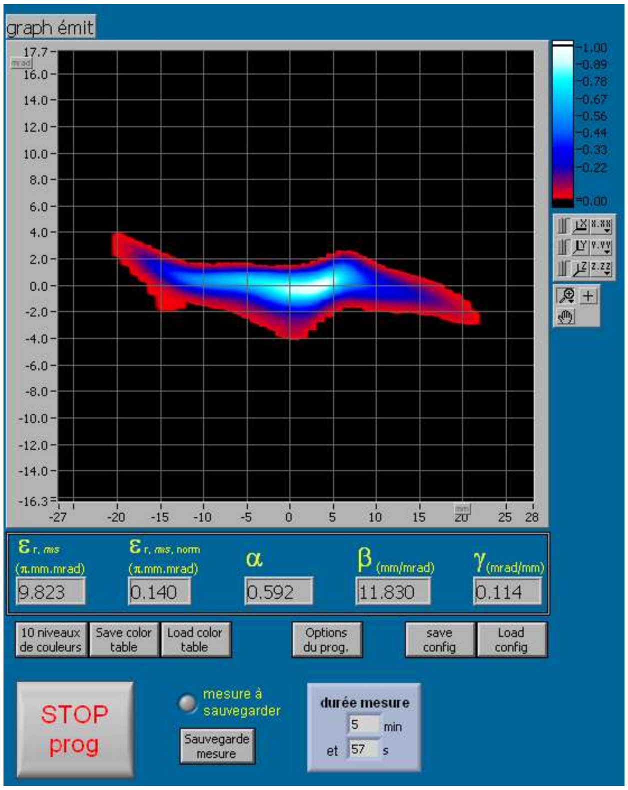

$\varepsilon_{r,\,rms}$ (π.mm.mrad) 9.823

$\varepsilon_{r,\,rms,\,norm}$ (π.mm.mrad) 0.140

α 0.592

β (mm/mrad) 11.830

γ (mrad/mm) 0.114

○ mesure à sauvegarder

durée mesure 5 min et 57 s

Figure 4.1.14: *The LabVIEW front panel.*

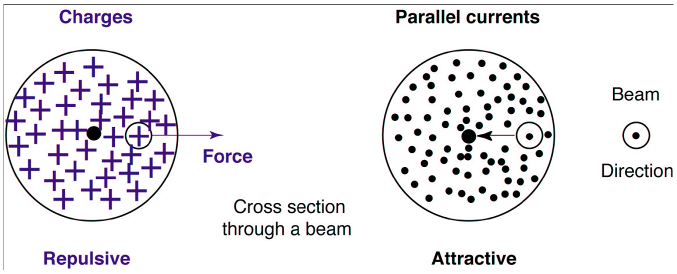

Figure 4.1.15: *Electrostatic and magnetic forces on a test particle within a cylindrical unbunched beam [75].*

with circular cross section (see figure 4.1.15), the Coulomb repulsion pushes one fo the test particles away from the beam center[5]; the overall force is zero in the beam center and increases towards the edge. Ion particles move with velocity $v = \beta c$, each ions represents parallel currents $I = ve$ which attract each other by the effect of their magnetic fields. The overall effect is still repulsive but decreases with the speed; special relativity implies that the forces become equal at the speed of light and thus cancel.

The extracted beam would suffer from the influence of space charge force, which would diverge the beam with increasing intensity. However, from experience, it is known that space charge compensation will build up fast and do exist even in magnetic dipoles. If no external electric fields are applied, the space charge force will be compensated by electrons, created by collisions of primary beam ions with residual gas atoms, and trapped within the positive space charge potential as the SC is not fully compensated. Another source of compensating charges is sputtering of primary ions at surrounding surface. The positive potential dip of the positive ion beam will be filled with electrons, minimizing the absolute potential dip with time. This process ensures that the electrons with highest energy might escape the potential dip, but that the remaining trapped electrons will become colder with time because of collisions [76].

The parameters of extraction geometry, as electrode aperture, electrode gaps and electrode shapes were optimized to reduce only emittance distortions because of the ion energy spread, that is determined by the plasma generator. The first spread of divergence values occurs on the downstream side of extraction system, where the equipotential surface bulge out through the last aperture electrode, and produce transverse field components that lead to the so-called aperture-lens effect. This non linear effect again results in an increase of the effective emittance.

In our emittance measurements we didn't inject gas (as Argon) in the LEBT, but after extraction system there is a focusing solenoid which allows to change the strength of the corrector dipole magnets (see figure 3.1.8). When a beam travels through a solenoid, its horizontal and vertical dynamics

---

[5] Particle with same charge experience the repulsion due to the Coulomb force.

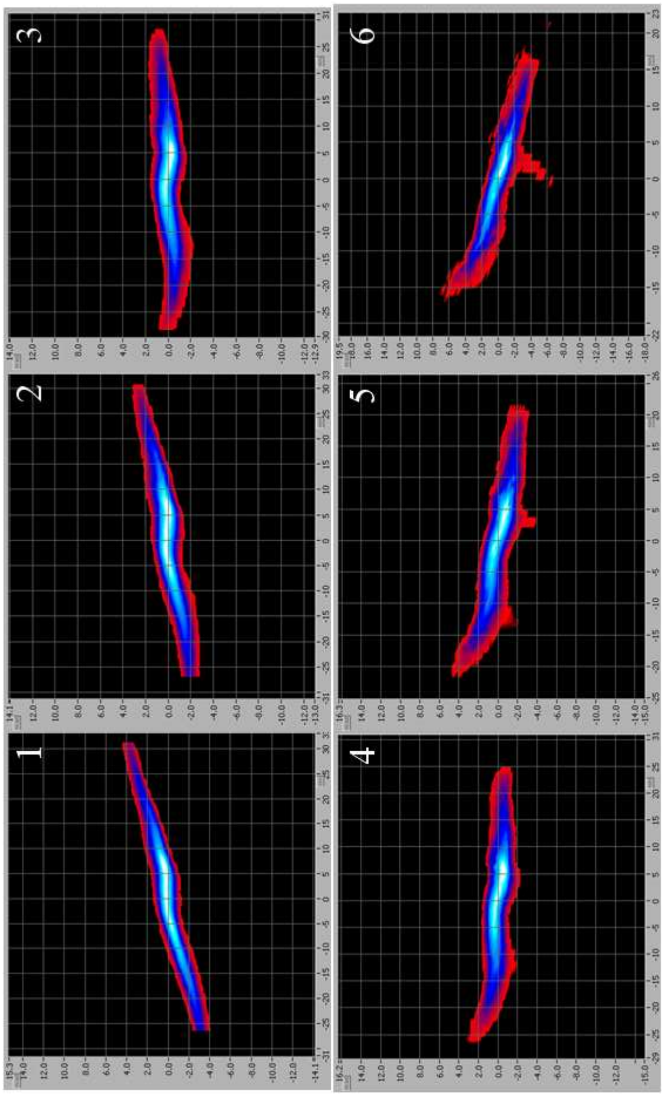

Figure 4.1.16: *Proton beam emittance measured for different Solenoid current (from* 180 *to* 250 *A) (* $P_{source} = 2.3 \cdot 10^{-5}$ *mbar*, $P_{Line} = 1.5 \cdot 10^{-5}$ *mbar*, $P_{frw} =$ 700 *W*, $V_{Ext} = 60kV$*).*

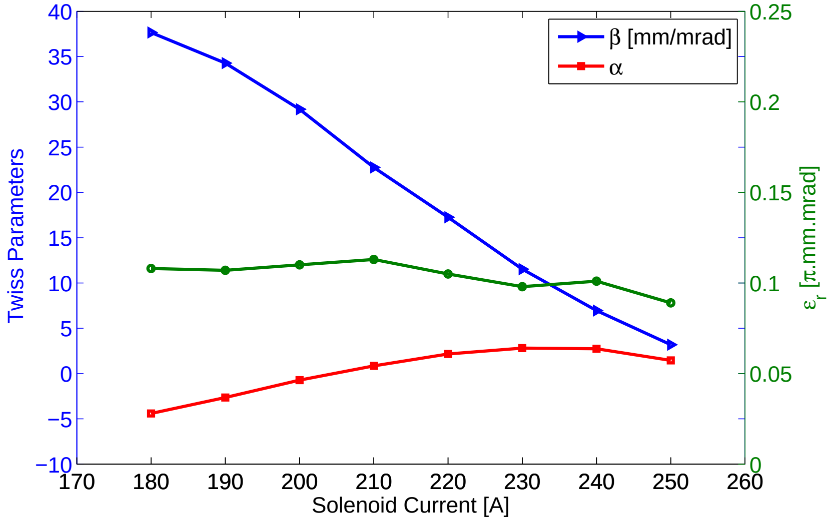

Figure 4.1.17: *Beam emittance and variation of Twiss parameters at* 60 kV*, by changing the focusing strength of the beam line solenoid from about* 180 A *to about* 250 A *(*$P_{source} = 2.3 \cdot 10^{-5}$ $mbar$*,*$P_{Line} = 1.5 \cdot 10^{-5}$ $mbar$*,* $P_{frw} = 700$ W*).*

are coupled due to the beam rotation by the solenoidal field. When the beam leaves this solenoid, an azimuthal velocity component causes a rotation of the original quadrupole axis as well as a remaining twist. Whereas the twist cannot be removed from the beam, the rotation of the quadrupole axis might be corrected by an additional beam line solenoid of reverse polarity with respect to the ion source solenoid [76].

If we consider a solenoid, that has a length of L, inside the solenoid, for $0 < z < L$, the magnetic field is uniform ($\vec{B} = B_0\hat{z}$). The magnetic field is zero outside the solenoid. For region near $z = 0$ and $z = L$, the field rises rapidly from zero to B_0 (or drops from B_0 to zero). When a charged particle beam passes through a uniform solenoidal magnetic field, the trajectory of a charged particle is in general a helix.

But near the two ends of the solenoid, $z = 0$ and $z = L$, where the axial magnetic field is changing, Maxwell equation suggests that there exists a radial component of the magnetic field[6]. This radial field component gives an azimuthal kick to the particle when it enters or exits from the solenoid [77].

The change in the azimuthal momentum can be obtained from the Lorentz force law:

$$\triangle p_{\phi} \approx -\frac{qr\triangle B}{2} \tag{4.1.6}$$

where $\triangle B(z = 0) = B_0$ and $\triangle B(z = L) = -B_0$. An important implication of the model is that the azimuthal kick received by the particle when it enters the solenoid $(z = 0)$ cancels that one at the exit $(z = L)$, as expected since the conservation of canonical angular momentum is zero.

We have seen this phenomena in our device, in fact by changing the solenoid current to increase the strength of the magnetic field the beam rotated with respect to the axis solenoid, as shown in figure 4.1.16.

The Twiss parameters determine the shape and orientation of the ellipse in phase space when the beam is transmitted through the focus solenoid, as we have described in the section 1.5.1. Figure 4.1.17 shows the beam emittance and Twiss parameters dependence on the solenoid current over the range of $180 - 250$ A. First of all we can observe that the emittance values only slightly change with the beam intensity. This is due to Liouville's theorem, described in the section 1.5. When we have increased the strength of the magnetic field, β decreased because there was a strong focusing force acting on the proton beam. Instead α got negative values (diverging beam) in correspondence of low solenoid current, then assuming positive values (converging beam) for high solenoid currents. By the figure 4.1.17 obtained at 60 kV, we can deduce that the best operating conditions have been obtained when we have set 230 A as solenoid current, because for current values higher than 230 A α decreases. So we cannot increase indefinitely the strength of the magnetic field, because if we focus the total beam in a smaller area in phase space, then nonlinear effects due to space charge arise.

---

[6] From Maxwell equation the radial component of the magnetic field is

$$B \approx -\frac{r}{2}\frac{\partial B}{\partial z}. \tag{4.1.5}$$

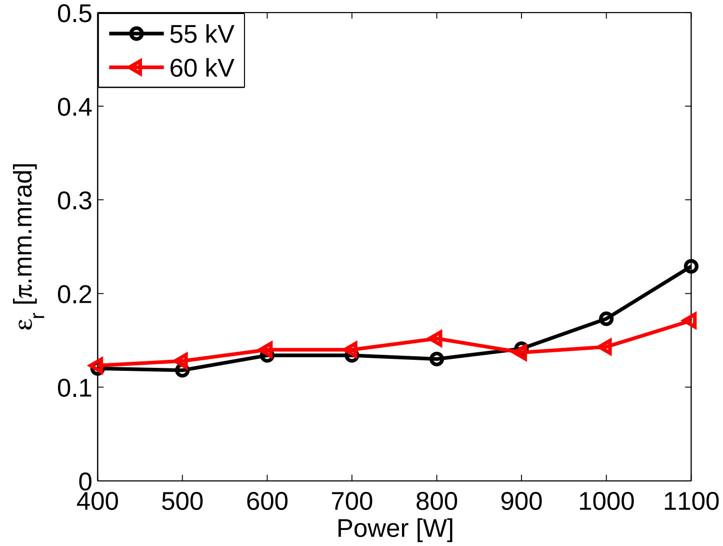

Figure 4.1.18: *Variation of beam emittance as a function of microwave power for two high voltage values,* $P_{Source} = 2.3 \cdot 10^{-5}$ *mbar.*

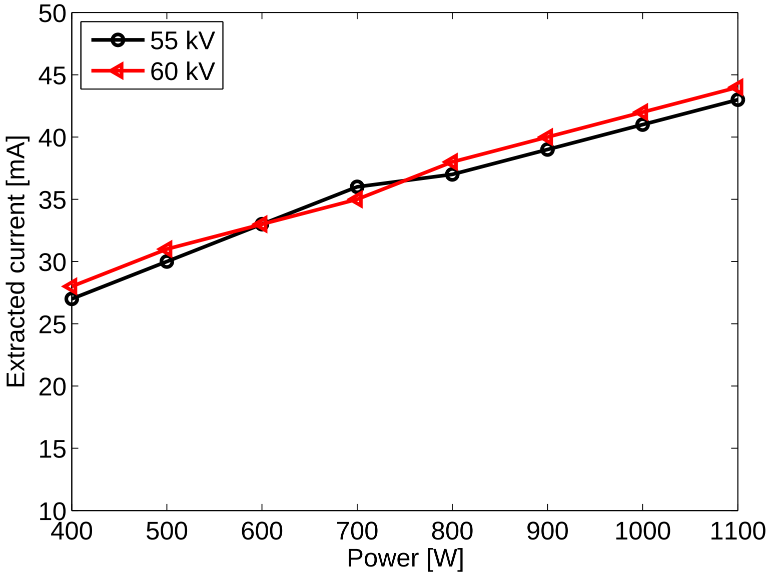

Figure 4.1.19: *Variation of beam current as a function of microwave power for two high voltage values,* $P_{Source} = 2.3 \cdot 10^{-5}$ *mbar.*

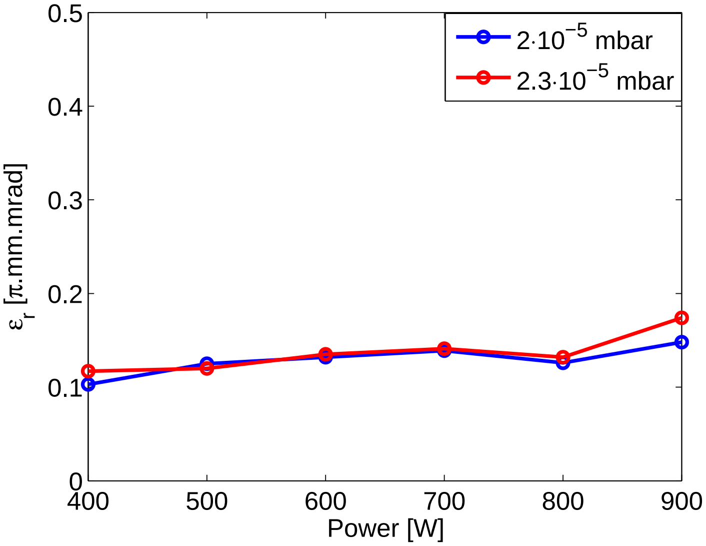

Figure 4.1.20: *Variation of beam emittance as a function of microwave power for two pressure values, puller voltage*= 55 *kV*.

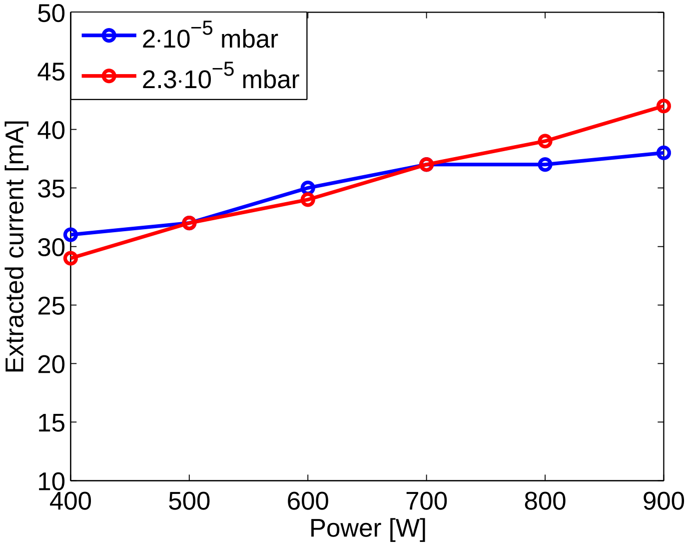

Figure 4.1.21: *Variation of beam current as a function of microwave power for two pressure values, puller voltage*= 55 *kV*.

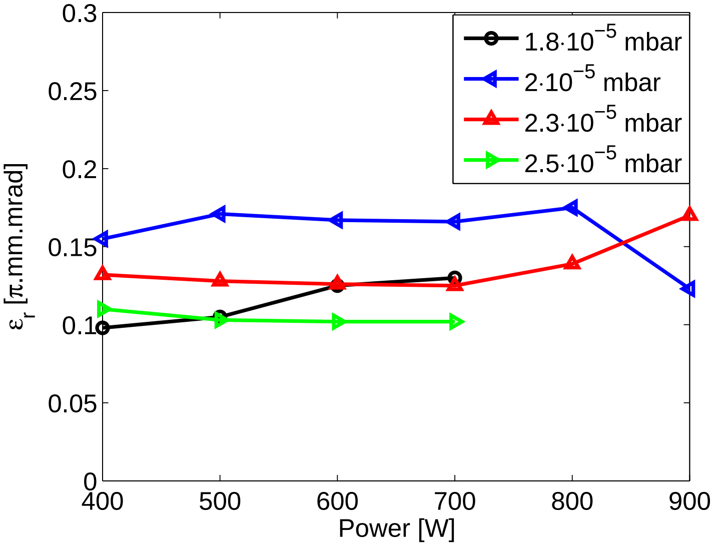

Figure 4.1.22: *Variation of beam emittance at* 60 *kV for different pressure values* .

When the permanent magnets were shifted of 8 mm from the initial position emittance measurements were repeated, for different microwave powers and for two puller voltage values (60 and 55 kV). The rms emittance, shown in figure 4.1.18, increases with the microwave powers (especially from 400 to 1100 W), because for higher currents we have stronger space charge effects. In fact taking into consideration the intensity of beam current (measured contemporaneously at emittance measurements), for both high voltage, one can see in figure 4.1.19 that, as we have wrote in the section 4.1.1, ion current increases with extracted voltage and changes of 40% with the power [7]. From the figure 4.1.18 operating at pressure of $2.3 \cdot 10^{-5}$ mbar, the beam emittance changes from 0.12 to 0.17π mm mrad at 60 kV and from 0.12 to 0.23π mm mrad at 55 kV; the variation of beam emittance depends on the puller voltage value. It is very interesting to note the differences in the emittance values calculated for two puller voltage, when the microwave power

---

[7] The emittance measurements were always compared with the extracted current, measured at the same time

values were higher than 900 W: the lower emittance has been obtained at 60 kV because when the source extracted higher current became relevant the space charge effects. The space charge field can decrease by applying higher acceleration potential.

Figures 4.1.20, 4.1.22 show the emittance measurements as a function of the pressure. The magnetic system has been shifted of 6 mm from the initial position in figure 4.1.20, where the pressure has been changed for two values, $2.3 \cdot 10^{-5}$ and $2 \cdot 10^{-5}$ mbar. By varying the power from 400 to 900 W, we can see that the emittance's trend is almost constant and the beam divergence remains below 0.17π mm mrad.

The measurements carried out at 60 kV for four pressure values are shown in figure 4.1.22; we can see that the beam divergence has its lowest value when the pressure (near the chamber) is about $2.5 \cdot 10^{-5}$ mbar. But the corresponding values of the beam current, reported in figure 4.1.5, are lower than the other measurements, so low beam intensity means low beam divergence because of the space charge effects decrease. In adding at $2.5 \cdot 10^{-5}$ mbar the electron temperature decreases because of collisions between electrons and neutral particles. The electrons didn't have energy high enough to ionize all hydrogen's molecules and consequently the total current extracted from the source keeps a low intensity. The best experimental condition has been obtained at a pressure of $2.3 \cdot 10^{-5}$ mbar: for this configuration the source performed the highest current with lower emittance values.

In figure 4.1.23 we can estimate the emittance variation with respect to the permanent magnets position: the ion beam intensity (4.1.24) and ion beam emittance change as a function of the magnetic induction in the region of the microwave window. The most important plasma parameters, like ion energies, plasma densities, electron temperature, depend substantially on magnetic field configuration. Figure 4.1.23 shows that the permanent magnets configuration with the highest divergence beam has been achieved when the permanent magnets were at home (the magnetic system did not move). In all the other configurations the emittance values are lower than 0.2π mm mrad, and change slightly with microwave power. When we shifted

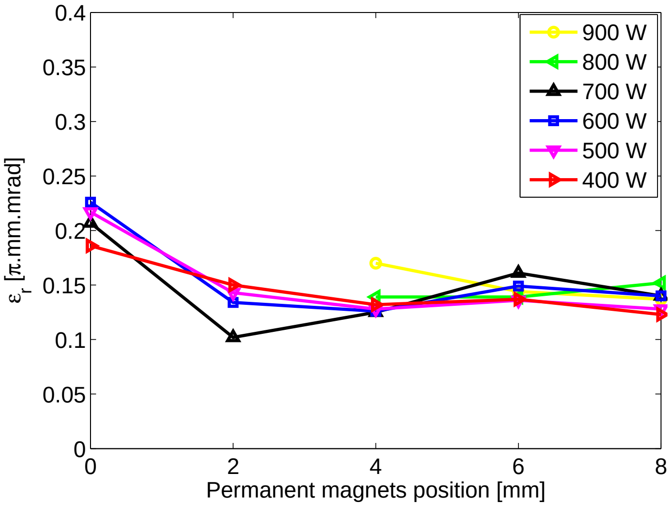

Figure 4.1.23: *Variation of beam emittance at* 60 *kV*, $2.3 \cdot 10^{-5}$ *mbar for different permanent magnets position.*

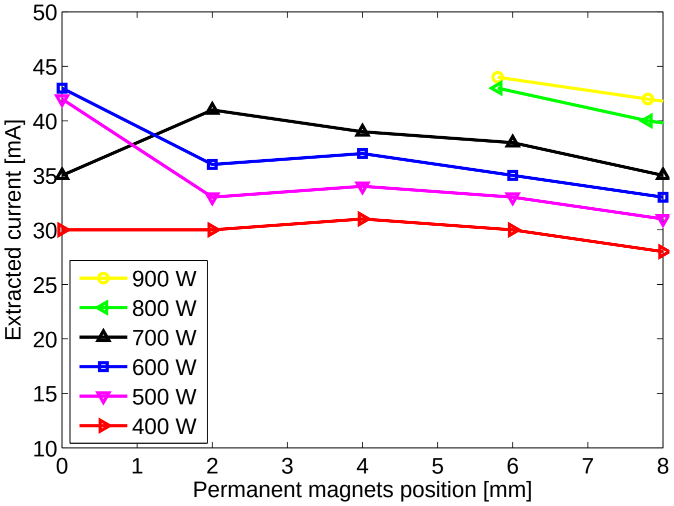

Figure 4.1.24: *Variation of beam current at* 60 *kV*, $2.3 \cdot 10^{-5}$ *mbar for different permanent magnets position.*

the permanent magnets towards the microwave window of six and eight millimeter, the total extracted current decreased so if one wanted to extract higher currents, it needed to apply a larger microwave power. In particular, by moving the magnets 8 mm away and by applying a total power of 1100 W maximum current of about 44 mA has been obtained. The same current value (44 mA) has been achieved at lower microwave power, 900 W, when the permanent magnets were shifted of 4 mm.

By means of figure 4.1.23 we have identified the worst permanent magnets configuration with respect to beam emittance. In fact, when the magnetic system was not moved, the higher emittance values have been calculated; with the increase of microwave power from 400 to 700 W the beam divergences fluctuated between $1.9 - 2.3\pi$ mm mrad. The variation of beam current at the same microwave powers and permanent magnets position, shown in figure 4.1.24, had a transition: at 500 W increases with the power ($\sim$ 44 mA), at 600 W stays unchanged ($\sim$ 43 mA) and then at 700 W decreases (35 mA). This phenomenon has been observed at different hydrogen mass flow, so this magnetic system position doesn't allow to generate stable ion beams with low emittance values [78, 79, 80].

In a previous work with the TRIPS source [43], it has been observed that the emittances significantly change when gas is injected into the beamline. So if we compare our measurements with the ones carried out on TRIPS without gas (puller voltage 40 kV, by changing the discharge power from 450 to 650 W) we find comparable values. In other works [60, 81] it is shown that at high-currents the beam was more space-charge compensated in presence of a high-pressure gas (10^{-5} Pa) into beamline, instead A. BenIsmail et al. [82] have studied the neutralization of proton beam[8] induced by the secondary charged particles produced by ionization of the residual gas.

---

[8] The space charge force is reduced and even cancelled by the charges trapped in the beam potential well

4.2 SILHI characterization in pulse mode

4.2.1 Analysis of the pulses ion beam

The SILHI source was operated with hydrogen fluxes of about $3 - 4$ sccm, resulting in a working pressure of approximately $1.4 \cdot 10^{-5}$ Torr. By means computer control we have set the applied voltage at:

1. High voltage platform = 85 kV;
2. Intermediate electrode $\sim$ 25 kV;
3. Repeller electrode ~ -2 kV.

In addition we have chosen the current values of the two coils (producing the axial magnetic field in the plasma chamber), in order to have a steady ion beam in different experimental configurations. Once the plasma discharge was established, the solenoid coil current was adjusted to obtained the desired magnetic field configuration which was able to focus the proton beam in a diagnostic box. These values have been kept costant for all the measurements time.

We can select cw mode or pulse mode by changing synthesizer operations. In the case of the pulse mode operation, synthesizer is operated by the shaped signal from the function generator in order to lunch the pulsed microwaves with the required average amplitude, width and duty cycle. Typical incident power has been fixed at 600 W, and pulse duration and frequency have been changed from 1 to 10 ms and from 10 to 40 Hz, respectively.

The duty cycle D_c, is defined by the product of the pulse duration t_{on} and the frequency f:

$$D_c = t_{on} \cdot f \tag{4.2.1}$$

In order to analyze the rectangular shaped pulse, a rise(fall) time t_r (t_f) has be defined, representing the time required for a signal to change from a specified low (high) value to a specified high (low) value. Typically, these values are $\sim$ 1% and $\sim$ 17% of the step height [83]. The time evolutions

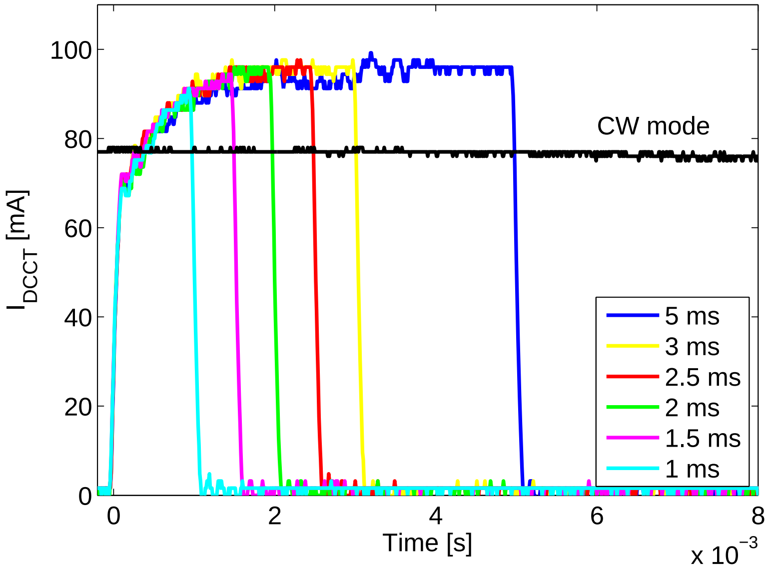

Figure 4.2.1: *Pulse wave forms of beam current for different pulse lengths at* 30 *Hz. (The pressure is* $1.4 \cdot 10^{-5}$ *Torr, the power is* 600 *W.)*

of ion saturation currents and the beam currents are measured by a digital oscilloscope directly.

In figure 4.2.1 the time dependence of the ion current is measured for different pulse length at a constant frequency of 30 Hz. The steady-state values of the ion beam changed from 83 to 96 mA, and for all pulses the rise and fall times did not exceed $t_r = 0.16 \cdot 10^{-3}$ s and $t_f = 0.17 \cdot 10^{-3}$ s, respectively. In addition, these ion currents have been compared to those ones measured during continuous operation using the same parameters. It is found that in pulsed mode the beam currents were more intense than those ones obtained in cw mode operations. We obtained the maximum current at pulse duration of 10 ms.

In these experiment at each pulse length and frequency we optimized the tuning of microwaves in order to obtain the maximum ion current at the same incident power of the cw operations (about 600 W). Figure 4.2.2 shows the profile of the extracted ion beam currents measured by DCCT in the pulse microwaves operations. We can see the dependence of time-averaged

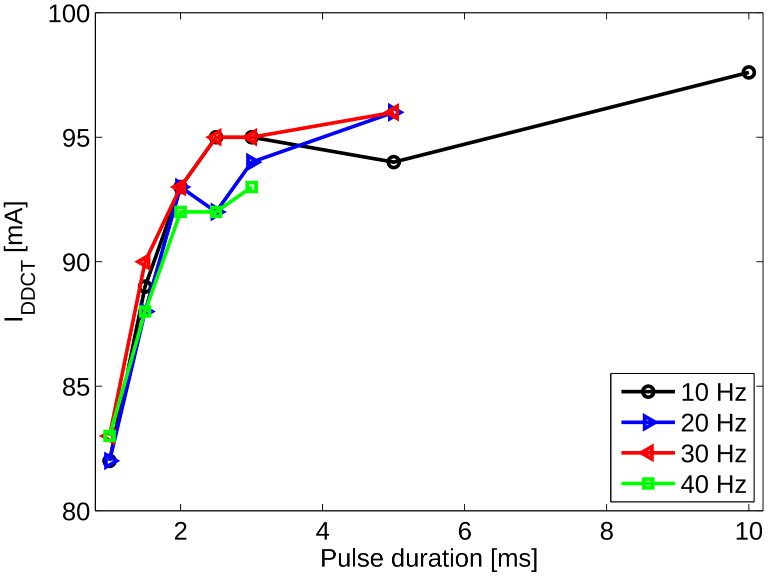

Figure 4.2.2: *The trends of the extracted ion currents in pulsed mode as a function of the pulse length for different frequencies. (The pressure is* $1.4 \cdot 10^{-5}$ *Torr, the power is* 600 *W.)*

extracted current as a function of pulse length for different frequencies. An increase of pulse length causes a contemporary increase of the ion beam current, as shown in figure 4.2.1. Instead lowly ion currents has been measured in correspondence of short pulse duration, where the deviation of the real pulse shape from the ideal, rectangularly shaped function becomes more significant.

From the figure 4.2.2, it can be seen that for pulse durations shorter than 3 ms the time-averaged ion current grows rapidly from about 83 to 95 mA. For pulse durations longer than 3 ms the total current slightly increases linearly. Furthermore, the total current changes slightly with frequency.

The maximum ion currents, equal to 98 mA, was obtained at a frequency of 10 Hz and a pulse duration of 10 ms. The gain of total currents with respect to the corresponding cw operations was $\sim 30\%$ (in cw we obtained 77 mA).

Measurements of plasma parameters were performed either in cw and pulsed mode by means of a Langmuir probe [84]. It was found that the electron density in the pulsed mode was larger than in cw mode, while the electron temperatures were lower. These evidences explain the better performance in pulsed mode. Hirai et al [84], looked to the temporal evolution of the n_e and T_e in ECR plasmas. It is found that these diffusion time are different in the off phase of incident microwave power. The diffusion time of the n_e is slower than that of the T_e. The long decay time of n_e in pulse mode is considered to cause higher n_e level than that in cw mode. This phenomena generates the increase of the extracted ion beam current in the pulsed mode.

We can think to compare the time-average ion beam currents as a function the duty cycle, as reported in figure 4.2.3; the reason for this choice is that D_c contains information on both the pulse length and pulse frequency. The total ion current enhances increasing the duty cycle, at constant frequency this corresponds to an increase of the pulse duration (as we have seen in the previous figure 4.2.2). In table 4.2 we have reported the duty cycle values for the different experimental conditions; if we considered the measurement performed at the same duty cycle, the maximum current has been obtained at the highest frequency.

4.2.2 Emittance measurements

The emittance measurements has been realized with the same device used with the VIS source, but working in pulsed mode the measurements were more complicated: we had indicate the start and the stop time of the emittance measurements.

From the software interface (LabVIEW), see figure 3.4.3, we selected the *Mesure pulsée* option, and then we decided when the start time of each measurement, more in detail we have inserted a delay, in μs from the start of microwave power (this delay and the rise time had the same order of magnitude). In addition we could choose the stop measurements time; therefore for each configuration we have determined the portion of the signal to be analyzed. Finally, the number of pulses to be averaged was included.

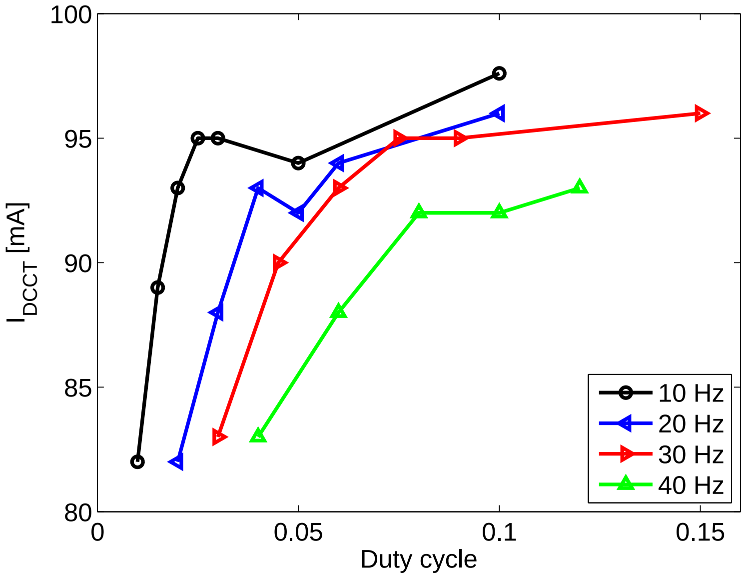

Figure 4.2.3: *Variation of the ion beam as a function of duty cycle for different frequencies.*

Table 4.2: *Duty cycle calculated for all experimental configurations (at* 600 *W and* $1.4 \cdot 10^{-5}$ *Torr).*

Duty Factor							
	10 ms	5 ms	3 ms	2.5 ms	2 ms	1.5 ms	1 ms
10 Hz	0.1	0.05	0.03	0.025	0.02	0.015	0.01
20 Hz		0.1	0.06	0.05	0.04	0.03	0.02
30 Hz		0.15	0.09	0.075	0.06	0.045	0.03
40 Hz			0.12	0.1	0.08	0.06	0.04

The beamlet divergence, as we have described in the section 4.1.3, is deduced from the width of the current peak collected on the wire for all device positions[9]. It can see from the figure 3.4.3, that the proton peak is made of many points. When the source produced a pulsed beam, each current pulse generated one point of the peak at a fixed electric field value. In addition for each point the EMU can mediate the measurements for many pulses (generally we considered two or three of pulses).

In figure 4.2.4 we have reported the emittance measurement at 30 Hz and 3 ms. This emittance picture is different with respect to those ones obtained with the VIS source: the two source have unlike extraction system (four electrodes for VIS and five electrodes for SILHI) and different low energy beam transport line. Therefore the two sources produce ion beams differently distributed in phase space, this generating different emittance pictures.

By working in pulsed mode, we set the temporal part of the signal to analyze by means of the EMU; we initially verified how changed the emittance values when changing the delay settings (the increase of the delay means to analyze a smaller part of the ion pulse). The delay has been changed at fixed pulse lengths as shown in figure 4.2.5. The figure represents the variation of the emittance, obtained by a microwave pulse of 30 Hz and 5 ms, for four different delay values. It can be seen that the difference between minimum and maximum emittance values is $\sim 6\%$.

Figure 4.2.6 and table 4.3 summarize the emittance measurement as a function of duty cycle for different pulse length and frequency. The emittance increased with duty factor, because we have seen in the figure 4.2.3 that there are higher currents in correspondence of higher duty cycle values. The best compromise between high values of ion currents and quality of the extracted beam has been obtained by operating at 30 Hz. In fact, the emittance values changed from 0.13 to 0.153π mm mrad for the beam currents that increase from 83 to 96 mA.

The table 4.3 shows all the measurements: at 10 Hz, we have obtained higher beam current and emittance values, while at 40 Hz we have obtained

---

[9] The EMU can be moved vertically long a beam diameter.

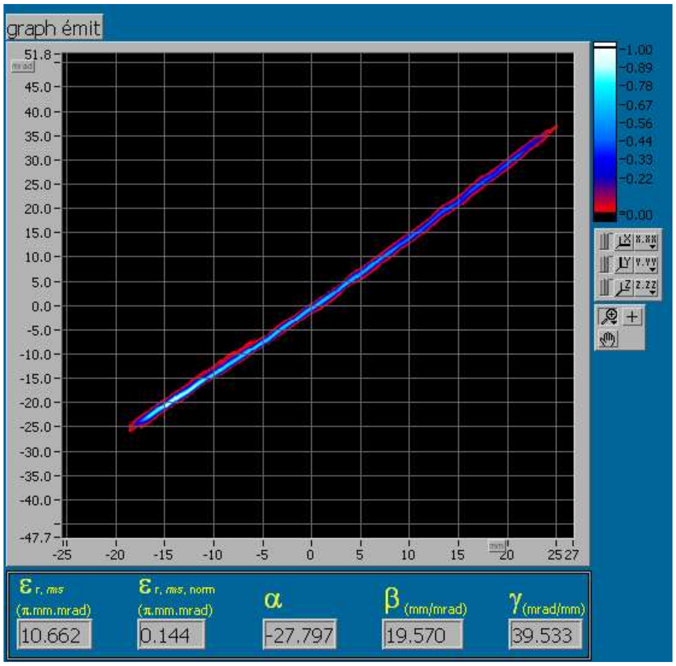

$\varepsilon_{r,\,rms}$ (π.mm.mrad) 10.662

$\varepsilon_{r,\,rms,\,norm}$ (π.mm.mrad) 0.144

α -27.797

β (mm/mrad) 19.570

γ (mrad/mm) 39.533

Figure 4.2.4: *Emittance picture for SILHI source, by working in pulsed mode at* 30 *Hz and* 3 *ms pulse length.*

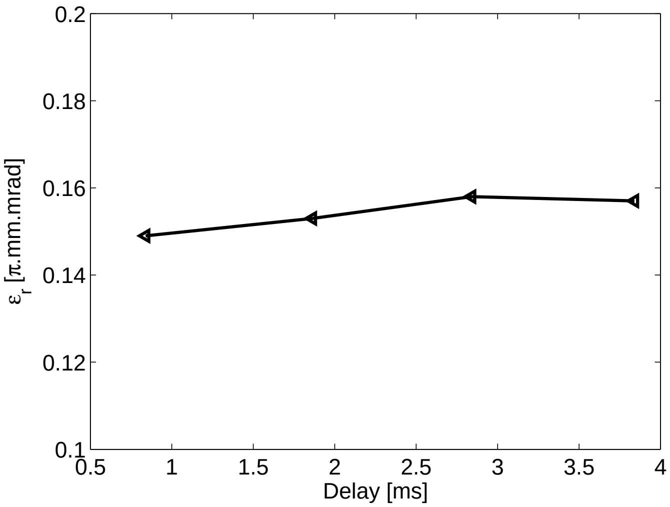

Figure 4.2.5: *Emittance values obtained for different part of the same pulse at* 30 *Hz and* 5 *ms. .*

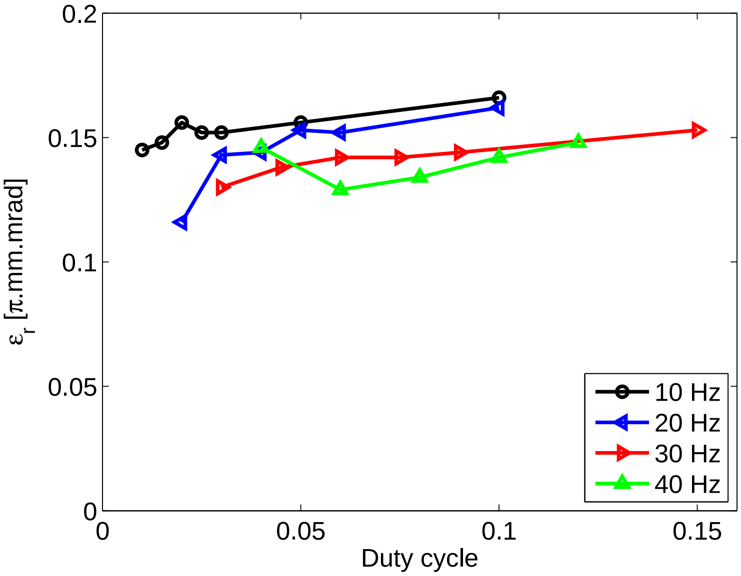

Figure 4.2.6: *Emittance profiles as a function of duty cycle for different frequencies.*

Table 4.3: *Emittance measurements for all experimental configurations (at* 600 *W and* $1.4 \cdot 10^{-5}$ *Torr).*

Emittance [π mm mrad]							
	10 ms	5 ms	3 ms	2.5 ms	2 ms	1.5 ms	1 ms
10 Hz	0.166	0.156	0.152	0.152	0.156	0.148	0.145
20 Hz		0.162	0.152	0.153	0.144	0.143	0.116
30 Hz		0.153	0.144	0.142	0.142	0.138	0.13
40 Hz			0.148	0.142	0.134	0.129	0.146

lower beam currents and emittances. In adding if we consider the measurements at fixed duty cycle, for example:

1. duty cycle = 0.03
2. duty cycle = 0.06
3. duty cycle = 0.1

we observed tant in each configuration the lower emittance values were closely related to the lower ion beam intensity.

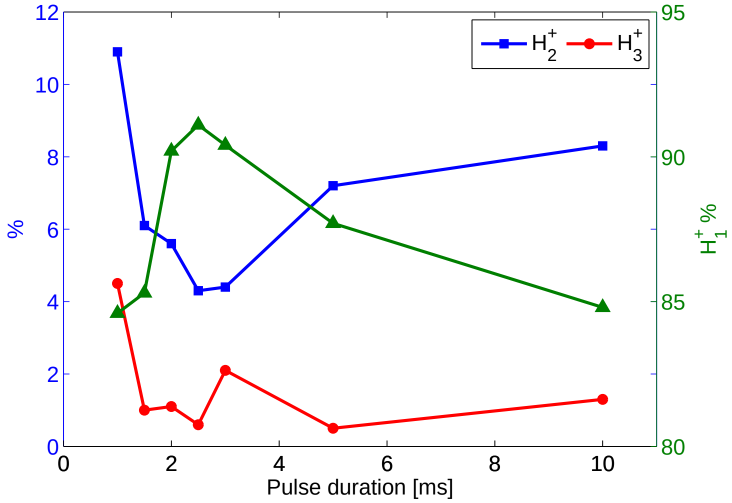

Figure 4.2.7: *Components of ion beam as a function of pulse length, at* 10 *Hz. .*

The SILHI source works also in cw mode, so we compared the beam intensity and emittance with the values obtained in pulsed mode. In continuous mode we didn't change the source parameters, working with the same settings of high voltage and solenoids current. Only the hydrogen gas flow was adjusted to make more stable the beam current. In cw mode at 600 W the SILHI source produced about 77 mA of proton beam, with an emittance of 0.109π mm mrad. The beam emittance was then lower with respect to the values measured in pulsed mode. This is due to the lower beam current.

We increased the power in order to compare the emittance in pulsed and cw mode for the same extracted proton current. At 670 W the source generated proton current higher than 90 mA with an emittance value like 0.177π mm mrad.

Setting the same microwave power of 600 W and extracting approximately the same current (higher than 90 mA), the lower rms emittance value was obtained in pulsed mode.

The proton fraction was analyzed by using the EMU Wien filter, when the device is aligned with respect to the LEBT axis. The EMU divides the different ion species and only of a part of the beamlet can pass through the beamlet slit and is collected by means of a wire. Figure 4.2.7 shows the species fraction as a function of the pulse length: more than 85% is the fraction of H^+. The other species contribute at a much smaller amount, being within 11% the H_2^+ and lower than 4% the H_3^+

Chapter 5

Methods to improve the intensity of ion beams in MDIS

It has been observed that in the ion sources it is necessary to have an electron density large enough for efficient ionization and for high beam currents. There are different methods able to increase the electron density: they are active e passive techniques [9]:

1 Passive techniques:

- BN disk and wall coating effects;
- Biased electrodes techniques.

2 Active techniques:

- Ferroelectric Cathodes;
- Electron gun.

VIS and SILHI sources usually adopt passive technique: as described in the chapter 3, thick BN plates are located at two extremities of the plasma chamber. Due to high secondary electron emission coefficients of nitride plates, the electron densities in the discharge is enhanced leading to increase dissociative ionizations of the hydrogen atoms and molecules. The wall conditions are also an important parameter and many chemical wall coatings may be useful electron donors. The secondary electrons can either return towards the central plasma or neutralize the ions near the walls and subsequently reduce the ambipolar electron drain. In both cases they improve the electron density inside the MDIS [73]. In the section 5.1 it is described the behavior of the VIS source when a 5-mm-thick Al_2O_3 tube is embedded in the plasma chamber.

A negatively biased disk, with a voltage of a few hundred volts with respect to the source voltage, and located at the injection end of the plasma chamber, is usually employed in ECR ion source. This biased disk reflects electron back to the central plasma and attracts ions, producing secondary electrons, which are then accelerated into the plasma chamber. As a consequence the electron density of the plasma increases [85].

Active materials, like ferroelectric cathodes, such as PBZT doped with 2 % of Bi_2O_3, have been employed because of their capability of producing high emission yields of energetic electrons [86]. However, their robustness is not sufficient for stable applications into ECRIS. In fact, they showed not only a lack of reliability, but also a little resistance to plasmas, and they failed after short time.

The electron guns technique [7, 87], which makes use of CNTs-based electron guns, has been used with the CAESAR source, and it will be described in the section 5.2.

5.1 Passive technique: coatings of Al_2O_3

In the past several passive techniques for the injection of the secondary electrons were tested on the TRIPS source. With the tick alumina tube not only was possible to extract a more intense current with a larger proton fraction, but a lower beam ripple and better stability were also observed.

A series of measurements were carried out with the VIS source by inserting a thick Al_2O_3 tube inside the plasma chamber, shown in figure 5.1.1. The test, here reported, was carried out in the same conditions of magnetic

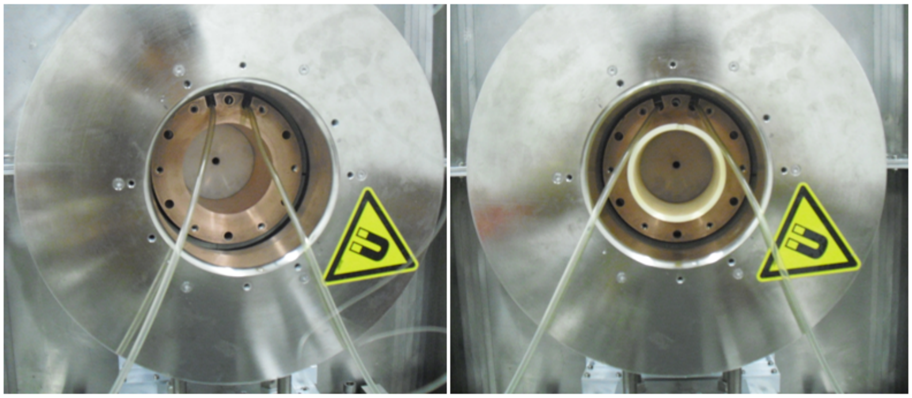

Figure 5.1.1: *(on the left) The copper plasma chamber without Al_2O_3. (on the right) The copper plasma chamber with Al_2O_3.*

field, and only rf power was changed, keeping constant its value during the comparative measurements with and without the Al_2O_3 tube. Its dimension are the following: inner diameter 79 mm, outer diameter 89.5 mm, length 95 mm. When Al_2O_3 is nested in the plasma chamber, it covered the entire walls from one side to other; furthermore there were two BN disks on both sides of the plasma chamber (injection and extraction flange).

The measurements have been carried out by changing the power from 250 to 1000 W, and at operating pressure of $2 \cdot 10^{-5}$ mbar, as shown in figure 5.1.2. The beam current when the $\mathrm{Al_2O_3}$ tube has been inserted into the chamber is always higher than the total current obtained when we have used only the BN disks. In particular between 600 and 850 W there was a more evident increment of the extracted current, higher than 25%. At very high microwave power the enhancement was only of $\sim 7\%$, because the efficiency of electron donors decreases with the increase of the electron energy.

The electron donors influences the plasma essentially by emitting cold electrons. Being accelerated in the sheath by the plasma potential, they will enter the plasma generally with energies in the order of several tens of eV [88]. The higher electrons density in turn demands higher amounts of positive charge, resulting again in a better confinements of ions with high charge states. This phenomenon is due to the decrease of the plasma

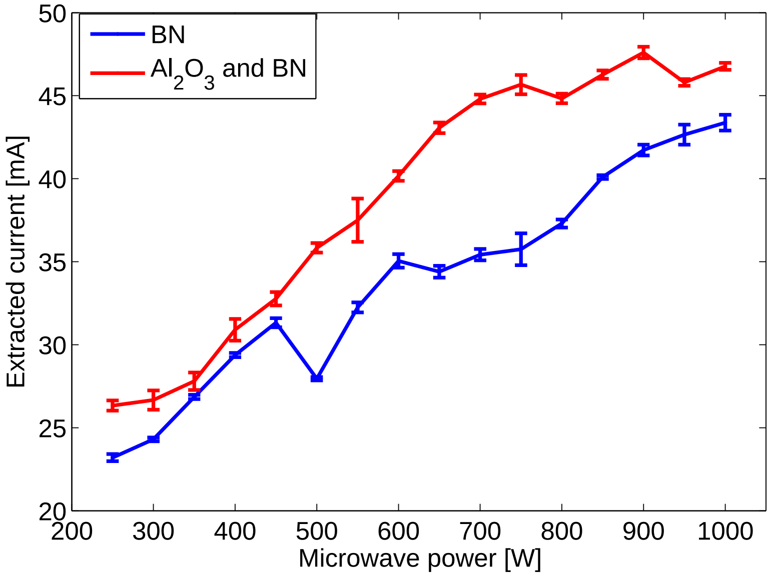

Figure 5.1.2: *The comparison of the total extracted current in two different experimental set-up.*

potential. A lower plasma potential will have a very important positive effect: it reduces the ionic losses towards the wall thus improving the ion confinement. The ion sputtering, consequently, will reduce, so that the plasma stability will improve [89].

The improvement of the performance with the use of alumina in place of a BN disk could be explained just by looking at the table 5.1 that shows the secondary electron emission coefficient values for Al_2O_3 and BN. Alumina has the advantage of a high rate of secondary electron emission even at low energy of the primary electrons[1]. Therefore, it is particularly suited for the microwave discharge ion source, in which the plasma electron energy is

---

[1] The study of the secondary electron emissivity of different materials has been determined by means electron impact, in fact δ_{max} has been obtained through the ratio of the secondary electron current (emitted from the Al_2O_3 or BN targets and collected by a faraday cup) and the primary electron beam current (emitted by an electron gun and directed toward on targets).

E_{max} is the primary electron energy value for which δ_{max} is maximum.

E_l is the primary electron energy value for which $\delta_{max} = 1$ [73].

Table 5.1: *Secondary emission* δ_{max}*, maximum yield* E_{max} *and characteristic energies* E_l *are listed for* Al_2O_3 *and BN.*

Material	δ_{max}	E_{max} (eV)	E_l (eV)
Al_2O_3	6.4 – 19	650 – 1300	25
BN	2.9	600	50

typically in the order of a few tens of eV, (15 to 40 eV have been measured with the Langmuir probe [90]). In this situation, the average yield δ that can be obtained by alumina surfaces is about a factor of 2 higher than for the BN surfaces.

5.2 Active technique: Electron guns

Electron guns can be made of different materials and designed by means of different technological solutions. We particularly employed an innovative technique based on Carbon Nanotubes (CNT). The name of this technique is CANTES[2].

In CANTES techniques, two electron guns are placed on a copper plate connected to the RF waveguide, that is usually employed as bias disk in the CAESAR source[3]. A potential in the range $0 - 2.5$ kV, is then applied between the chamber and the waveguide, and the same potential is used to produce the emission field (i.e. the extraction field) between CNTs and the anodic grid [7, 87].

The CNTs electron gun used for the test is made of three elements: a CNTs cathode obtained on a 300 μm thick silicon substrate, a 150 μm thick mica spacer and an anodic copper grid with quad cells of 350 μm side. CNTs eject electrons because of the field emission effect, i.e. quantum tunneling, which is obtained by applying an electric field higher than $3 - 4V/\mu m$.

---

[2] CANTES (CArbon NanoTubes as Electron Source) is the name of an experiment supported by the 5th Nat. Comm. of INFN.

[3] CAESAR is an ECR ion source, operating as injector for the K-800 Superconducting Cyclotron, has been used as testbench for the CANTES technique.

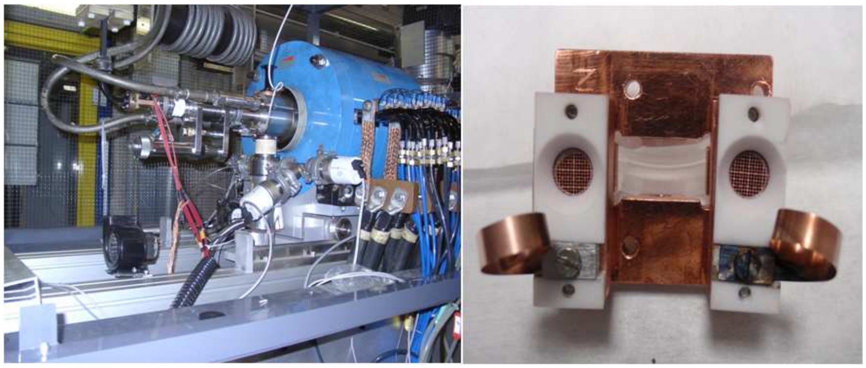

Figure 5.2.1: *(on the left) CAESAR source. (On the right) The CAESAR bias disk, holding two CNTs electron guns.*

The gun elements are kept together by a MACOR holder, on which the electrical connection is obtained by an evaporated gold track. The MACOR holder is then fixed on a copper plate, i.e. the bias disk of the source, connected to the waveguide of the plasma chamber. The anodic grids are linked to the ground potential of the plasma chamber wall by means of copper creeping contacts. Two of such electron guns were mounted on the same bias disk during the experimental tests. A picture of a CNTs sample and the assembled guns is shown in figure 5.2.1. Prior to the plasma test, each CNTs sample was tested in terms of field emission, by means a custom-designed apparatus [91]. Emission measurements for sample tested in CAESAR produced current densities up to $50 - 100$ mA/cm^2.

The charge state distribution has been measured at different RF power and voltages applied to the CNTs electron gun for the Kr, working at fixed pressure. The Kr^{11+} extracted current has been particularly focused. The extracted currents can be compared with those obtained when the CNTs electron gun was switched off. The beam current exceeded the one obtained with the biased disk already at 1 kV, as it can be observed in figure 5.2.2. In spite of the small emission area, an increase of $30 - 70\%$ was obtained in any case (about 40% for Kr^{11+}).

From X-ray measurements, we have observed a relevant reduction of the number of higher energy electrons thanks to the electrons emitted by the

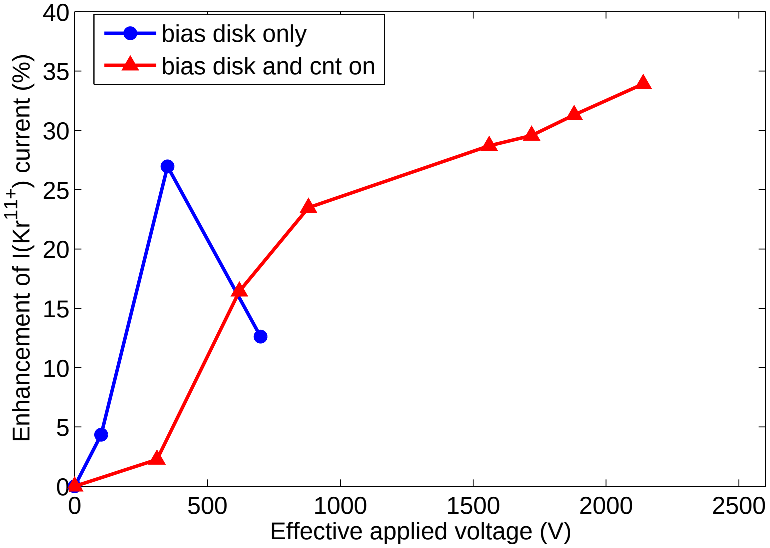

Figure 5.2.2: *Comparison of produced* Kr^{11+} *current when using conventional biased disk or emitting CNTs. The current has been normalized to its maximum value.*

CNTs-based electron gun. The current gain was between 30 and 70%. Once that a full comprehension of the phenomenon will be gained, this last result is quite promising for modern ECRIS which performances are strongly limited by the occurrence of such hot electrons when large power and frequencies above 18 GHz are used.

The use of CNTs-based emitters has solved robustness problem which emerged when ferroelectric cathodes were used. For these tests, their period of operation was limited to some tens of hours. Future experiments on ECRIS will focus on reliability tests, for one week or more.

In the future this new technique will be applied to the MDIS sources. The performance of the MDIS source is optimized when in the plasma core the numbers of electrons at low temperature below 10 eV is increased, as we have shown in the section 5.1 when an electron donor has been used. The MDIS sources require an electron gun, that will increases the intensity rather than temperature of electrons emitted by means the CNTs.

5.3 Alternative active methods for boosting the electron density

Others technique may also be studied to improve the source performance in terms of beam intensity. For example it has been demonstrated that the production of highly charged ion beams with ECR ion sources can be improved through the use of multiple frequency heating, which provides additional resonance surfaces for electron heating [92, 93]. In the section 4.2 it has been proved that the SILHI source produced at pulse mode higher currents than at cw mode.

In the next section we will introduced an innovative mechanisms of plasma ignition based on electrostatic waves (ESW) wich are able to a consistently increase electron density [8].

5.3.1 Theoretical treatment

A new experiment has been carried out in the last year at LNS. It consist of a new plasma ignition technique based on inner plasma mode conversion, this technique is very much promising ad it may be a standard tool in the next years to definitely overcome the current limitations the proton sources.

In order to overcome the electron density limitations in electromagnetically heated plasmas, we started with an experimental campaign aiming to electrostatic waves heating. ESW, in fact, do not suffer any density cutoff; they are able to propagate in overdense plasmas being absorbed at cyclotron harmonics, as demonstrated in large dimension fusion devices: with the WEGA Stellarator of Greifswald, densities up to $10n_{cutoff}$ ($n_{cutoffs} = 7.5 \cdot 10^{16}$ cm^{-3}) have been obtained at 2.45 GHz [94].

In cold magnetized plasma approximation, as we have described in the section 1.3, four typical waves propagate: R and L waves have $\vec{k} \parallel \vec{B}$ but different polarization, while O and X waves have $\vec{k} \perp \vec{B}$ and different orientation of the electric field with respect to $\vec{B}$. The X wave has a resonance when $\omega_{RF} = \omega_h = \sqrt{\omega_p^2 + \omega_c^2}$, the R wave has a resonance which takes place when $\omega_{RF} = \omega_c$; it is largely employed for plasma ignition either in multiply charged ion and/or proton sources [20], and provides a large number of

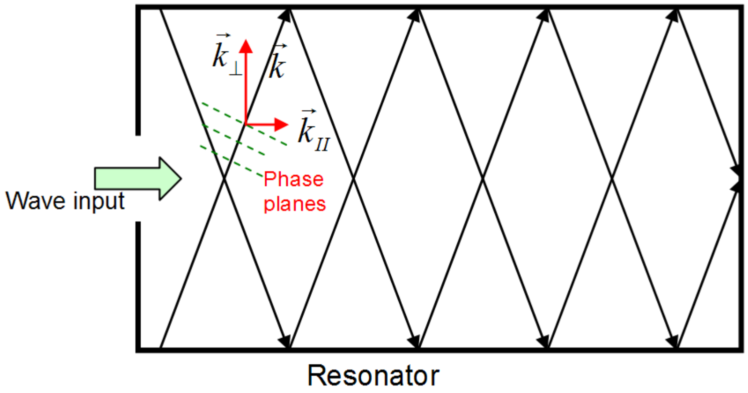

Figure 5.3.1: *Sketch of wave propagation inside a resonator: multiple wall reflections originate non parallel components of the k vector.*

energetic electrons (up to 1 MeV in ECRIS) but underdense plasmas.

In our device we launched the waves axially (i.e. with $\vec{k} \parallel \vec{B}$) inside a bounded volume (resonant cavity); the wave propagation is complicated by wall reflections: it is no longer a TEM mode. Being the $\vec{k}$ vector everywhere perpendicular to the phase planes, a perpendicular component of $\vec{k}$ originates with respect to B, as shown in figure 5.3.1. The field components are, in cylindrical coordinates:

$$\begin{aligned} E_r &= A J'_m(k_c r)\cos(m\phi)\sin\left(\frac{\pi p z}{h}\right) \\ E_\phi &= \left(\frac{B}{r}\right) J_m(k_c r)\sin(m\phi)\sin\left(\frac{\pi p z}{h}\right) \\ E_z &= C J_m(k_c r)\cos(m\phi)\cos\left(\frac{\pi p z}{h}\right) \end{aligned} \tag{5.3.1}$$

for the TM modes, and, for TE modes:

$$\begin{aligned} E_r &= \left(\frac{D}{r}\right) J_m(k_c r)\sin(m\phi)\sin\left(\frac{\pi p z}{h}\right) \\ E_\phi &= F J'_m(k_c r)\cos(m\phi)\sin\left(\frac{\pi p z}{h}\right) \\ E_z &= 0 \end{aligned} \tag{5.3.2}$$

where J$(k_c r)$, J$'$ $(k_c r)$ are the Bessel functions and their derivatives, z is the longitudinal coordinate; A, B, C, D, F are constants depending on the wave amplitude, and:

$$\begin{aligned} k_c^2 &= \left(\frac{\omega}{c}\right)^2 + k_z^2 \\ k_z &= \frac{2\pi}{\lambda_z} \end{aligned} \tag{5.3.3}$$

with $p\lambda_z = 2h$. Hence $\vec{k} = \vec{k}_\perp + \vec{k}_\|$. Terms $k_c r$ are connected to the zeros of Bessel functions, so that a triplet of integer numbers n, ν, r define the excited mode (the first two individuate the ν^{th} zero of the n^{th} Bessel function). Therefore the cavity wave will be neither pure perpendicular, nor pure parallel. In this case the Appleton-Hartree dispersion relation is valid [95]:

$$n_y^2 + n_z^2 = 1 - \frac{2X\left(1-X\right)}{2\left(1-X\right) - Y^2\sin^2\left(\theta\right) \pm \Gamma} \tag{5.3.4}$$

Where:

$$\Gamma = \left[Y^4 \sin^4 \left(1-X\right)^2 Y^2 \cos\left(\theta\right)\right]^{\frac{1}{2}} \tag{5.3.5}$$

$$\vec{n} = \frac{\vec{k}c}{\omega} \tag{5.3.6}$$

Here n$_y$, n$_z$ are the components of the refractive index vector, $X = \omega_p^2/\omega^2$ is the dimensionless density, $Y = \omega_c/\omega$ is the dimensionless magnetic field, θ is the angle between $\vec{k}$ and $\vec{B}$. The positive and negative sign in the denominator of 5.3.2 correspond to the O-mode and X-mode respectively. Although the O mode has no access in overdense plasmas, for some θ it can convert into the X mode at the O cutoff. The X mode, instead, can propagate inside the plasma bounded by the R and L cutoffs, which are given by:

$$\begin{aligned} \omega_L &= \frac{1}{2}\left(\omega_c + \sqrt{\omega_c^2 + \omega_p^2}\right) \\ \omega_R &= \frac{1}{2}\left(-\omega_c + \sqrt{\omega_c^2 + \omega_p^2}\right) \end{aligned} \tag{5.3.7}$$

If the UHR layer is enclosed by ω_L and ω_R the incoming X wave tunnels through one of them, and begins to be reflected back and forth passing

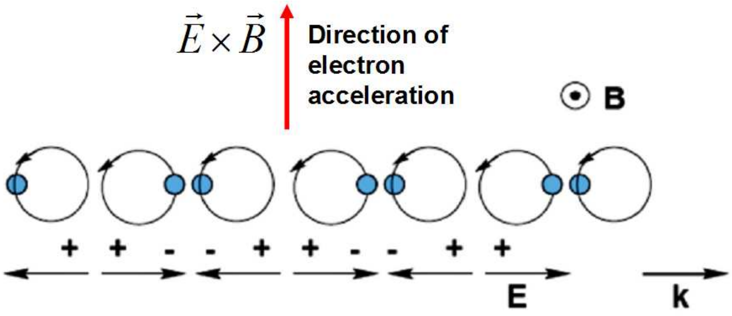

Figure 5.3.2: *Origin of the $\vec{E}\times\vec{B}$ the drift: the BW moves in the k direction and generate a longitudinal field which is intensified in proximity of the cyclotron harmonics.*

through the UHR. The X wave has normally a longitudinal component of the electric field (TM mode), that is emphasized close to the UHR layer where it adopts an electrostatic nature and becomes a Bernstein wave with $\vec{k}\perp\vec{B}$ and $\vec{E}\parallel\vec{k}$. Its dispersion relation is [12]:

$$1-\left(\frac{k_B\nu_{th}}{\omega_p}\right)^2 = e^{\left(-k_B^2r_L^2\right)}I_0\left(k_B^2r_L^2\right)-2\left(\frac{\omega}{\omega_c}\right)^2\frac{\sum_q e^{\left(-k_B^2r_L^2\right)}I_q\left(k_B^2r_L^2\right)}{q^2-\frac{\omega^2}{\omega_c^2}} \tag{5.3.8}$$

The conversion requires the so called *double resonance*, i.e. the incoming and the nascent waves must be in the double accordance of wavelength and frequency. This condition is satisfied when the two dispersion relations coincide. Comparing the equation 5.3.8 with the X mode dispersion relation:

$$1-\left(\frac{k_xc}{\omega}\right)^2=\frac{\left(\frac{\omega_p}{\omega}\right)^2\left(\omega^2-\omega_p^2\right)}{\omega_p^2+\omega_c^2-\omega^2} \tag{5.3.9}$$

it comes out that the *double resonance* takes place at the UHR. The BW can be seen as a longitudinal, compression-rarefaction wave due to the self organization of the electron gyromotion around the magnetic field lines (see figure 5.3.2). According to Segdeev and Shapiro theory [96], the wave energy can be absorbed by the electrons like in case of Landau damping for longitudinal and magnetic field parallel waves. The maximum energy reached by the electrons is given by [96]:

$$W_{max} = \frac{e^2 E_0^2}{2m\omega_c^2} = mc^2 \left(\frac{4\pi P}{\nu_{ph} B^2}\right) \tag{5.3.10}$$

This formula is not so valuable for practical use, because the phase velocity of the BW is usually unknown. But it helps to find the region of BW absorption: the dispersion relation 5.3.5 reveals that the BW exhibits a resonance at cyclotron harmonics, so there $\nu_{ph} \rightarrow 0$ and the most energetic electrons appear. An alternative version of this formula can give the electric field in which the electrons move when the wave acts on them:

$$E\left[\frac{kV}{cm}\right] = 2\left(W_{max}\left[keV\right] \cdot B^2\left[kG\right]\right) \tag{5.3.11}$$

This field is of course intensified where W$_{max}$ assumes its maximum value. Because of the external B field, an $\vec{E} \times \vec{B}$ drift can arise, as depicted in figure 5.3.2. In a cylindrical symmetry this drift forms an azimuthal flow rotating around the plasma axis. Viscosity and non linear phenomena could then generate a 3D, *typhoon-shaped* plasma vortex [97]. The EM-to-ES conversion mechanism could produce non-linear processes. They appear as additional components in the wave spectrum.

5.3.2 Experimental results

Measurements of the plasma density and temperature were made by a movable Langmuir Probe, described in the section 3.4.2. The probe tip can be used as local electromagnetic antenna, which can be connected to a Spectrum Analyzer (SA) for the plasma spectral emission analysis. The LP was inserted inside the plasma reactor, introduced in the section 3.2, with an angle of 45° (see figure 3.2.1). A conventional 300 W magnetron was used at 2.45 GHz, while a tunable TWT covered the range 3.2 - 4.9 GHz. The background pressure was kept constant during the experiment (p$\sim$ 10^{-3} mbar), while the RF power was limited to 30 - 40 W for safety of instrumentation. The microwaves were axially launched inside a closed cylindrical

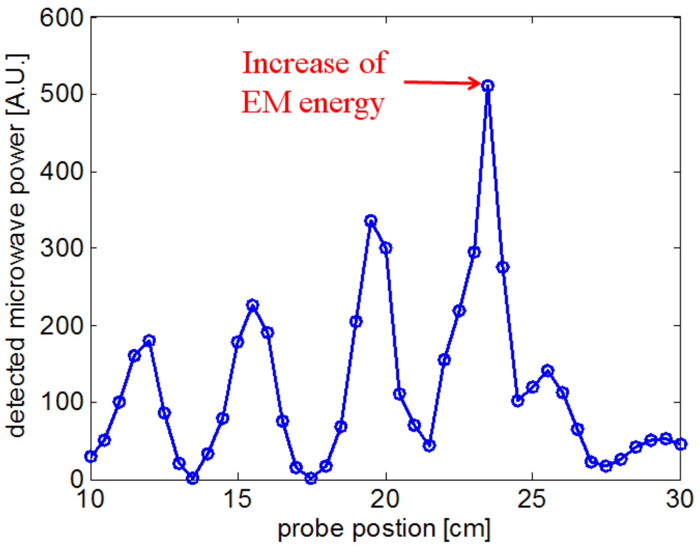

Figure 5.3.3: *Trend of the electromagnetic field energy inside the plasma chamber measured by the LP working as an antenna.*

stainless-steel chamber (a LP position of 28 cm, that is its maximum elongation, corresponds to chamber position of 23 cm). An infrared camera has been used to visualize the heat deposition on the chamber walls.

The electromagnetic wave energy distribution inside the plasma filled chamber is reported in figure 5.3.3, measured at 3.76 GHz (which has given the most clear evidence of mode conversion). Note that, as required in section 5.3.1, standing waves are generated when the coupling is good, and this may favour the mode conversion even in the case of axial wave launching. Moreover, conversely to the usual cavity wave distribution, the electromagnetic energy accumulates in a far window position, around 24 cm (this typically occurs in near UHR zones [98]).

The trend of the electron temperature in different heating configurations is reported in figure 5.3.4. Note that at 3.76 GHz a suprathermal (ST) electron population at probe position equal to 20 cm (corresponding to $B=B_{ECR}/2$) appears; these electrons are much hotter ($T^{ST} > 20$ eV)

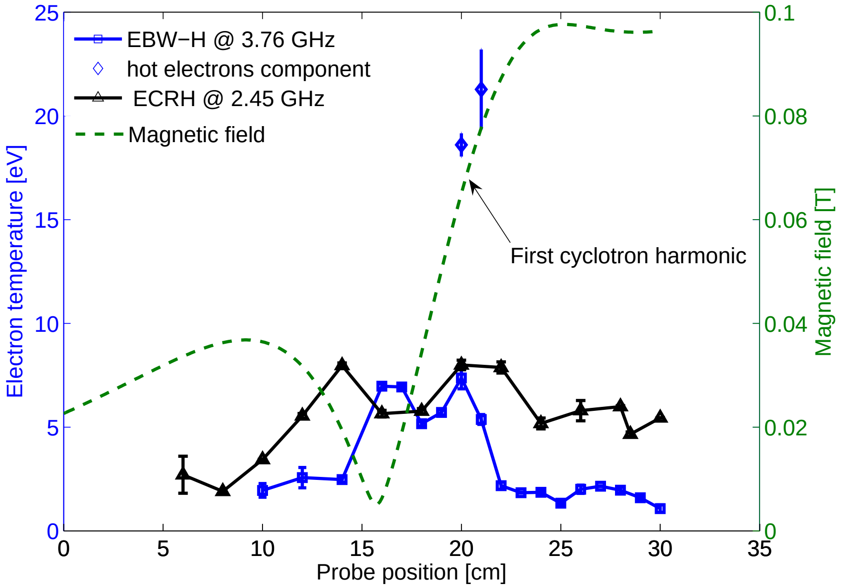

Figure 5.3.4: *Trend of electron temperature at different positions compared with the magnetostatic field shape. Two different operating conditions are reported: conventional heating at* 2.45 *GHz and possible EBW-H at* 3.76 *GHz.*

than that ones observed at 2.45 GHz. At P_{RF} = 40 W was $T^{ST} \sim 40$ eV. The appearance of hot electrons at the first cyclotron harmonic is a signature of possible BW absorption, as predicted in section 5.3.1. The establishment of an overdense plasma (see figure 5.3.5), which is inaccessible to EM waves, is another signature of mode conversion. Figure 5.3.5 clearly evidences the overdense plasma formation in the central part of the cavity, with densities well above the critical value at the corresponding frequency ($1.5 \cdot 10^{17}$ m^{-3}). The evident pronounced oscillations of n_e are due to EM wave cutoffs and resonances displacements.

Where the density is strongly depleted (i.e. around 20 and 24 cm), the ratio between ion and electron saturation currents is much larger than the expected Bohm value. This discrepancy, that is unreasonable in quasi-neutral plasmas, can be only explained by possible plasma flows or *runaway electrons*, predicted by the model proposed in section 5.3.1 when BW are generated. Experimental results (figure 5.3.6, left) show also one ring formed

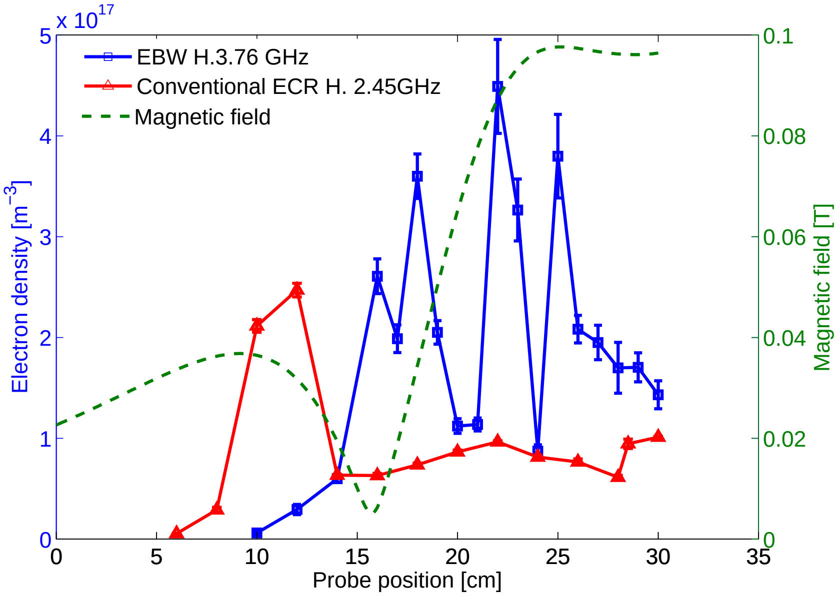

Figure 5.3.5: *Trend of electron electron density along the LP direction of motion: at* 3.76 *GHz the plasma core density largely overcome the O cutoff value* $n_{cutoff} = 1.5 \cdot 10^{-17}\ m^{-3}$.

in correspondence of the strong density depletion (position= 20 cm). The correct ring position has been identified because a high temperature region appears on the plasma chamber walls, as shown in figure 5.3.6 (right). Plasma holes and 3D vortex have been observed in larger devices like those described in [97, 99]; anyway in that case no plausible explanations about the origin of such phenomena were given. Dougar-Jabon and Golovanivsky also observed hot plasma rings when X waves were launched into the plasma: they linked these rotating layers to the internal mode conversion and following BW generation [96], according to the approach proposed in section 5.3.1.

5.3.3 Discussion

Let us come back to the interpretation of the density and temperature profiles which come out at 3.76 GHz. Accurate calculations about wave propa-

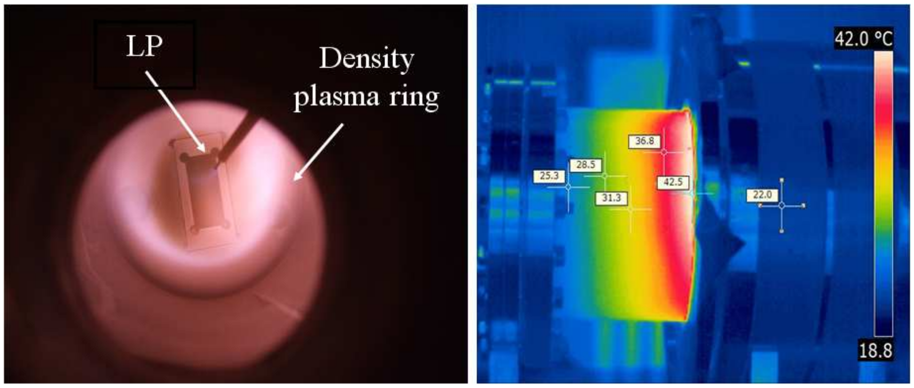

Figure 5.3.6: *(left) CCD camera image of the plasma. The LP also is visible in the picture, other than the high luminosity plasma ring. (right) Thermo-camera measurement: in correspondence of the hot ring a high temperature region appears in the chamber walls.*

gation should take into account the θ angle that $\vec{k}$ forms with the magnetic field. According to relations 5.3.3, it depends on the triplet of numbers n, ν, r. For the plasma reactor seven modes exist in the range 3.76 ± 0.1 GHz, all of them having $r = 5$, $0 < n$, $\nu < 2$, which corresponds to $60^\circ < \theta < 85^\circ$.

The corresponding refraction index for O and X mode calculated for three different θ by means of the Appleton-Hartree relation is shown in figure 5.3.7.

The pumping wave comes from the right side in the figure. Whatever the angle is, the propagation of the X wave is allowed till the X-cutoff located around 25 cm; there, in the XY space (i.e. in the virtual density vs magnetic field space) the extraordinary mode should be reflected towards regions of lower density. Looking to figure 5.3.5, there is a density peak at 25 cm, therefore the X mode can be reflected or it passes through with a non zero probability. The part which is reflected again converts in a O mode (for $\theta < 60^\circ$possibilities of O-X or X-O conversions exist near 28 cm) or reflects on the injection flange. This multi-passing of X and O waves between the cutoff and the input flange may generate the overdense plasma in the region $25 - 30$ cm.

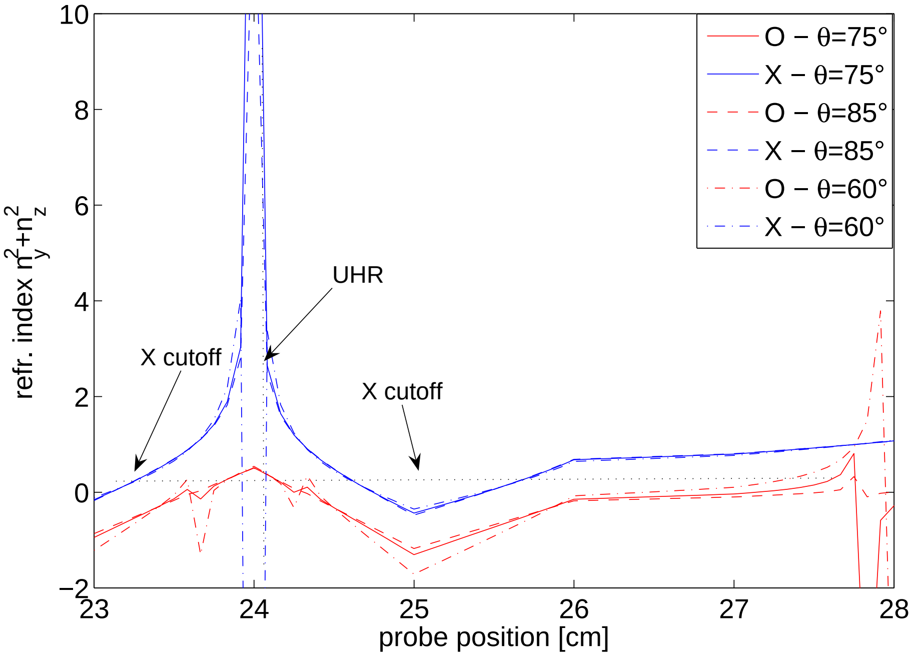

Figure 5.3.7: *Refraction index for ordinary and extraordinary mode propagating at different angles.*

The fraction of extraordinary waves which passes through the cutoff encounters the UHR at position 24.5 cm, where they can be converted into a BW, then absorbed at the first cyclotron harmonic, as observed in figure 5.3.4. The UHR is placed just where the detected electromagnetic energy was amplified, and it is enclosed inside two cutoffs, which is the additional requirement for mode conversion. Another confirmation of the occurred mode conversion comes from the plasma spectral analysis done in proximity of the UHR. Figure 5.3.8 shows that well separated, equally spaced sidebands appear beside to the pumping frequency. The separation is around 10^4 Hz. We tried to correlate the sidebands to some typical wave frequencies of plasmas. They may correspond to possible ion sound waves originated few mm away from the UHR layer or they may be due to same modulation instability, which is usually detected in presence of BW propagation in plasmas. The UHR is located in a critical point, because any density

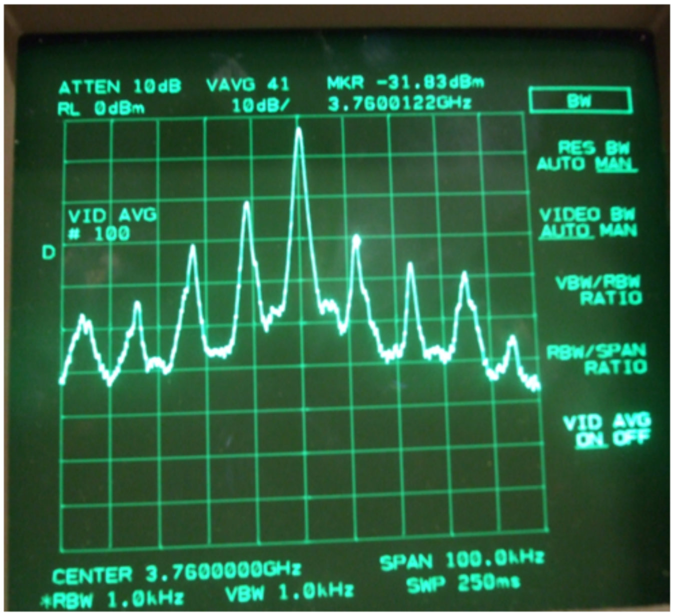

Figure 5.3.8: *Spectral structure of the antenna detected signal close to the UHR.*

increase would move the UH frequency above the pumping wave one (see figure 5.3.6), thus deactivating the conversion mechanism. This is the reason of the density depletion close to the UHR. The density depletion close to the first harmonic is instead generated by the BW absorption and following acceleration of fast electrons. Estimations based on the theory described in section 5.3.1 give a strong electric field:

$$\begin{aligned}\vec{E}\left[\frac{kV}{cm}\right] &= 2\left(W_{max}\left[krV\right]\cdot B^2\left[kG\right]\right) = \\ 2\cdot 10^{-1}\cdot 0.8 &= 0.16\frac{kV}{cm} \\ &= 1.5\cdot 10^4\frac{V}{m}\end{aligned}$$

For this calculation we assumed $W_{max} = 100$ eV, according to measurements, and $B = 0.8$ kG. This electric field originates an $\vec{E}\times\vec{B}$ drift creating an azimuthal plasma flow with $\nu_{drift} = 3\cdot 10^5$ m/sec. This corresponds to ion energy of about 8 keV. The obtained values are very similar to the ones measured in [97] on linear devices for fusion purposes. We plan to measure them in the next months to confirm theoretical prediction.

If the calculations would be confirmed, this method could be used also for industrial purposes, allowing to realize very compact high-density plasma immersed implantators.

By the scientific point of view, the experiment has successfully demonstrated the mode conversion and BW generation in linear and small plasma reactor, thus opening new roads in the increase of ion currents obtainable from proton ion sources.

Chapter 6

Conclusion

The VIS source is a practical device for generating dc proton beam with high current and low emittance. Proton beams up to 45 mA have been extracted from a plasma electrode having a diameter of 8 mm at 60 kV. Proton fraction as high as 80% were generated at different hydrogen mass flow and microwave power. It was shown that these two parameters regulated the amount of the different species extracted from the source ($H^+,\ H_2^+$) by affecting the electron temperature: in fact any variation of T_e modifies the Maxwellian distribution of the thermal electrons, that is correlated to the ionization rates. A complete characterization of the beam has been obtained by means of the Emittance Measurements Unit. The rms normalized beam emittance, measured for different permanent magnets configurations, hydrogen plasma flow, high voltage and microwave power, is lower than $0.2\,\pi$ mm mrad.

Another set of measurements has been then collected with the SILHI, that was also operated in pulsed mode: current higher than 90 mA, with rms normalized emittance value lower than $\sim 0.17\pi$ mm mrad have been measured in pulsed mode. For both the sources good results we have obtained in terms of low divergence and high currents, fitting the requirements of the projects currently under design or already in the preparatory phase.

In particular they are:

- the MYRRHA facility (Multi-purpose hybrid research reactor for hightech applications);

- the DAEDALUS project;
- the ESS facility (European Spallation Source).

The goal of the **MYRRHA** project is to demonstrate the technical feasibility of transmutation in an Accelerator Driven System (ADS) by building a new flexible irradiation complex in Mol (Belgium). Based on the transmutation process, such a device allows to decrease lifetime of the radioactive wastes, and consequently to relax the constraints on the geological disposals. The MYRRHA facility will be able to operate in sub-critical and critical modes, requiring a 2.4 MW proton accelerator (600 MeV, 4 mA max) operating in CW mode; a critical requirement will be the production of a very limited number of unforeseen beam interruptions per year. This stringent reliability requirements are motivated by the fact that frequently-repeated beam interruptions may induce high thermal stresses and fatigue on the reactor structures, the target or the fuel elements, with possible significant damages especially on the fuel claddings. Moreover, beam interruptions can dramatically decrease the plant availability, possibly implying plant shutdowns of tens of hours in most of the cases. The present tentative limit for the number of allowable beam trips is therefore 10 transients longer than 3 seconds per 3-month operation cycle [5, 100].

The realization of the 50 kV MDIS proton source is proven to be a very reliable technological choice: a source similar to SILHI source, described in the section 3.3, could be the best option.

The primary goal of **DAEDALUS** is to search for CP violation in a complementary manner to the present plans.The present suite of experiments is based on long-baseline conventional neutrino beams. These beams are produced by impinging high-energy protons on a target, resulting in pions and kaons which are sign-selected and focused by a magnet in the direction of a neutrino detector located ∼ 1000 km away[1]. CP violation is explored by comparing the rates of $\nu_{mu} \rightarrow \nu_e$ to $\bar{\nu}_{mu} \rightarrow \bar{\nu}_e$ These experiments are hampered by a lack of antineutrino statistics and by poor signal-to-background ratio, and suffer for a complication of matter effects [6]. This facility therefore needs a proton source that produces several milliamperes of protons.

The goal of the European Spallation Source (**ESS**) project is to construct and operate the next generation, high-intensity neutron source for Europe. The high luminosity and the advanced neutron methods available at ESS will be required to tackle challenges such as those set by the quest for more effective energy production and storage, and a higher quality of life with better health in a cleaner environment as well as to satisfy human scientific curiosity.

The spallation process is almost 10 times more efficient than fission in terms of neutron production, and is firmly based on proven technology. The ESS development programme will, however, explore novel ways for producing neutron beams. These centre on a new multi-megawatt, accelerator-driven spallation neutron source. It will generate neutron beams that are 50 times brighter, thanks to the long pulse of protons and the high power of the accelerator [101].

Lund was chosen as the site of the European Spallation Source in May 2009. The superconducting linac is expected to begin delivering beam to users in 2019, eventually delivering an average beam power of 5 MW to a single neutron target station with a proton (H^+) macro-pulse current of (provisionally) 50 mA at 2.5 GeV in 2.0 ms long pulses at a repetition rate of 20 Hz, the ESS parameters are shown in table 6.1.

The Electron Cyclotron Resonance proton source will deliver macropulses up to 2 ms in length with currents of up to 90 mA. Pulse repetition frequencies as high as 40 Hz may be viable, permitting interleaved delivery to 2

---

[1] Neutrinos are produced through the decay chain:

$$\begin{aligned} \pi^+ \rightarrow \nu_\mu + \quad & \mu^+ \\ & \hookrightarrow \quad \bar{\nu}_\mu e^+ \nu_e \end{aligned}$$

Table 6.1: *Possible ESS nominal and upgrade performance that will be built into the flexible pulse structure during baseline construction.*

INPUT		N.	U.
Average beam power	(MW)	5	7.5
Macro-pulse length	(ms)	2	2
Pulse repetition rate	(Hz)	20	20
Proton kinetic energy	(GeV)	2.5	2.5
Peak coupler power	(MW)	1	1
Beam loss rate	(W/m)	< 1.0	< 1.0
OUTPUT			
Duty factor		0.04	0.04
Ave. pulse current	(mA)	50	75
Ion source current	(mA)	60	90
Total linac length	(m)	418	418

target stations at 20 Hz. The Low Energy Beam Transport matches the beam extracted from the ion source into the Radio Frequency Quadrupole with minimal emittance growth, using a dual solenoid system. Magnetic focusing permits space charge neutralization via the ionization of the residual gas. The slow chopper system beam dump embedded in the first part of the LEBT is mainly an aperture reduction of the cooled vacuum chamber. A negatively polarized ring located at the RFQ entrance acts as an electron barrier, and provides two functions [4]:

1. Eliminating an electron flow from the LEBT into the RFQ which would provoke incorrect DCCT current measurements;

2. Inducing a better space charge neutralization near the RFQ entrance, helping beam focusing into the cavity.

INFN-LNS (Catania) and CEA-Saclay will contribute to the design of the injector part (the proton source and the LEBT) in close collaboration.The high current proton source will be based on the know-how acquired during the design phase and the construction phase and commissioning of the sources named TRIPS and VIS at INFN-LNS and of the SILHI source at CEA-Saclay, but surely some remarkable improvements are to be developed because of the high current at a relatively low extraction voltage. A new extraction system has to be developed for a pulsed beam of about 60 mA with a quite low emittance as required by the following RFQ.

In ESS facility the input emittance of RFQ is $\sim 0.2\pi$ mm mrad, so the emittance of the extracted beam (also in the LEBT) must keep lower than this value. If we consider the emittance measurements carried out on the SILHI source at low duty cycle (~ 0.04) and for high ion beam current 4.2.2, we can observe that emittance assumed values lower than 0.156π mm mrad.

The measurements show in this thesis are very encouraging for the design of the future proton sources, but some additional technological changes will be needed to satisfy the requirements of ESS project. A new design of the magnetic field profile is to be considered (in order to get a denser plasma) and the microwave injection system will be deeply revised according to the recent experience gained with the VIS source. A new idea to enhance the electric field in the plasma chamber will be tested in order to get highest ionization rates. Further studies about brightness optimization are mandatory, which can be carried out either at CEA and at INFN-LNS.The LEBT from the source extractor to the RFQ entrance must take into account different and competitive requests as it should be the shortest as possible and it should permit to allocate the necessary diagnostics and the low energy chopper.

Many efforts will be paid in the investigation of electrostatic wave heating, discussed in chapter 5. Proton sources fully based on this novel philosophy of plasma ignition could be ready in three or four years, after an adequate modelling of the involved physical mechanisms, and a proper design of the related technology (see section 5.3).

Acknowledgements

First, I would like to express my gratitude to Prof. Salvatore Cavallaro, who followed my PhD activities as tutor. Another person who deserve my sincere gratitude is Dr. Santo Gammino for giving me an opportunity to work in the ion source group of the LNS-INFN and for his invaluable guidance and support in the course of this work. The largest part of the work described in this thesis has been carried out at the Laboratori Nazionali del Sud of INFN Catania: I thank the LNS director, Prof. Marcello Lattuada, for the opportunity to stay there during my PhD course, in a friendly and intellectually fertile environment, and all the laboratory staff. The support of the PhD course coordinator, Prof. Francesco Riggi, is especially acknowledged.

I wish to thank Dr. David Mascali and Dr. Luigi Celona for professional help and fruitful, without them I could not have finished this thesis. I extend my thanks to all people working with the ion source group, especially Dr. Giovanni Ciavola, Luciano Allegra and Dr. Giuseppe Castro. I would like to thank the ion source people from CEA-SACLAY, for helping me during the experimental activities in Saclay, thank Dr. Raphael Gobin, Adroit Guillame and Frank Senee. Special thanks to Dr. F. Odorici and Dr. L. Malferrari of the INFN of Bologna, for their precious help and collaboration for the measurements carried out by means the CNTs. My time at LNS was made enjoyable in large part due to the many friends that became a part of my life: thank all the guys of the *Allegra Cafè Social Club* and all my friends.

My work would not possible without the support of my family: I like to thank my family: mother, father, brother and grandmother for their

encouragement.

Bibliography

[1] B. Wolf. *Handbook of Ion Source.* FL: CRC Press, Boca Raton, 1995.

[2] F. Carminati, R. Klapisch, J.P. Revol, C. Roche, J.A. Rubio, and C. Rubbia. An energy amplifier for cleaner and inexhaustible nuclear energy production driven by a particle beam accelerator. *CERN-AT-93-47-ET*, page 70, 1993.

[3] L. Celona, G. Ciavola, S. Gammino, R. Gobin, and R. Ferdinand. TRIPS: The high intensity proton source for the TRASCO project. *Review of Scientific Instruments*, 71:771–773, 2000.

[4] S. Peggs et al. Plans for the ESS LINAC. 2010. Proc. LINAC conference, Tsukuba, Japan.

[5] J.L. Biarrotte, A.C. Mueller, H. Klein, P. Pierini, and D. Vandeplassche. Accelerator reference design for the MYRRHA European ADS demonstrator. 2010. Proc. LINAC conference, Tsukuba, Japan.

[6] J. Alonso, F. T. Avignone, W. A. Barletta, R. Barlow, H. T. Baumgartner, A. Bernstein, E. Blucher, L. Bugel, L. Calabretta, et al. Expression of interest for a novel search for cp violation in the neutrino sector: Daedalus. 2010.

[7] F. Odorici, M. Cuffiani, L. Malferrari, R. Rizzoli, G. P. Veronese, L. Celona, S. Gammino, D. Mascali, R. Miracoli, F. P. Romano, N. Gambino, G. Castro, G. Ciavola, and T. Serafino. Enhancement of ECR performances by means of carbon nanotubes based electron guns. 2010. Proc. 19^{th} Workshop on ECR ion Sources, Grenoble.

[8] D. Mascali, L. Celona, S. Gammino, R. Miracoli, G. Castro, N. Gambino, and G Ciavola. Electrostatic wave heating and possible formation of self-generated high electric fields in a magnetized plasma. Proc. 4^{th} International Conference on Superstrong Fields in Plasmas Varenna, Italy, October $3-9$ (2010) To be published on Nuclear Instruments and Methods A.

[9] R. Geller. *Electron Cyclotron Resonance Ion Sources and ECR Plasmas*. PA: Inst. Phys., Philadelphia, 1996.

[10] S. Barbarino. Appunti di campi elettromagnetici.

[11] F. F. Chen. *Introduction to the Plasma Physics and Controlled Fusion: Plasma Physics*. U.K.:London Press, London, 1986.

[12] Ira B. Bernstein. Waves in a plasma in a magnetic field. *Phys. Rev.*, 109:10–21, Jan 1958.

[13] H. P. Laqua. Electron Bernstein wave heating and diagnostic. *Plasma Physics and Controlled Fusion*, 49:R1, 2007.

[14] P. W. Hitz. *Recent Progress in High Frequency Electron Cyclotron Resonance Ion Source*. Academic Press, Elsevier , USA, 2006.

[15] M. P. Stockli. Measuring and analyzing the transverse emittance of charged particle beams. volume 868. AIP Conf. Proc., November 2006.

[16] I. G. Brown. *The Physics and Technology of Ion Sources*. NewYork: Wiley, 2004.

[17] M. P. Stockli. Design of the extraction system of the superconducting ECR ion source VENUS. Proceedings of the 2001 Particle Accelerator Conference, Chicago, June 2001.

[18] S. Gammino, L. Celona, G. Ciavola, F. Maimone, and D. Mascali. Review on high current 2.45 GHz electron cyclotron resonance sources (invited). *Review of Scientific Instruments*, 81:02B313, 2010.

[19] O. A. Popov, S. Y. Shapoval, and M. D. Yoder Jr. 2.45 GHz microwave plasmas at magnetic fields below ECR. *Plasma Sources Science and Technology*, 1:7, 1992.

[20] D. Mascali, N. Gambino, R. Miracoli, S. Gammino, L. Torrisi, F. Maimone, and L. Tumino. Plasma parameters measurements by means of Langmuir probe. *Radiation Effects and Defects in Solids*, 163:471, 2008.

[21] G. Lisitano, Jr. R. A. Ellis, W. M. Hooke, and T. H. Stix. Production of Quiescent Discharge with High Electron Temperatures. *Review of Scientific Instruments*, 39:295–297, 1968.

[22] G. Lisitano, M. Fontanesi, and E. Sindoni. NONRESONANT ABSORPTION OF ELECTROMAGNETIC WAVES IN A HIGH-DENSITY PLASMA. *Applied Physics Letters*, 16:122–124, 1970.

[23] N. Sakudo. Microwave ion sources for industrial applications (invited). *Review of Scientific Instruments*, 71:1016–1022, 2000.

[24] N. Sakudo, K. Tokiguchi, H. Koike, and I. Kanomata. Microwave ion source for high-current implanter. *Review of Scientific Instruments*, 49:940–943, 1978.

[25] J. Ishikawa, Y. Takeiri, and T. Takagi. Axial magnetic field extraction-type microwave ion source with a permanent magnet. *Review of Scientific Instruments*, 55:449–456, 1984.

[26] T. Taylor and J. S. C. Wills. A high-current low-emittance dc ECR proton source. *Nuclear Instruments and Methods in Physics Research Section A: Accelerators, Spectrometers, Detectors and Associated Equipment*, 309:37 – 42, 1991.

[27] T. Taylor and J. F. Mouris. An advanced high-current low-emittance dc microwave proton source. *Nuclear Instruments and Methods in Physics Research Section A: Accelerators, Spectrometers, Detectors and Associated Equipment*, 336:1 – 5, 1993.

[28] Joseph Sherman, Andrew Arvin, Lash Hansborough, David Hodgkins, Earl Meyer, J. David Schneider, Jr. H. Vernon Smith, Matthew Stettler, Jr. Ralph R. Stevens, Michael Thuot, Thomas Zaugg, and Robin Ferdinand. Status report on a dc 130 mA, 75 keV proton injector (invited). *Review of Scientific Instruments*, 69:1003–1008, 1998.

[29] J.M. Lagniel, P.Y. Beauvais, D. Bogard, G. Bourdelle, G. Charruau, O. Delferrière, D. De Menezes, A. France, R. Ferdinand, Y. Gauthier, R. Gobin, F. Harrault, J.L. Jannin, P.A. Leroy, I. Yao, P. Ausset, B. Pottin, N. Rouvière, L. Celona, and S. Gammino. Status and new developments of the high intensity electron cyclotron resonance source light ion continuous wave, and pulsed mode (invited). *Review of Scientific Instruments*, 71:830–835, 2000.

[30] H. W. Zhao, B. W. Wei, Z. W. Liu, Y. F. Wang, and W. J. Zhao. Development of ECR ion sources in China (invited). *Review of Scientific Instruments*, 71:646–650, 2000.

[31] Y. Kato, S. Kobayashi, and S. Ishii. Enhanced production of multicharged ions using pulse-modulated microwave in a 2.45 GHz electron cyclotron resonance source. *Review of Scientific Instruments*, 71:657–659, 2000.

[32] S. Ishii, H. Oyama, and H. Odagiri. Fundamental study of ECR multicharged ion sources. *Nuclear Instruments and Methods in Physics Research Section B: Beam Interactions with Materials and Atoms*, 37-38:147 – 150, 1989.

[33] P. Roychowdhury and D. P. Chakravarthy. High intensity electron cyclotron resonance proton source for low energy high intensity proton accelerator. *Review of Scientific Instruments*, 80:123305, 2009.

[34] X. Jia, T. Zhang, S. Luo, C. Wang, X. Zheng, Z. Yin, J. Zhong, L. Wu, and J. Qin. Design of a compact, permanent magnet electron cyclotron resonance ion source for proton and H_2^+ beam production. *Review of Scientific Instruments*, 81:02A321, 2010.

[35] I. S. Hong, B. S. Park, J. H. Jang, H. J. Kwon, Y. S. Cho, and Y. S. Hwang. Design and construction of a compact microwave proton source for a proton linac. *Review of Scientific Instruments*, 81:02A314, 2010.

[36] R. F. Welton, M. P. Stockli, S. N. Murray, T. R. Pennisi, B. Han, Y. Kang, R. H. Goulding, D. W. Crisp, D. O. Sparks, N. P. Luciano, J. R. Carmichael, and J. Carr. H^- ion source developments at the SNS. *Review of Scientific Instruments*, 79:02C721, 2008.

[37] R. F. Welton, J. Carmichael, N. J. Desai, R. Fuga, R. H. Goulding, B. Han, Y. Kang, S. W. Lee, S. N. Murray, T. Pennisi, K. G. Potter, M. Santana, and M. P. Stockli. The continued development of the spallation neutron source external antenna H^- ion source. *Review of Scientific Instruments*, 81:02A727, 2010.

[38] M. Kronberger, D. Küchler, J. Lettry, Ø . Midttun, M. O'Neil, M. Paoluzzi, and R. Scrivens. Commissioning of the new H^- source for Linac4. *Review of Scientific Instruments*, 81:02A708, 2010.

[39] R.F. Welton. Overview of High Intensity H^- ion sources. volume 868, page 559. Proceedings of LINAC02, Gyeongju, Korea, 2002.

[40] L.Celona, S.Gammino, G. Ciavola, F. Chines, S. Marletta, and E. Messina. Ionization efficiency measurements with the Microwave Discharge Ion Source MIDAS. pages 1601–1603. Proceedings of EPAC 2000, Vienna, Austria, 2000.

[41] G. Ciavola, S. Gammino, G. Raia, and J. Sura. MIDAS, a high efficiency microwave discharge ion source for the EXCYT facility. *Review of Scientific Instruments*, 65:1110–1112, 1994.

[42] S. Gammino, G. Ciavola, L. Celona, L. Torrisi, M. Castro, F. Chines, S. Marletta, E. Messina, J. Qin, and Z. Wang. Off-line efficiency measurements of the microwave discharge source (MIDAS) at the Laboratorio Nazionale del Sud. *Review of Scientific Instruments*, 69:747–749, 1998.

[43] L. Celona, G. Ciavola, S. Gammino, F. Chines, M. Presti, L. Andò, X. H. Guo, R. Gobin, and R. Ferdinand. Status of the Trasco Intense Proton Source and emittance measurements. *Review of Scientific Instruments*, 75:1423–1426, 2004.

[44] G. Ciavola, L. Celona, S. Gammino, M. Presti, L. Andò, S. Passarello, XZh. Zhang, F. Consoli, F. Chines, C. Percolla, V. Calzona, and M. Winkler. A version of the Trasco Intense Proton Source optimized for accelerator driven system purposes. *Review of Scientific Instruments*, 75:1453–1456, 2004.

[45] W. Krauss-Vogt, H. Beuscher, H.L. Hagedoorn, J. Reich, and P. Wucherer. Emittance and matching of ECR sources. *Nuclear Instruments and Methods in Physics Research Section A: Accelerators, Spectrometers, Detectors and Associated Equipment*, 268:5 – 9, 1988.

[46] F. Maimone, G. Ciavola, L. Celona, S. Gammino, D. Mascali, N. Gambino, R. Miracoli, F. Chines, S. Passarello, G. Gallo, and E. Zappalà. Status of the versatile ion source vis. volume 868, page MOPC151. Proceedings of EPAC08, Genoa, Italy, 2008.

[47] F. Maimone et al. Proceedings of 23rd Symposium on Plasma Physics and Technology, 16 – 19 June, Prague, Czech Republic, 2008.

[48] Online available http://www.ansoft.com/products/hf/hfss/.

[49] F. Maimone et al. INFN Report $INFN/TC-07/04$, 2008.

[50] L. Celona. Private communication.

[51] F. Maimone. Private communication.

[52] M. Rosalba. Studio per mezzo di una langmuir probe delle proprietà fisiche di un plasma generato da microonde, 2007. Degree Thesis in Physics, Università degli studi di Catania, Italy.

[53] S. Gammino, D. Mascali, L. Celona, G. Ciavola, F. Maimone, S. Barbarino, N. Gambino, R. Miracoli, and F. Samperi. Diagnostics and

preliminary operations of a microwave discharge plasma reactor for complex molecules dissociation. volume 31F, pages P–2.066. Proceedings of 34th EPS Conference on Plasma Phys., Warsaw, 2007.

[54] Online Available: http://www.home.agilent.com/agilent/product.jspx?nid = −536902643.761696.00&cc=US&lc=eng.

[55] S. Gammino, L. Celona, G. Ciavola, N. Gambino, F. Maimone, D. Mascali, R. Miracoli, and L.Torrisi. Microwave absorption in dense and overdense plasmas generated in a plasma reactor for environmental applications. volume 32D, pages P–1.174. Proceedings of 35th EPS Conference on Plasma Phys., Hersonissos, 2008.

[56] L. Celona, S. Gammino, F. Maimone, D. Mascali, N. Gambino, R. Miracoli, and G. Ciavola. Observations of resonant modes formation in microwave generated magnetized plasmas. *Eur. Phys Journal D*, 10.1140/epjd/e2010-00244-y, 2010.

[57] D. Mascali. *A new approach to the study of the ECR-heating and particle dynamics in the plasma of the Electron Cyclotron Resonance Ion Sources*. PhD thesis, Università degli studi di Catania, Italy, 2009.

[58] O. Delferrière, D. De Menezes, R. Gobin, F. Harrault, and O. Tuske. Electron cyclotron resonance 140 mA D^+ beam extraction optimization for IFMIF EVEDA accelerator. *Review of Scientific Instruments*, 79:02B723, 2008.

[59] R. Gobin, P. Y. Beauvais, R. Ferdinand, J. M. Lagniel, P. Ausset, B. Monsanglant, B. Pottin, and N. Rouvière. SILHI proton beam (80 mA-95 keV) characteristics as a function of the beam line atmosphere at CEA/Saclay. *Vacuum*, 60:261 – 266, 2001.

[60] P. Y. Beauvais, R. Ferdinand, R. Gobin, J. M. Lagniel, P.A. Leroy, L. Celona, G. Ciavola, S. Gammino, B. Pottin, and J. Sherman. Emittance improvement of the electron cyclotron resonance high intensity light ion source proton beam by gas injection in the low energy beam transport. *Review of Scientific Instruments*, 71:1413–1416, 2000.

[61] R. Gobin, P.Y. Beauvais, O. Delferrière, D. De Menezes, O. Tuske, G. Adroit, Y. Gauthier, and F. Harrault. A 140 mA cw deuteron electron cyclotron resonance source for the IFMIF-EVEDA project. *Review of Scientific Instruments*, 79:02B303, 2008.

[62] R. Gobin, P.-Y. Beauvais, D. Bogard, G. Charruau, O. Delferrière, D. De Menezes, A. France, R. Ferdinand, Y. Gauthier, F. Harrault, P. Mattéi, K. Benmeziane, P. Leherissier, J. Y. Paquet, P. Ausset, S. Bousson, D. Gardes, A. Olivier, L. Celona, and J. Sherman. Status of the light ion source developments at CEA/Saclay. *Review of Scientific Instruments*, 75:1414–1416, 2004.

[63] D. Yuan, K. Jayamanna, T. Kuo, M. McDonald, and P. Schmor. An emittance-mass scanner for small-mass, low-energy beams. *Review of Scientific Instruments*, 67:1275–1276, 1996.

[64] G. D. Shirkov and G. Zschornsack. *Electron Impact Ion Source for Charged Heavy Ions.* Vieweg, Wiesbaden, 1996.

[65] I. H. Hutchinson. *Principles of Plamsa Diagnostics.* Cambridge University Press, New York, 2002.

[66] K. Horvath. *Characterisation and Optimisation of WEGA Plasma.* PhD thesis, Ernst Moritz Universitat Greifswald, 2004.

[67] Hiden ESPion-Advanced Langmuir Probe for Plasma Diagnostics. Online Available:http://www.hidenanalytical.com/products/cat30.html.

[68] J. R. Coupland, T. S. Green, D. P. Hammond, and A. C. Riviere. A study of the ion beam intensity and divergence obtained from a single aperture three electrode extraction system. *Review of Scientific Instruments*, 44(9):1258–1270, 1973.

[69] Roderich Keller. Ion extraction systems: optics and design. *Nuclear Instruments and Methods in Physics Research Section A: Accelerators, Spectrometers, Detectors and Associated Equipment*, 298:247 – 254, 1990.

[70] K. Tokiguchi, N. Sakudo, and H. Koike. Beam extraction experiments from microwave ion sources. *Review of Scientific Instruments*, 57:1526–1530, 1986.

[71] D. Spence, G. McMichael, K. R. Lykke, J. D. Schneider, J. Sherman, R. Stevens, Jr., and D. Hodgkins. Production of high-brightness continuous wave proton beams with very high proton fractions. *Review of Scientific Instruments*, 67:1642, 1996.

[72] D. Spence and K. R. Lykke. Generation of High-purity cw Proton Beams from Microwave-driven Sources. Proc. of the Part. Accel. Conf., Dallas, TX, USA, May, 1995.

[73] S. Gammino, G. Ciavola, L. Celona, L. Torrisi, D. Mascali, S. Passarello, and A. Galatà. Enhancement of ion current from the TRIPS source by means of different electron donors. *Review of Scientific Instruments*, 77:03B511, 2006.

[74] H. Zhang. *Ion Sources.* Science Press Beijing and Springer, 1999.

[75] K. Schindl. *Space charge.* World Scientific Publishing Co. Pte. Ltd, 1999. Proocedings of the joint US-Cern-Japan Russia School on Particle Accelerator: Beam Measurements.

[76] P. Spádtke. Model for the description of ion beam extraction from electron cyclotron resonance ion sources. *Review of Scientific Instruments*, 81:02B725, 2010.

[77] Wai-Ming Tam. *CHARACTERIZATION OF THE PROTON ION SOURCE BEAM FOR THE HIGH INTENSITY NEUTRINO SOURCE AT FERMILAB.* PhD thesis, Department of Physics, Indiana University, 2010.

[78] S. Gammino, L. Celona, R. Miracoli, D. Mascali, G. Castro, G. Ciavola, F. Maimone, R. Gobin, O. Delferrière, G. Adroit, and

F. Senèe. Tests of the Versatile Ion Source (VIS) for high power proton beam production. Proc. 19th Workshop on ECR ion Sources, Grenoble, 2010.

[79] S. Gammino, L. Celona, G. Ciavola, R. Miracoli, et al. Production of intense beams with the Versatile Ion Source (VIS). LNS report 2009.

[80] S. Gammino, L. Celona, F. Maimone, R. Miracoli, D. Mascali, and G. Ciavola. Tests of the Versatile Ion Source (VIS) for high power proton beam production. Proc. LINAC conference, Tsukuba, 2010.

[81] P.Y. Beauvais, J.M. Lagniel, N. Pichoff, G. Haouat, and P. Chaix. SPACE-CHARGE NEUTRALIZATION EXPERIMENT WITH A LOW-ENERGY PROTON BEAM. Proc. of the XVIII International LINAC Conference, Geneva, Switzerland, 1996.

[82] A. BenIsmail, R. Duperrier, D. Uriot, and N. Pichoff. Space charge compensation studies of hydrogen ion beams in a drift section. *Phys. Rev. ST Accel. Beams*, 10:070101, 2007.

[83] J. Dienelt, K. Zimmer, F. Scholze, B. Dathe, and H. Neumann. Generation of a pulsed ion beam with a tuned electronic beam switch. *Plasma Sources Science and Technology*, 12:489, 2003.

[84] Yoshiaki Hirai, Yushi Kato, Fuminobu Sato, and Toshiyuki Iida. Pulse modulated microwave operation on large bore electron cyclotron resonance ion source with cylindrically comb-shaped magnetic fields configuration. *Review of Scientific Instruments*, 81:02A325, 2010.

[85] S. Gammino, J. Sijbring, and A. G. Drentje. Experiment with a biased disk at the k.v.i. ecris. *Review of Scientific Instruments*, 63:2872–2874, 1992.

[86] I. Boscolo et al. APPLICATION OF FERROELECTRIC CATHODES TO ENHANCE THE ION YIELD IN THE CAESAR SOURCE AT LNS. page 1631, 2000. Proc. of Eur. Part. Acc. Conf., Vienna, Austria.

[87] F. Odorici, M. Cuffiani, L. Malferrari, R.Rizzoli, G. P. Veronese, S. Gammino, L. Celona, D. Mascali, N. Gambino, R. Miracoli, and T. Serafino. The CANTES experiment: a carbon nanotubes based electron gun to improve performances of Electron Cyclotron Resonant Ion Sources. 2010. Proc. IPRD, Siena.

[88] L. Schachter, S. Dobrescu, K. E. Stiebing, and J. D. Meyer. On the physics of metal–dielectric structures in ecr ion sources. *Review of Scientific Instruments*, 75:1511–1513, 2004.

[89] A. G. Drentje. Techniques and mechanisms applied in electron cyclotron resonance sources for highly charged ions. *Review of Scientific Instruments*, 74:2631–2645, 2003.

[90] D. Mascali, G. Ciavola, S. Gammino, L. Celona, F. Consoli, S. Passarello, S. Barbarino, and F. Maimone. Measurement of the TRIPS source plasma parameters by means of a Langmuir probe. 2006. INFN/TC-06/03.

[91] R. Angelucci, I. Boscolo, A. Ciorba, M. Cuffiani, L. Malferrari, A. Montanari, F. Odorici, S. Orlanducci, R. Rizzoli, M. Rossi, V. Sessa, M.L. Terranova, and G.P. Veronese. Honeycomb arrays of carbon nanotubes in alumina templates for field emission based devices and electron sources. *Physica E*, 42:1469 – 1476, 2010.

[92] Z. Q. Xie and C. M. Lyneis. Improvements on the LBL AECR Source. 1995. Proc. 12^{th} Int. Workshop ECR Ion Sources, Tokyo, Japan.

[93] D. Mascali, S. Gammino, L. Celona, G. Ciavola, L. Neri, R. Miracoli, N. Gambino, G. Castro, and F. Maimone. Some considerations about frequency tuning effect in ECRIS plasmas. 2010. Proc. 19^{th} Workshop on ECR ion Sources, Grenoble.

[94] Y. Y. Podoba, H. P. Laqua, G. B. Warr, M. Schubert, M. Otte, S. Marsen, F. Wagner, and E. Holzhauer. Direct observation of electron-bernstein wave heating by $o - x - b$-mode conversion at low

magnetic field in the wega stellarator. *Phys. Rev. Lett.*, 98:255003, 2007.

[95] Thomas Howard Stix. *Waves in plasmas.* Springer-Verlag New York, 1992.

[96] K. S. Golovanivsky, V. D. Dougar-Jabon, and D. V. Reznikov. Proposed physical model for very hot electron shell structures in electron cyclotron resonance–driven plasmas. *Phys. Rev. E*, 52:2969–2973, 1995.

[97] K. Nagaoka, A. Okamoto, S. Yoshimura, M. Kono, and M. Y. Tanaka. Spontaneous Formation of a Plasma Hole in a Rotating Magnetized Plasma: A Giant Burgers Vortex in a Compressible Fluid. *Phys. Rev. Lett.*, 89:075001, 2002.

[98] R. B. White and F. F. Chen. Amplification and absorption of electromagnetic waves in overdense plasmas. *Plasma Physics*, 16:565, 1974.

[99] S. YOSHIMURA, A. OKAMOTO, and M. Y. TANAKA. Measurement of Ion Flow Velocity Field Associated with Plasma Hole Using Laser Induced Fluorescence Spectroscopy. *J. Plasma Fusion Res. SERIES*, 8:11–14, 2009.

[100] http://myrrha.sckcen.be/.

[101] Nina Hall, editor. *NEUTRONS for SCIENCE, NEUTRONS for SOCIETY, Why Europe needs the European Spallation Source.* June 2009. European Spallation Source Scandinavia.